

ENTANGLING ATOMS FOR QUANTUM METROLOGY

A DISSERTATION

SUBMITTED TO THE DEPARTMENT OF APPLIED PHYSICS
AND THE COMMITTEE ON GRADUATE STUDIES
OF STANFORD UNIVERSITY
IN PARTIAL FULFILLMENT OF THE REQUIREMENTS
FOR THE DEGREE OF
DOCTOR OF PHILOSOPHY

Rajiv Krishnakumar

September 2017

© 2017 by Rajiv Krishnakumar. All Rights Reserved.
Re-distributed by Stanford University under license with the author.



This work is licensed under a Creative Commons Attribution-
Noncommercial 3.0 United States License.
<http://creativecommons.org/licenses/by-nc/3.0/us/>

This dissertation is online at: <http://purl.stanford.edu/sb587hw2094>

I certify that I have read this dissertation and that, in my opinion, it is fully adequate in scope and quality as a dissertation for the degree of Doctor of Philosophy.

Mark Kasevich, Primary Adviser

I certify that I have read this dissertation and that, in my opinion, it is fully adequate in scope and quality as a dissertation for the degree of Doctor of Philosophy.

Jason Hogan

I certify that I have read this dissertation and that, in my opinion, it is fully adequate in scope and quality as a dissertation for the degree of Doctor of Philosophy.

Amir Safavi-Naeini

Approved for the Stanford University Committee on Graduate Studies.

Patricia J. Gumpert, Vice Provost for Graduate Education

This signature page was generated electronically upon submission of this dissertation in electronic format. An original signed hard copy of the signature page is on file in University Archives.

Abstract

Atomic sensors, such as atomic clocks and atom interferometers, have to date achieved very precise measurements of various quantities such as time, acceleration, gravitational fields and distances. However they currently use coherent (or unentangled) states of atoms, which imply that their precisions are limited by the standard quantum limit and their precision scales as \sqrt{N} where N is the number of atoms being used in the sensor. However this limit of these sensors can be reduced by using atoms that are in an entangled states.

This work's main focus is on the creation of specific type of entangled states known as spin-squeezed states. The creation of a 20dB spin-squeezed state an ensemble of ultracold ^{87}Rb atoms using a cavity-mediated light-atom interaction is demonstrated, with which proof-of-principle metrology is performed. More specifically, a tipping measurement resolving more than 18dB beyond the standard quantum limit and a clock measurement with a quantum enhancement of over 10dB are shown. The single-shot phase resolution of the apparatus of $147\ \mu\text{rad}$ achieved is the most precise to have been shown to date. In addition, preliminary results in which retention of squeezing of in free-space for over 1ms are discussed.

Another experiment showing a “quantum phase magnification” method is also implemented. This method allows for entanglement-enhanced measurements without low-noise detection. We perform squeezed-state metrology 8dB below the standard quantum limit with a detection system that has a noise floor of 10dB above the standard quantum limit. Finally, the highly non classical nature of the squeezed states created is discussed, and the collective measurements of our state showing Bell correlations significant to 124 standard deviations are presented.

Acknowledgments

No person is an island, or as a physicist would say, no person is a closed system. And I am no exception to that rule. In fact I am a prime example of it, evidenced by all people that have shown me immense amounts of support and love over my life, including these last six years, without whom I would not have been able to make it through my Ph.D.

In order to avoid writing a whole book's worth of pages, I have unfortunately had to greatly underestimate my gratitude to the people in this acknowledgement, but hopefully I can at least give you a glimpse of how much they have done for me.

I would like to thank my advisor Mark Kasevich for giving me the opportunity to do some fantastic research with him. You have always been very supportive of me and I have learnt a lot from you over the years. In addition to your immense knowledge of physics and your incredible intuition about the way experiments work (“we’re not building BMWs, we’re building Fiats, so we better get the data while the experiment is working!”) you have a very sharp sense of humor (“never trust a physicist in a sports jacket... it means they’re about to ask you for money!”) and most importantly, you have the experience, insight and willingness to not only ask which experiments can be interesting or feasible, but which ones will really help to advance the state of the art of the field in a significant way. This is a school of thought that I have become a 100% a student of, and is a general attitude that I have adopted in both my professional and personal life.

Thank you to my readers Amir Safavi-Naeini and Jason Hogan, for not only diligently reading my thesis and giving me pertinent feedback, but also for the many things you have taught me through your classes and through our conversations on various topics ranging from cavities and atom interferometers to airlifting cows and camels carrying bananas. Thank you to Mac Beasley and Art Owen for being on my defense committee and for all the physics and statistics that I've learnt from you.

Onur Hosten, you're probably one of the clumsiest people I have ever met. I'm honestly surprised that you're still alive! I always get scared that you're going to break something or someone when you start playing around with one of the bouncy balls in the office. But when I see you in the lab, in front of a computer or writing on a whiteboard, it's a whole other situation. Whether you're fixing the equipment, upgrading our experiment, doing a theoretical calculation or a simulation, or coming up with the big ideas of where to take the experiment next, I've never seen someone do it like you do. And to top it off you're a excellent teacher with tons of patience. Thank you for being my pseudo-mentor and Godfather. I owe much of my success as a graduate student to you.

Thank you Nils Engelsen for being a great senior graduate student. You are really a knowledgeable physicist who has mastered the art of sarcasm and the science of making coffee. And when you sarcastically talk about physics while making coffee... it's a real treat to watch! And thank you for everything you've taught me, ranging from how AOMs work to all the tricks in FIFA. I'll never forget the time you came in on a weekend when I called you to tell you I accidentally unlocked the lasers! And I'll always remember your quote "it's more important to all agree on the correct answer than to show that you are the one who found it". It's been an honor working alongside you for most of my graduate career.

Thank you to my junior grad student Yunfan Wu for always being so optimistic and enthusiastic. I hope you never change that! And thanks for putting up with my weird taste in music. I hope I managed to teach you as much as you have taught me! I'm happy that you will be taking over the experiment. And thank you Ben Pichler. Even though we only worked together for a few months, it was a real pleasure. Both of you are very impressive and capable and I'm sure you'll have great success in your

graduate careers and beyond! And to Julián Martínez-Rincón, it was great to meet you and I look forward to our chats in the future!

Thank you to the rest of the past and present Kasevich students, postdocs and staff scientists: Catherine Kealhofer, Brannon Klopfer, Alex Sugarbaker, Christoph Kohstall, Joshua Francis, Gunnar Skulason, Seth Foreman, Peter Asenbaum, Susannah Dickerson, David Berryrieser, Chris Overstreet, Christine Donnelly, Kaspar Sakmann, Raphaël Bouganne, Fan Xiao, Tim Kovachy, Sheng-wei Chow, Patrick Medley, Michael Minar, Stewart Koppell, Thomas Juffmann, Sean Roy, Remy Notermans, Naceur Gaaloul, Alex Stibor, Fufang Wen and Brian Schaap. You are all highly intelligent people that are also very genuine. Thank you for all that you've taught me throughout the years and for all the good times. Getting those "lunch in 5?" messages would always make me happy :) Special shout-out to Brannon who, unfortunately for him, had to share an office with me for most of our graduate careers. I owe you a lot for all the food that I stole from you, but more importantly for all the times that I would walk in the office and feel better after seeing you typing away at your Leenux computer with your 5 monitors and that sweet sweet window manager. Thanks for everything dude!

Thank you to all the fantastic administrators with whom I have had the pleasure to work with, especially Ping Feng, Sha Zhang, Paula Perron and Claire Nicholas. You really made my life so easy despite my complicated administrative situations.

Thank you to everyone in the Schleier-Smith lab and everyone on the 2nd floor of Varian. Varian was a really great place to work in thanks to all of you.

Thank you to all the professors, teachers and staff that I have had the pleasure to interact with at Stanford who have taught me so much and helped me throughout my Ph.D.

Everyone that I have thanked thus far has been directly instrumental in enhancing my professional life at Stanford, some of whom have of course become my very close friends. As you can imagine I also have other people in my life that I have a purely personal relationship that have done immense amounts for me during my Ph.D. To keep this acknowledgment

to a reasonable length I will be even briefer in my thank-yous to them. I do sincerely apologize to them and I want them to know that they mean a lot more to me than I am capable of expressing here.

Thank you to all my many many friends, extended family and mentors at Stanford and around the world who have taught me so much and have brought positivity to my life throughout the years. There are really too many of you to name here but you know who you are, and I also know who you are!

Thank you to my old friends from back home. There are too many memories here to list but whenever I see you, wherever in the world it may be, you make it feel like home. A special thanks to Gokul Ramakrishnan, my brotha from another mothah, Nicolas Pitteloud, my hero that I always try and imitate, Nicolas Jutigny, the soldier that'll be OK no matter what, Alex Drake, one of the funniest guys I know, Adam McClure, so chill no matter what, Yann Micuta, for letting me make your home my home, Gilead Amit, for always showing me a different perspective on life, Santiago Godard, the person I wish I was as suave as, Julia Paranhos, for your amazingly positive vibes and Florian Thirot, one of the cheekiest lads I know. Merci à Adrien Soumaille, mon fréro pour la vie, et à mon petit frère William Dufaux, pour tous tes Snaps et de toujours être OP pour trainer avec moi quand je rentre en Suisse.

Thank you to my 311 friends from London: Pablo Mateos-Rodriguez, Rauf Gearing and Ricardo Smith. I couldn't have asked for better college flatmates and I always smile when I wake up to your whatsapp messages. I've learnt an incredible amount from you and you've really been an inspiration to me.

Thank you Judy Kroo, my first Stanford friend! I'll never forget the memories, from that time we went to Target to buy ALL the things, to the times we ran the dish together, to our drives up Page Mill, to talking about all the people we hate and love.

Thank you Emily Davis, my milkshake buddy, bike-home buddy, one-time gym buddy and plane buddy! Thank you for all the times that you've made my day better.

Thank you Raghu Mahajan for the many coffees, lunches and Inchin's, and for the many conversations and experiences ranging from dancing to bollywood songs to discussing the nature of reality. Thank you for always having my back no matter

what.

Thank you Lucas and Zahara Zipp for being a permanent part of my life at Stanford. You really kept me sane throughout my graduate career and have been better friends to me than I can ever be to you. Thank you for everything we've shared together.

Thank you Akash Maharaj and Woubzena Jifar. I'm so grateful for having you as my housemates. I am extremely lucky to get to live with you and home at Stanford has become wherever we're living together. I could have never made it through grad school without you.

Nisha Garimalla. You have seen me at my absolute worst and yet you never walk away from me. You have been a better friend to me than anyone could ever ask for. You've done more for me than anyone should. I am forever grateful and it's been a true blessing having you in my life. Thank you.

Thank you to my aunt and uncle, Prabha chithi and Siddharth chithappa, for giving me a home away from home and letting me thoroughly abuse your hospitality.

Thank you to my cousin Divya, for hanging out with me even though you're way cooler, smarter and more successful than I am.

Thank you to my nephews and niece: Kiran, Naveen and Diya Bronevetsky. Being with you is a humbling experience and always makes me realize that my problems are not important. You truly are joy in its purest forms.

Thank you to my brother-in-law Gregory Bronevetsky, for treating me like your own brother since the first day I met you. Among the plethora of things you've done for me, I'll never forget how you helped me settle down on my first day at Stanford.

Thank you to my sister Raga Krishnakumar, for always being there for me all the time and never expecting anything in return. For being the big sister everyone should have despite me being the spoilt bratty little brother.

And finally thank you to my parents Jayalakshmi and Velamur Krishnakumar. Most of everything that I have ever managed to accomplish in my life, including this Ph.D., has been because of what Thayaar and Perumal have given me through you. Thank you for everything.

Contents

Abstract	iv
Acknowledgments	v
1 Introduction	1
2 Modeling the atom-cavity interaction	3
2.1 ^{87}Rb atoms as an ensemble of spin- $\frac{1}{2}$ particles	3
2.1.1 A single ^{87}Rb atom	3
2.1.2 An ensemble of ^{87}Rb atoms	6
2.2 The empty cavity	8
2.3 Atom cavity interaction	9
2.4 Spin-Flips	12
2.4.1 D ₂ line spin flip probabilities	12
2.4.2 D ₁ line spin flip probabilities	15
3 Apparatus	17
3.1 Trapping and cooling the atoms	17
3.2 Homodyne detection system	21
3.3 Initial state preparation	22
3.4 Atom/cavity parameters	24
3.5 Fluorescence detection with the CCD camera	24

4 Measurement Based Squeezing	27
4.1 General Procedure	28
4.2 The Three Pillars	29
4.2.1 Shot Noise Measurements	29
4.2.2 Reduction in Variance	31
4.2.3 Coherence	32
4.3 Metrological Enhancement	32
4.4 Particle Entanglement	33
4.5 Pre-Squeezing	35
4.6 Clock measurements	37
4.7 Anti-Squeezing	38
4.8 Squeezing limitations	39
4.8.1 Cavity broadening due to atom absorptions	40
4.9 Coupling inhomogeneity	42
4.10 Maintaining squeezing after the release of atoms into free space . . .	43
4.10.1 Photons needed to image atoms with fluorescence below shot noise	46
5 Quantum phase magnification	49
5.1 General Procedure	50
5.2 Coherent state magnification	53
5.3 Squeezed state magnification	55
5.3.1 Squeezed state generation	56
5.3.2 Pulse sequences for the experiments	58
5.3.3 Noise re-focusing with squeezed states	60
5.4 The shearing interaction in the atom-cavity system	60
5.5 Experimental Extraction of the magnification parameters	63
5.6 Effects of fluctuations in experimental parameters	64
5.7 Limits	65
5.8 Generalization to many systems	67

6 Bell Correlation Measurements	70
6.1 Theory	71
6.2 General Procedure	73
6.3 Obtaining a Bell's witness with squeezed states	75
6.4 Entanglement depth	77
6.5 Conditional squeezing and Bell witnesses	79
6.6 Modeling atom-cavity coupling inhomogeneities	80
6.7 Calculating entanglement depth with nonsymmetric coupling	81
6.7.1 Use of $\sqrt{S_x^2 + S_y^2}$ for the calculation of entanglement depth .	83
6.7.2 Symmetric and nonsymmetric coherence	86
6.8 Standard Error Calculations	87
A Uncertainty Calculations	88
A.1 Confidence interval on the variance of a normally distributed variable	88
A.1.1 The square of a standard normal random variable	89
A.1.2 Sum of χ^2 -distributed variables	89
A.1.3 The variance of the empirical variance	90
A.2 The pooled variance	91
A.3 Variance of the empirical second moment	93
B Quantum Fisher Information	96
B.1 Definitions	96
B.2 Properties of Mathematical Objects	97
B.2.1 Density operator properties	97
B.2.2 Trace properties	97
B.2.3 Hermitian Conjugate Properties	98
B.2.4 Cauchy Schwarz Inequality for complex matrices.	98
B.3 Calculating the Quantum Cramér-Rao Bound	98
B.4 Acknowledgements	101
C Cavity Optomechanics of our system	102

List of Tables

List of Figures

2.1	^{87}Rb D ₂ transition hyperfine structure	4
2.2	m_F sublevels of the ^{87}Rb ground states	5
2.3	Three important energy levels of ^{87}Rb	6
2.4	Coherent state on a Bloch sphere	9
2.5	Selected Rubidium Transitions	13
2.6	^{87}Rb D ₂ 780nm absorption transitions	13
2.7	^{87}Rb D ₂ 780nm emission transitions	14
2.8	^{87}Rb D ₁ 780nm absorption transitions	15
2.9	^{87}Rb D ₁ 780nm emission transitions	15
3.1	Picture of the lab	18
3.2	High-Level View of the Apparatus	19
3.3	MOT setup	20
3.4	Detection system	23
3.5	Picture of the cavity	25
3.6	Image from our fluorescence detection	26
4.1	Squeezing Apparatus Setup	29
4.2	Shot Noise Measurements	31
4.3	Reduction in Variance	32
4.4	Coherence Measurements	33
4.5	Largest Inferred Metrological Enhancement	34
4.6	Inferred entanglement depths, quantifying multi-particle entanglement.	36
4.7	Clock Measurements	38

4.8	Inhomogeneity Analysis	44
4.9	Free Space Squeezing	46
4.10	Free Space Squeezing Coherence	47
4.11	Atom-Cavity coupling as a function of wait time	48
5.1	Conceptual description of quantum phase magnification	51
5.2	Experimental setup implementing phase magnification	53
5.3	Characterization of the basic magnification process with CSSs	55
5.4	Magnification process with noise re-focusing using 8 dB squeezed spin-states	57
5.5	Experimental pulse sequences.	59
6.1	Spin-squeezed states used in Bell's Witness demonstration	74
6.2	Rabi oscillations to demonstrate coherence	75
6.3	Bell correlation witness	76
6.4	Entanglement depth and Bell correlation boundaries	78
6.5	Entanglement depth bounds	84

Chapter 1

Introduction

Metrology is the science of measurements, and the overarching goal of metrologists is to try and come up with ways to measure various physical quantities as precisely as possible. These quantities include time, acceleration, gravitational fields, distances and magnetic fields. Atom sensors, such as atom interferometers [1] and atomic clocks [2], are a class of instruments that can measure such quantities with a very high precision. To date, the state of the art atomic clocks and atom interferometers use uncorrelated atoms, which gives them a fundamental precision limit that scales as \sqrt{N} where N is the total number of atoms being used by the sensor. This limit is known as the standard quantum limit or SQL [3].

Quantum metrology is the science of exploiting quantum entanglement to surpass the SQL i.e. to have a precision that scales better than \sqrt{N} . One of the holy grails of the field of quantum metrology is to reach the best possible scaling of N known as the Heisenberg limit [4, 5]. Although this has not been achieved to date in the context of creating a practical sensor, there have been many advances towards attaining it, including the pushing the boundaries of creating spin-squeezed states [6]. This thesis focuses mainly on the creation of highly spin-squeezed states of ^{87}Rb atoms with the help of a cavity and proof-of-principle demonstrations of measurements that exploit these spin-squeezed states to groundbreaking levels.

In Chapter 2 I go over some theory modeling the atom-cavity interaction followed by a brief explanation of the apparatus used in our experiments in Chapter 3. Following

that, in Chapter 4 I discuss our experiment in which we created 20dB spin-squeezed states [7]. Then in Chapter 5 I present how we demonstrated a technique to be able to resolve quantities to a precision below the SQL by using measurements that are limited to above the SQL [8]. Finally in Chapter 6 I discuss how the highly squeezed states described in Chapter 4 contain Bell correlations to an unprecedented degree of statistical significance [9].

Just a note: my former labmate Nils J. Engelsen, whom I worked together with on the experiments presented in this work, submitted his very well written thesis less than a year ago [10]. Since there are many aspects of our experiments which he has written in great detail about, there are certain sections of my thesis in which I have purposefully been brief and refer to his thesis if the reader is interested in more details. On the other hand, I cover other aspects to some more detail which I am more familiar with. However this work is self-contained and although I would recommend reading Nils' thesis independently, the reader does not need to have read his thesis to have an overall understanding of this work.

Chapter 2

Modeling the atom-cavity interaction

In this chapter I will discuss how we model our ^{87}Rb atoms as an ensemble of two-level systems and its interaction with light mediated by a cavity. In § 2.1 I will first present the relevant energy levels and how we use them to create a simplified model of a ^{87}Rb atom as a spin- $\frac{1}{2}$ particle and then discuss the Hamiltonian and the commutation relations of an ensemble of spin- $\frac{1}{2}$ particles in a symmetric subspace. I will then switch gears in § 2.2 and describe the Hamiltonian of a cavity probed with an electric field and in § 2.3 I will describe the whole system i.e. an ensemble of spin- $\frac{1}{2}$ particles in a cavity probed by an electric field. Finally in section § 2.4 I will discuss the additional effects of spin-flips caused by the light-atom interaction.

2.1 ^{87}Rb atoms as an ensemble of spin- $\frac{1}{2}$ particles

2.1.1 A single ^{87}Rb atom

To describe the ^{87}Rb atom I will be using what has now become the canonical reference for all information pertaining to the ^{87}Rb atom, “Rubidium 87 D Line Data” by Prof. Steck [11]. Let us start by looking at the D_2 transition hyperfine structure in ^{87}Rb in Figure 2.1.

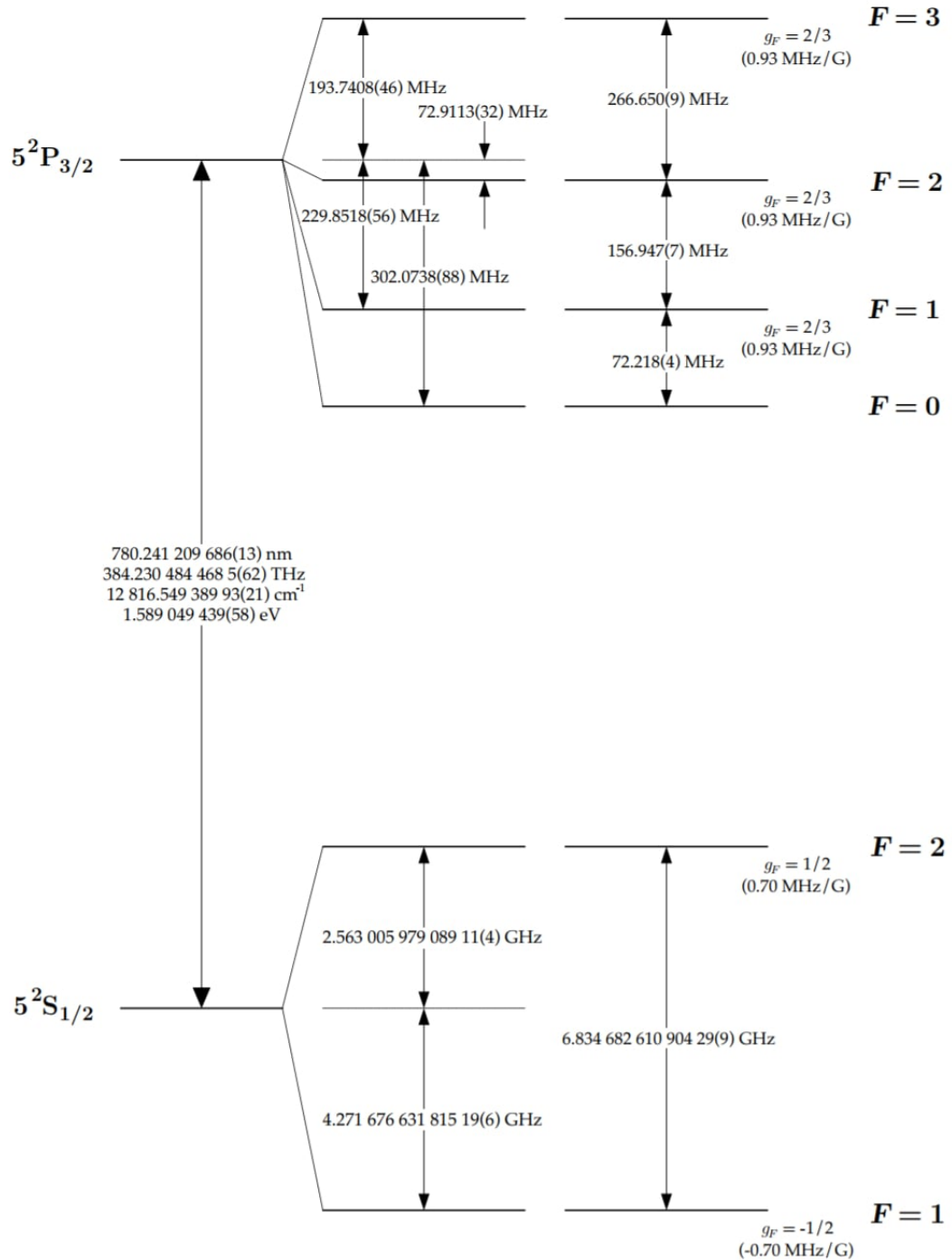


Figure 2.1: ^{87}Rb D₂ transition hyperfine structure, with frequency splittings between the hyperfine energy levels. The figure and caption are taken from [11]. The excited-state values are taken from [12], and the ground-state values are from [13]. The approximate Landé g_F -factors for each level are also given, with the corresponding Zeeman splittings between adjacent magnetic sublevels.

If we now look at just the $5^2S_{1/2}$ ground state hyperfine levels, we can split the $F=1$ and $F=2$ ground states into their $2F+1$ magnetic projections onto their quantization axis (m_F sublevels) after applying a constant magnetic field as shown in Figure 2.2.

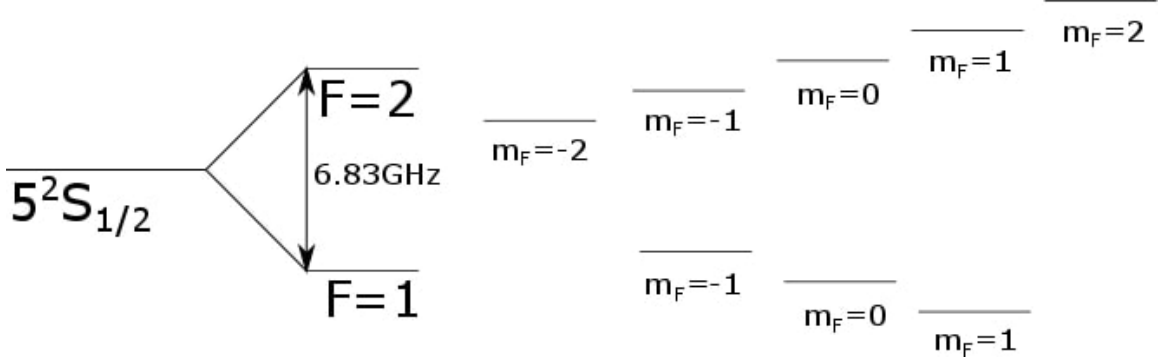


Figure 2.2: The m_F projections of the two hyperfine levels of the ground state of ^{87}Rb with the degeneracy lifted after applying a constant magnetic field

The magnetically insensitive sublevels $F=2$, $m_F=0$ and $F=1$, $m_F=0$ are known as the “clock states” and are two states we will use to describe ^{87}Rb as a two-level system. We will denote these states as $|\uparrow\rangle$ and $|\downarrow\rangle$ respectively. The fact that they are magnetically insensitive mean that they are not prone to first order Zeeman shifts and hence are more robust against stray magnetic fields.

In addition, we will define the $5^P\text{S}_{3/2}$ level as the “excited state” and denote it as $|e\rangle$. We now have a two-level system ($|\uparrow\rangle$ and $|\downarrow\rangle$) with an excited state ($|e\rangle$) as depicted in Figure 2.3. Now a single rubidium atom can be described as a pseudo spin- $\frac{1}{2}$ particle.

The Hamiltonian of this single particle can be written as

$$\begin{aligned} H_{a,single} &= -\hbar \frac{\omega_{HF}}{2} |\downarrow\rangle \langle \downarrow| + \hbar \frac{\omega_{HF}}{2} |\uparrow\rangle \langle \uparrow| + \hbar\omega_p |e\rangle \langle e| \\ &= \hbar\omega_{HF} j_z \end{aligned} \quad (2.1)$$

where ω_{HF} and ω_p are the frequencies corresponding to the transitions shown in Figure 2.3 and j_z is defined as $\frac{1}{2}(|\uparrow\rangle \langle \uparrow| - |\downarrow\rangle \langle \downarrow|)$. In free space, ω_{HF} is about $2\pi \times 6.83 \times 10^9$ (Figure 2.1). In the actual experiment there is the atoms are trapped in a

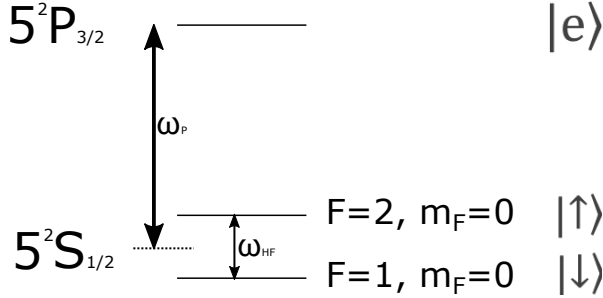


Figure 2.3: The three energy levels of ^{87}Rb depicting the clock states ($|\downarrow\rangle$ and $|\uparrow\rangle$) and excited state ($|e\rangle$) along with the hyperfine transition (ω_{HF}) and probe frequency (ω_P).

1560nm lattice which causes a small differential AC-Stark shift between the two states which is negligible (which is elaborated on in Section 3.3.3 of Nils' Thesis [10]). When going from the first step to the second in Equation 2.1, we ignore the $\hbar\omega_p |e\rangle \langle e|$ term by adiabatically eliminating the excited state. More details are explained in §2.3 but for now we can think of it as just setting $\langle\psi| \hbar\omega_p |e\rangle \langle e|\psi\rangle \approx 0$ where $|\psi\rangle$ is the state of the atom, i.e. the probability that the atom is in the $|e\rangle$ state at any point in time is low enough that we can approximate it to zero.

2.1.2 An ensemble of ^{87}Rb atoms

With N spin- $\frac{1}{2}$ particles each with spin $\mathbf{j} = \frac{1}{2}$, we have a system with a total spin of

$$\begin{aligned} \mathbf{J} &= \sum_{i=1}^N \mathbf{j}_i \\ &= \sum_{i=1}^N \frac{1}{2} \mathbf{\hat{z}} = \frac{N}{2} \mathbf{\hat{z}} \end{aligned}$$

with projections of that total spin into components labeled J_x, J_y and J_z which are the sum of their individual components $\sum_{i=1}^N j_{x,i}, \sum_{i=1}^N j_{y,i}$ and $\sum_{i=1}^N j_{z,i}$ respectively. These spin components have the following commutation relation:

$$[J_l, J_m] = i\hbar\varepsilon_{lmn}J_n \quad (2.2)$$

where l, m, n are the orthogonal spatial components x, y, z in any cyclical order and ε_{lmn} is the Levi-Civita symbol. This can be derived from the definition of the orbital angular momentum components:

$$\begin{aligned} (L_x, L_y, L_z) &= \mathbf{r} \times \mathbf{p} \\ &= \begin{vmatrix} \mathbf{i} & \mathbf{j} & \mathbf{k} \\ r_x & r_y & r_z \\ p_x & p_y & p_z \end{vmatrix} \end{aligned}$$

and then using the canonical commutation relation [14] $[r_l, p_m] = i\hbar\delta_{l,m}$. These commutation relations lead to the uncertainty relationship

$$(\Delta J_l^2)(\Delta J_m^2) \geq \frac{\langle J_n \rangle^2}{16} \quad (2.3)$$

which can be derived using the Robertson-Schrödinger uncertainty relationship [15, 16]. Again l, m, n are the orthogonal spatial components x, y, z in any cyclical order. A state for which ΔJ_l^2 and ΔJ_m^2 are equal is known as a coherent spin state (CSS) which has the property that ΔJ_l^2 (and ΔJ_m^2) is equal to $\frac{\langle J_n \rangle}{4}$ or

$$\Delta J_l = \Delta J_m = \frac{\sqrt{\langle J_n \rangle}}{2} \quad (2.4)$$

The value in Equation 2.4 is known as the standard quantum limit (SQL) or atomic shot noise. ‘Spin-squeezing’ [6, 17] is act of reducing the noise in one of the quadratures (say J_l) to below $\frac{\sqrt{\langle J_n \rangle}}{2}$ (and also causing the noise in the orthogonal quadrature, in this case J_m , to increase). If all the particles are pointing in the same direction (i.e. have the same expectation values in all 3 spin components), we say that the particles

are in the “symmetric subspace”. A more formal definition of an ensemble of particles in a symmetric subspace is an “N-particle pure state that remains unchanged by permutations of individual particles” [18]. These symmetric states can be visualized and defined on the surface of a Bloch sphere. There are many functions that can be used to define these states on a Bloch sphere (such as the Glauber-Sudharshan P function [19–22] and Husimi Q-function [22–24]) but we will be using the Wigner function [22, 25, 26] which in our case essentially depicts the probability distribution of measuring a value for a given spin component. For example the Wigner function of a coherent spin state (CSS) is shown in Figure 2.4. It is worth noting that these are not joint probability distributions of all spin components but the probabilities of a single measurement once a basis is chosen. This is because, as noted earlier in this section, the different spin components do not commute and hence measuring one of them will collapse the state and alter the distribution of the other components.

We can write down the Hamiltonian of this ensemble of N atoms as

$$\begin{aligned} H_a &= \sum_{i=1}^N \hbar\omega_a j_{z,i} \\ &= \hbar\omega_a J_z \end{aligned} \tag{2.5}$$

2.2 The empty cavity

In our experiment we use a near-confocal Fabry-Pérot cavity to enhance the atom-cavity interaction. When probing an empty cavity with a laser, we can write the Hamiltonian as

$$H_c = \hbar\omega_c a^\dagger a + \hbar\eta(a e^{i\omega_p t} + a^\dagger e^{-i\omega_p t}) \tag{2.6}$$

where ω_c is the resonant frequency of the cavity, ω_p is the frequency of the probe (as shown in Figure 2.3), η is the driving rate of the probe and a^\dagger and a are the creation

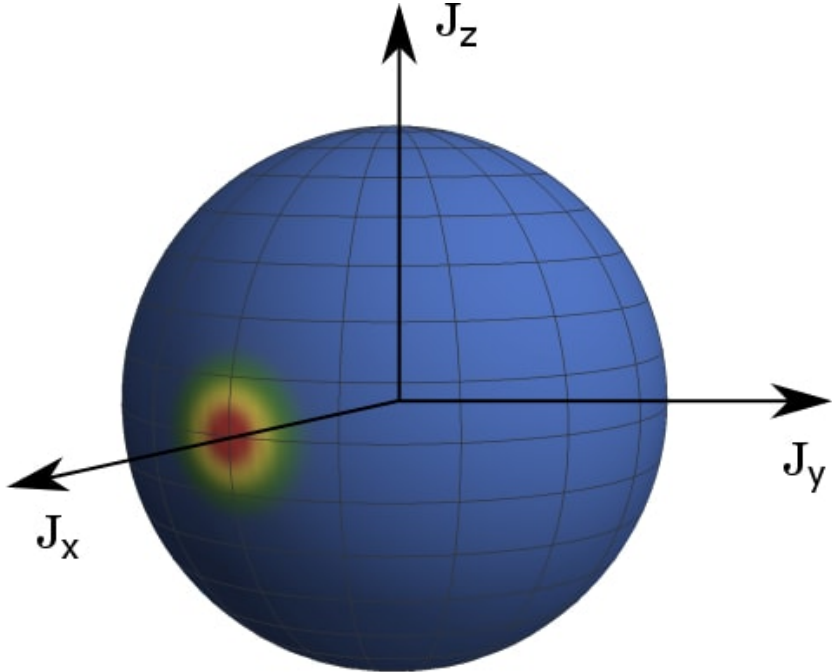


Figure 2.4: The Wigner function of a 50-50 superposition CSS (i.e. $(|\uparrow\rangle + |\downarrow\rangle)^{\otimes N}$) on a Bloch sphere.

and annihilation operators of the light field respectively. The first term represents the number of photons within the cavity and the second term represents the probe (we are ignoring the leakage term for now).

2.3 Atom cavity interaction

If we now insert the atoms at the center of our cavity, we obtain an interaction between the light field and the atoms, which can be written as

$$H_{int} = \sum_{i=1}^N -\hbar g(x)(\sigma_{i,\downarrow}^+ a + \sigma_{i,\downarrow}^- a^\dagger) + \hbar g(x)(\sigma_{i,\uparrow}^+ a + \sigma_{i,\uparrow}^- a^\dagger) \quad (2.7)$$

where $g(x)$ is the coupling constant [10] and $\sigma_{\downarrow(\uparrow)}^{+(-)}$ represent the pauli ladder operators where the superscripts denotes whether it is the raising (or the lowering operator) and the second subscript denotes whether it is acting on the \uparrow (\downarrow) state. For simplicity's sake, we will now look at the simpler system of a single 2-level atom whose two levels are $|\uparrow\rangle$ and $|e\rangle$.

$$H_{int,single} = \hbar g(x)(\sigma^+ a + \sigma^- a^\dagger) \quad (2.8)$$

This gives us a complete Hamiltonian (for a single atom) as

$$H_{single} = \hbar\omega_a\sigma_z + \hbar\omega_c a^\dagger a + \hbar\eta(ae^{i\omega_p t} + a^\dagger e^{-i\omega_p t}) + \hbar g(x)(\sigma^+ a + \sigma^- a^\dagger) \quad (2.9)$$

where ω_a is the transition frequency between $|\uparrow\rangle$ and $|e\rangle$ and σ_z is $|\uparrow\rangle\langle\uparrow| - |e\rangle\langle e|$. Equation 2.9 is known as the Jaynes-Cummings Hamiltonian [27]. We will now look at adiabatically eliminating the excited state to simplify this Hamiltonian. There are many ways of doing this, and I will briefly discuss the way in the lecture notes of Prof. Tobias Donner's FS2015 course [28]. The first step is to change the equation to the Hamiltonian picture with the unitary operator $U(t) = e^{i\omega_p t(\sigma_x + a^\dagger a)}$ which gives us

$$a \rightarrow U^\dagger a U = ae^{i\omega_p t} \quad (2.10)$$

$$\sigma^+ \rightarrow \sigma^+ e^{i\omega_p t} \quad (2.11)$$

We then move to the rotating frame of the probe using

$$\Delta_c = \omega_p - \omega_c \quad (2.12)$$

$$\Delta_a = \omega_p - \omega_a \quad (2.13)$$

We then adiabatically eliminate the excited state by stating that because on average there will be 0 atoms in the excited state, we can set $\dot{\sigma}^+$ and $\dot{\sigma}^-$ to 0. Solving the

Heisenberg equations of motions for these two (i.e. $\dot{\sigma}^+ = \frac{i}{\hbar}[H, \sigma^+] = 0$ and similarly for $\dot{\sigma}^-$) we obtain

$$\begin{aligned}\sigma^+ &= \frac{g(x)}{\Delta_a} a^\dagger \sigma_z \\ \sigma^- &= \frac{g(x)}{\Delta_a} a_z^\sigma\end{aligned}\quad (2.14)$$

We can then solve the Heisenberg equation for \dot{a} and inserting values for σ^+ and σ^- in Equation 2.14, we obtain

$$\dot{a} = -i\Delta_c a + \frac{ig^2(x)}{\Delta_a} a + i\eta \quad (2.15)$$

We then make a clever guess of the Hamiltonian that will give us Equation 2.15 which gives us

$$H_{single} = \hbar\Delta_a \sigma_z + \hbar\Delta_c a^\dagger a + \hbar\eta(a + a) + \hbar\frac{g^2(x)}{\Delta_a} a^\dagger a \sigma_z \quad (2.16)$$

We notice that the interesting term in the above Hamiltonian is the last one, which describes the detuning of the cavity. More specifically it corresponds to the additional phase shift that the light imposes and the atoms and that the atoms impose on the light from the interaction proportional to σ_z .

This same calculation can be done starting with full interaction terms (in Equation 2.7) after which the final result is

$$H = \hbar\Delta_a J_z + \hbar\Delta_c a^\dagger a + \hbar\eta(a + a) + \hbar\frac{g^2(x)}{\Delta_a} a^\dagger a J_z \quad (2.17)$$

This Hamiltonian is sufficient to describe interaction which leads to measurement based squeezing [29] since the interaction term is now $\hbar\frac{g^2(x)}{\Delta_a} a^\dagger a J_z$ which means that the phase shift imposed on the light by the atom is proportional to J_z . Taking the

ensemble of atoms to be in a coherent state (i.e. a superposition of J_z states), the light is in a superposition of phase-shifted coherent states after the interaction. However when it is measured it reduces the number of possible phase-shifted states it can be in (to within the measurement uncertainty) which in turn causes the atoms to reduce the number of possible J_z states that they can be in, hence creating a squeezed state. A full Hamiltonian (without using the adiabatic elimination of the excited state) which can be derived using input-output theory be found in Ref. [29]. When sending in a probe that is far off resonant to the cavity resonant frequency, the higher order terms that are ignored due to the adiabatic elimination in Equation 2.17 become relevant, and so a different formalism is required. This is examined further in §5.4 after putting it in context with the experiment

2.4 Spin-Flips

Now we look at the effects of spin-flips, i.e. the atoms flipping from $|\uparrow\rangle$ to $|\downarrow\rangle$ and vice-versa due to the absorption and re-emission of 780nm light.

2.4.1 D₂ line spin flip probabilites

In our experiment, the atoms are prepared in a superposition of the clock states (i.e. $|F = 1, m_F = 0\rangle$ and $|F = 2, m_F = 0\rangle$) and then a 780nm (i.e. D₂ line) π pulse is applied on them. This pulse is located half way between the 2 resonances, as shown in Figure 2.5.

This causes some of the population in both states to spin-flip when they spontaneously emit. Since the population in both states are coupled equally to the light, we can use the standard relative strengths of the dipole interactions to calculate the spin flips, specifically the population change due to these spin flips.

Probabilities going from ground to excited states

All probabilities from here on are calculated using state transition values found in ref. [30].

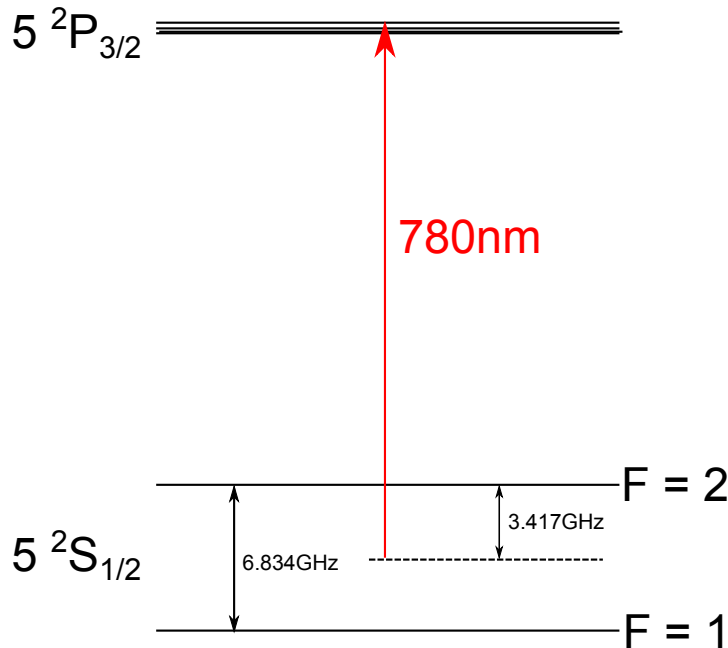


Figure 2.5: The relevant transitions for demonstrating spin-flips in the ^{87}Rb atom.

Since a π pulse is applied, we can assume that the states go from $m_F = 0 \rightarrow m_{F'} = 0$. Therefore, using the selection rule $\Delta F = \pm 1$ (along with $\Delta m_F = 0$ for π pulses), the probabilities for the excitations from each individual hyperfine state are shown in Figure 2.6.

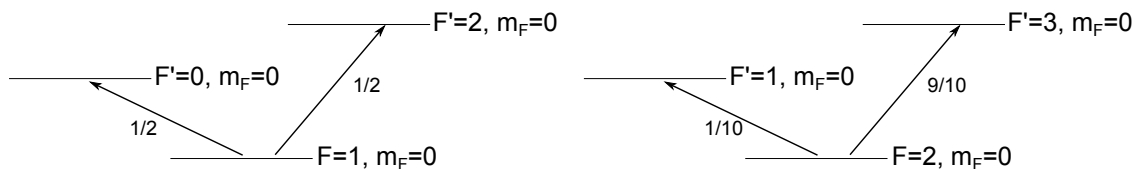


Figure 2.6: The relevant D_2 absorption transitions for demonstrating spin-flips in the ^{87}Rb atom.

Probabilities going from excited to ground states

After having gone to the excited states, the atoms can decay into several ground states, emitting π or σ^\pm . Therefore, using the selection rules $\Delta F = \pm 1$ and $\Delta m_F = 0, \pm 1$ we

have the transition probabilities shown in Figure 2.7.

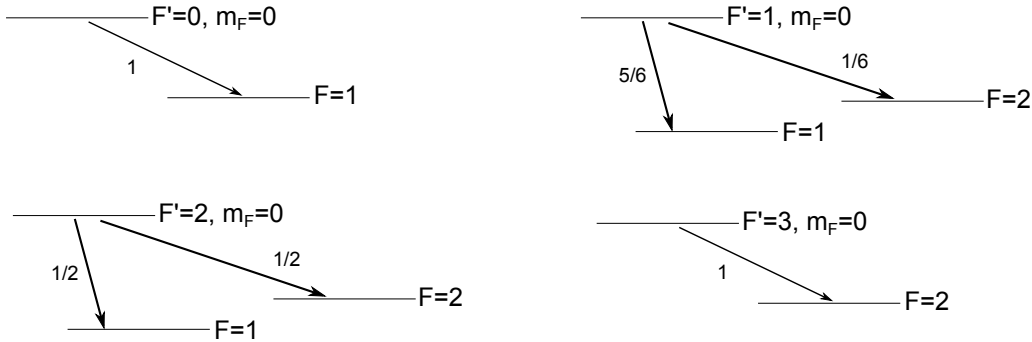


Figure 2.7: The relevant D_2 emission transitions for demonstrating spin-flips in the ^{87}Rb atom.

Probability of spin flips occurring

Using the above, we can calculate the probabilities for the spins to go from $F=1$ to $F=2$ and vice versa for every excitation:

$$\begin{aligned}
 P(|1, 0\rangle \rightarrow |2, m_F\rangle) &= P(|F = 1, m_F = 0\rangle \rightarrow |F' = 2, m_{F'} = 0\rangle \rightarrow |F = 2, m_F\rangle) \\
 &= \frac{1}{2} \times \left(\frac{1}{2} \times \frac{1}{2} \right) = \frac{1}{8} \\
 P(|2, 0\rangle \rightarrow |1, m_F\rangle) &= P(|F = 2, m_F = 0\rangle \rightarrow |F' = 1, m_{F'} = 0\rangle \rightarrow |F = 1, m_F\rangle) \\
 &= \frac{1}{2} \times \left(\frac{1}{10} \times \frac{5}{6} \right) = \frac{1}{24}
 \end{aligned} \tag{2.18}$$

This gives a total spin flip probability of $\frac{1}{6}$. Note that the first factor of $\frac{1}{2}$ outside the parentheses comes from the fact that we assumed 50-50 population distribution between the clock states.

Cavity shift caused by spin-flips

We can now calculate the total cavity shift due to spin flips by using the following quantities:

N - total number of atoms

m_s - number of spontaneous emissions per atom

δf - frequency shift per atom going from $|1, 0\rangle \rightarrow |2, m_F\rangle$ (which is the negative of the shift for atoms going from $|2, 0\rangle \rightarrow |1, m_F\rangle$)

$$\begin{aligned}\text{total cavity shift} &= N \times m_s \times \delta f \times (P(|1, 0\rangle \rightarrow |2, m_F\rangle) - P(|2, 0\rangle \rightarrow |1, m_F\rangle)) \\ &= Nm_s\delta f \left(\frac{1}{8} - \frac{1}{24} \right) \\ &= \frac{Nm_s}{12}\delta f\end{aligned}$$

2.4.2 D₁ line spin flip probabilities

Using the same method as above, the probabilities for the D₁ line shown in Figure 2.8, Figure 2.9 and Equation 2.18.

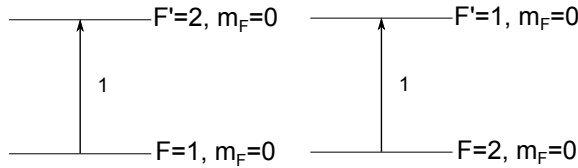


Figure 2.8: The relevant D₁ absorption transitions for demonstrating spin-flips in the ⁸⁷Rb atom.



Figure 2.9: The relevant D₁ emission transitions for demonstrating spin-flips in the ⁸⁷Rb atom.

$$\begin{aligned}
P(|1, 0\rangle \rightarrow |2, m_F\rangle) &= P(|F = 1, m_F = 0\rangle \rightarrow |F' = 2, m_{F'} = 0\rangle \rightarrow |F = 2, m_F\rangle) \\
&= \frac{1}{2} \times \left(1 \times \frac{1}{2}\right) = \frac{1}{4} \\
P(|2, 0\rangle \rightarrow |1, m_F\rangle) &= P(|F = 2, m_F = 0\rangle \rightarrow |F' = 1, m_{F'} = 0\rangle \rightarrow |F = 1, m_F\rangle) \\
&= \frac{1}{2} \times \left(1 \times \frac{1}{6}\right) = \frac{1}{12}
\end{aligned} \tag{2.19}$$

This gives a total spin flip probability of $\frac{1}{4}$. Again, the first factor of $\frac{1}{2}$ outside the parentheses comes from the fact that we assumed 50-50 population distribution between the clock states.

We see that this yields a higher spin-flip probability than the D₂ line and hence it is better to use the D₂ line.

Chapter 3

Apparatus

In this chapter I will briefly present how we create our entangled states and make measurements using our apparatus Figure 3.1. A much more in-depth presentation of the apparatus can be found in Nils' thesis [10], Geert's thesis [31] and ref. [32]. Nonetheless I will present a high-level overview for completeness' sake along with details of any new differences and upgrades of the apparatus that are not present in the references listed above.

A diagram depicting a high level overview of the apparatus can be seen in Figure 3.2. I will first discuss how we trap and cool an ensemble of ^{87}Rb atoms in the middle of a cavity with a Magneto-Optical trap. I will then explain how we prepare them in a superposition of the $|F = 1, m_F = 0\rangle$ ($|\downarrow\rangle$) and $|F = 2, m_F = 0\rangle$ ($|\uparrow\rangle$) ground states. This will be followed by a discussion on the measurement of the state and the atom/cavity parameters that affect this measurement. Then I will finally explain how we count our atoms with our camera.

3.1 Trapping and cooling the atoms

The main chamber consists of a rubidium source attached to a vacuum chamber made out of zerodur glass. This chamber houses a 2D magneto optical trap (MOT), 3D-MOT and a high finesse cavity. The MOT is a common technique used to cool and trap atoms in vacuum chambers and is explained in many references including

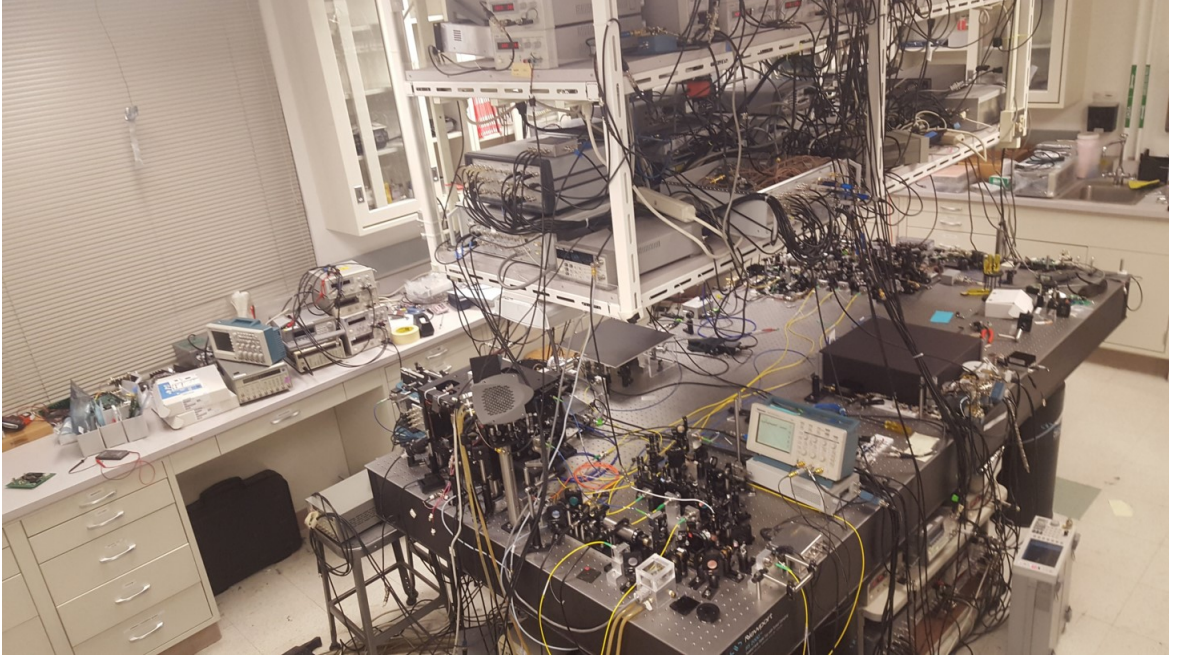


Figure 3.1: A full view of the lab. A few distinct features: the setup on the furthest end (top right) is where all the MOT and repump laser are. The fully covered black rectangular box on the table is our homodyne detection system. The grey box with black dots on top of a pole is our CCD camera which points to the center of our cavity which is located in behind it (not visible in this picture but is shown in Figure 3.5).

ref. [30]. Several laser/microwave sources are directed towards the center of the chamber: a 1560nm external cavity Redfern Integrated Optics (RIO) laser (used to create a trapping potential for the atoms), a microwave source (used to couple the two rubidium 87 ground states $|F = 1, m_F = 0\rangle$ and $|F = 2, m_F = 0\rangle$), several 780nm distributed Bragg reflector (DBR) lasers [33] from Eagleyard (used for generating the MOT, probing the cavity and separating the atoms) and a microwave source at the resonance frequency between the two clock states which is roughly 6.8GHz.

The MOT and repump lasers are locked to their respective frequencies using saturation absorption spectroscopy [34] and pass many optics including several acoustic-optic modulators (AOMs) [35]. These AOMs are voltage controlled by a digital signal processor (DSP) and can change the frequency shift of the input light on the order of $1\mu s$ during our experimental sequences. Figure 3.3 shows a schematic of the setup

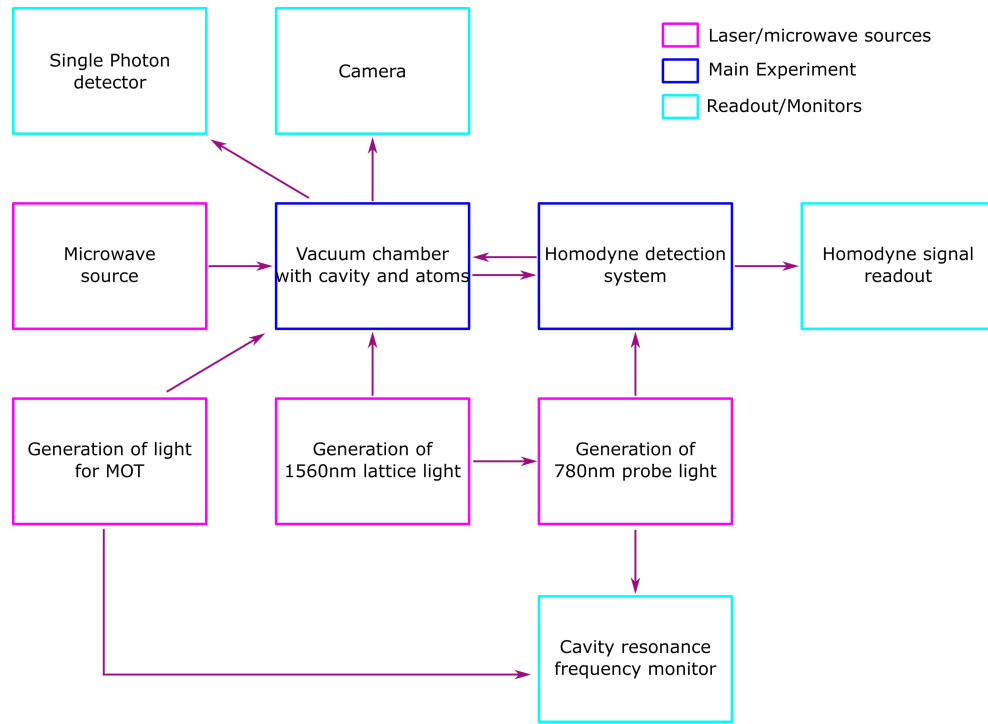


Figure 3.2: A high-level view of the full apparatus. The apparatus can be broken down into 3 sections: 1) The laser and microwave sources used in the experiment, 2) The main section where the light/atom interaction and entanglement takes place and 3) the monitors and readout apparatus where the measurements are recorded.

and a more in depth description of the lasers and the sequence can be found in [10].

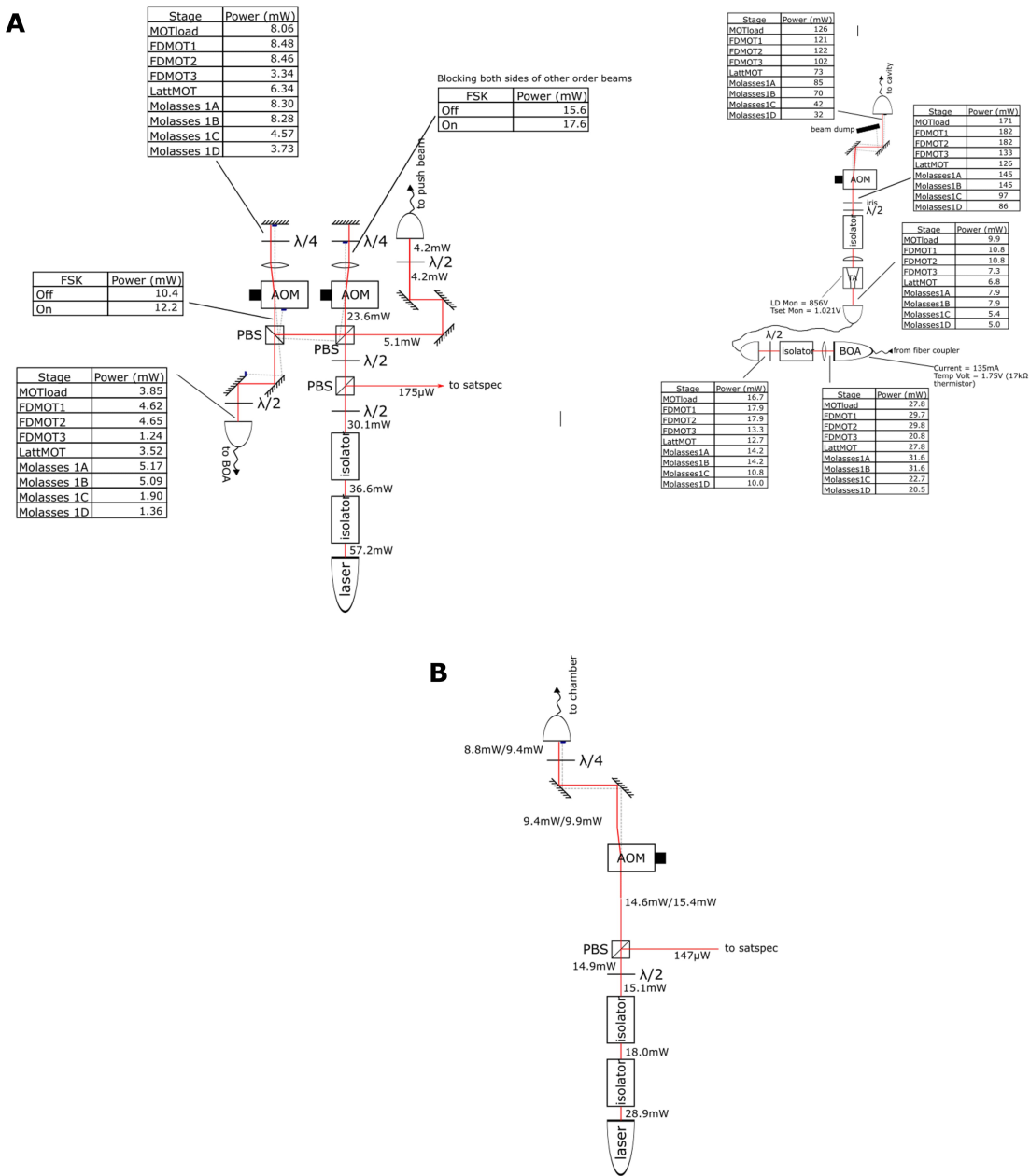


Figure 3.3: A schematic showing the setup for our A) MOT laser and B) repump laser.

The MOT coils are setup in the standard way for 2D and 3D quadrupole traps [30]. In addition, a 1560nm light is generated with a RIO laser. It is then locked to a scrubbing cavity, after which it seeds a 1560nm diode laser. This laser seeds a fiber amplifier. The output of that fiber laser is split into two paths: one path leads to a doubling crystal where it turns into the 780nm light we use for the probe, and the other path is modulated with sidebands and is locked to the main cavity. The light from the second path is set to be resonant with the cavity to create a standing wave lattice which is used to trap atoms [36]. The doubled 780nm light injects a diode laser (to get rid of amplitude noise). The light from that diode laser then enters an interferometer (which is the main component of the homodyne detection system) and is used as the probe for the cavity. Since the probe frequency is double that of the lattice frequency, the coupling of each atom to the probe is approximately uniform. The value for the coupling constant (Equation 2.17) g is an average over the position distribution of the atoms inside the lattice due to the finite temperature. The $25 \mu\text{K}$ atoms are distributed over about a thousand lattice sites. The root-mean-squared (RMS) of the atomic cloud size inside each $520 \mu\text{K}$ -deep lattice site is $17 \mu\text{m}$ in the transverse and 37 nm in the axial direction. The trap frequencies in the corresponding directions are 460 Hz and 205 kHz . We can vary the atom number in the experiment from 0 to 5×10^5 by changing the initial magneto-optical trap (MOT) loading time. There is some residual inhomogeneity in atom-cavity coupling due to thermal motion which is further discussed in § 4.9. A more detailed discussion of the 1560nm and doubled 780nm laser setup can be found in [10].

3.2 Homodyne detection system

The homodyne detection setup (Figure 3.4) is seeded with 780 nm light obtained by frequency doubling the 1560 nm lattice light, which is frequency stabilized to the main cavity following an intermediate stabilization step involving a scrubbing cavity. Thus, the 780 nm light is already stable in the short-term with respect to the cavity ($80 \text{ mHz}/\sqrt{\text{Hz}}$ level in the $0.2 - 4 \text{ kHz}$ band – about 8 Hz (RMS) stability). In the long term, thermal drifts in the cavity mirror coatings cause variations in the individual

cavity lengths seen by the 780 nm and 1560 nm light. During experimental cycles of 1s, the probe frequency can drift by 100 Hz (RMS); we correct the drift at the end of every cycle with an auxiliary empty cavity measurement. Using a 200 μ W local oscillator (80 MHz shifted from input) on the path going to the cavity of the homodyne system, the balanced detectors operate photon shot-noise limited from 10 Hz up to 5 MHz. Two 10 nW spectral components on the local oscillator path (offset by 78 MHz and 82 MHz from input) travel to the cavity and promptly reflect back from the first mirror to give a heterodyne beat-note signal (2 MHz) at the detectors. This signal is used to stabilize the interferometer path lengths via feedback onto the AOM in the local oscillator path. Stabilization covers the DC - 15 kHz frequency band, thus removing the influence of optical phase noise for the squeezing measurements. The local oscillator path also contains the probe (80 MHz offset from input), interfering with the local oscillator to form the homodyne signal after returning from the cavity. The overall detection efficiency limiting the achievable squeezing is $\varepsilon=0.16$. The breakdown is as follows: a factor of 0.50, since we collect light only from one cavity mirror; 0.57 due to loss in cavity mirrors; 0.80 backwards fiber coupling efficiency; 0.85, loss in isolator and other optical elements; 0.85, interferometer mode matching efficiency. Multiplying these factors results in the stated overall efficiency. Our ability to estimate the centroid of the cavity resonance frequency improves with the square root of the number of photons contained in a 200 μ s measurement pulse, and saturates around 15 Hz due to laser frequency instability.

3.3 Initial state preparation

After cooling and trapping the atoms, we apply a state purification procedure using optical pumping — with the cooling and re-pump lasers of the MOT — and microwave transitions to prepare the atoms in the lower clock state ($F = 1, m_F = 0$). We blast away the remaining atoms in the $F = 2$ ground state manifold with on-resonance light to further purify the states. We then adiabatically ramp up the lattice to a depth of 520 μ K to tightly trap the atoms with 17 μ m rms radius in the transverse direction. We end up with up to 5×10^5 atoms at 25 μ K prepared in the lower clock state. This

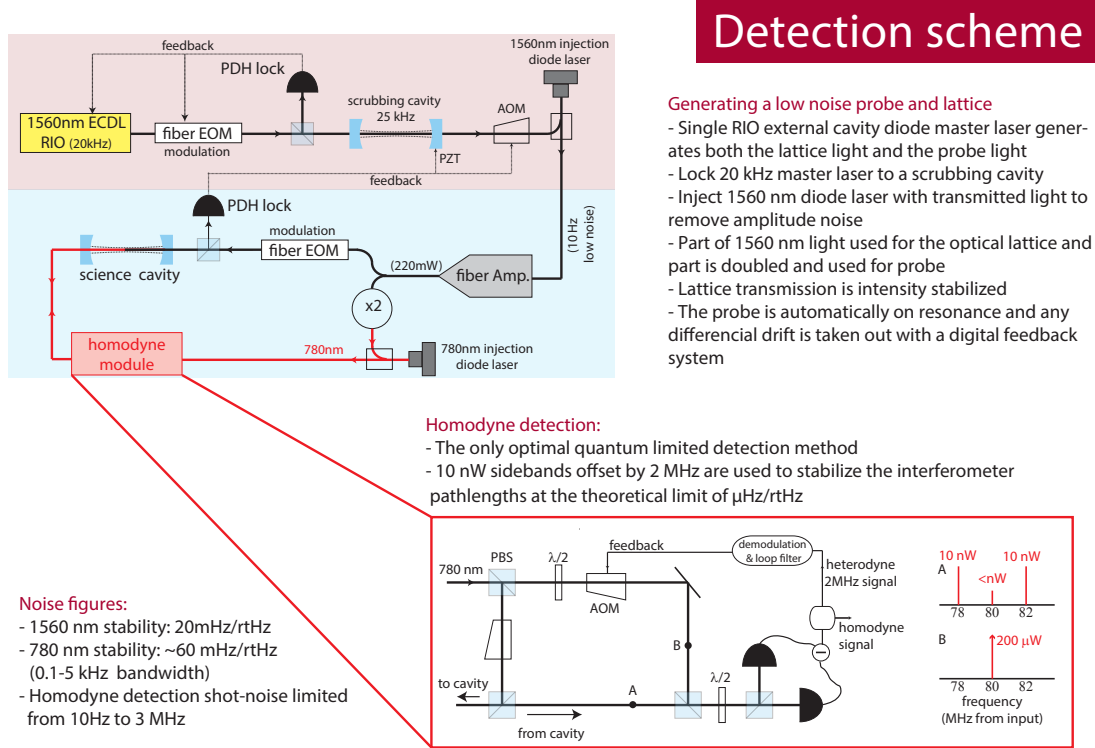


Figure 3.4: Diagram of the detection system showing the basic setup of the 1560nm laser, 780nm doubled laser and homodyne detection system.

state corresponds to a Bloch vector pointing to the bottom of the sphere.

To prepare CSSs aligned with the J_x -axis of the Bloch sphere — the starting point of our experiments — we apply a $\pi/2$ rotation about the J_y -axis. Physically, this rotation is accomplished by driving the to clock transition with on-resonance microwaves. The $\pi/2$ rotation is implemented in two-steps: $\pi/2_0 - \pi_{2\pi/3}$ (subscripts indicate relative phase between pulses). This composite rotation suppresses the microwave pulse area noise, suppressing technical noise levels below the relevant CSS noise level § 4.2.1. Experimentally, the absolute rotation angle is fine-tuned until the mean cavity resonance frequency shift is nulled.

3.4 Atom/cavity parameters

Our cavity is a near-confocal cavity that is about 10cm long with a decay rate of $\kappa = 2\pi \times 8\text{kHz}$ for 780nm light which can be broken down into $\kappa = 2\kappa_M + \kappa_L + \kappa_S$, where κ_M is due to mirror out-coupling, and κ_L is due to optical losses in the mirrors. The term due to atomic scattering can be expressed as $\kappa_S/\kappa_0 = NC(\Gamma/\omega_{HF})^2$, where $\kappa_0 = 2\kappa_M + \kappa_L$. The finesse of the cavity is 1.75×10^5 and for transitions from the clock states with π -polarized light, the single atom cooperativity is $C = 4g^2/\kappa_0\Gamma = 0.78$, with atom-cavity coupling $g = 2 \times 96.7\text{kHz}$, empty cavity decay rate $\kappa_0 = 2\pi \times 8.0\text{kHz}$, and atomic decay rate $\Gamma = 2 \times 6.06\text{MHz}$. The value for g^2 is an average over the position distribution of the atoms inside the lattice due to the finite temperature. The 25 μK atoms are distributed over about a thousand lattice sites. In addition, a spin-flip (discussed in § 2.4) causes a 5.5 Hz shift, a value calculated from the well-known atom-cavity parameters, and verified experimentally at 10% level with ac-Stark shift measurements for a known intra-cavity probe power.

3.5 Fluorescence detection with the CCD camera

An example of an image from our fluorescence detection can be seen in Figure 3.6 which we use to extract J_z in a single experimental shot. The difference in the number of total counts in the marked regions, after multiplication with a calibration factor, yields J_z . When trapped in the optical lattice, the atom cloud is cigar-shaped with an aspect ratio of ~ 10 . In order to obtain the images, we first turn off the lattice and immediately push the atoms in the $F = 2, m_f = 0$ state (bottom cloud) by illuminating the atoms for $7 \mu\text{s}$ from above with σ_+ -polarized light. This light is on resonance with the $F = 2$ to $F' = 3$ transition of the ^{87}Rb atoms and is at the saturation intensity. Since only the $F = 2$ atoms scatter the light, the $F = 1$ cloud remains unaffected. After the push, we allow 1.2 ms for the two clouds to spatially separate in free fall. During this time the clouds also expand and take a more spherical shape. Finally, we image the fluorescence from the two clouds for 2 ms on a CCD camera using the cooling and re-pumping lights of the MOT. The radius of the observed clouds is similar

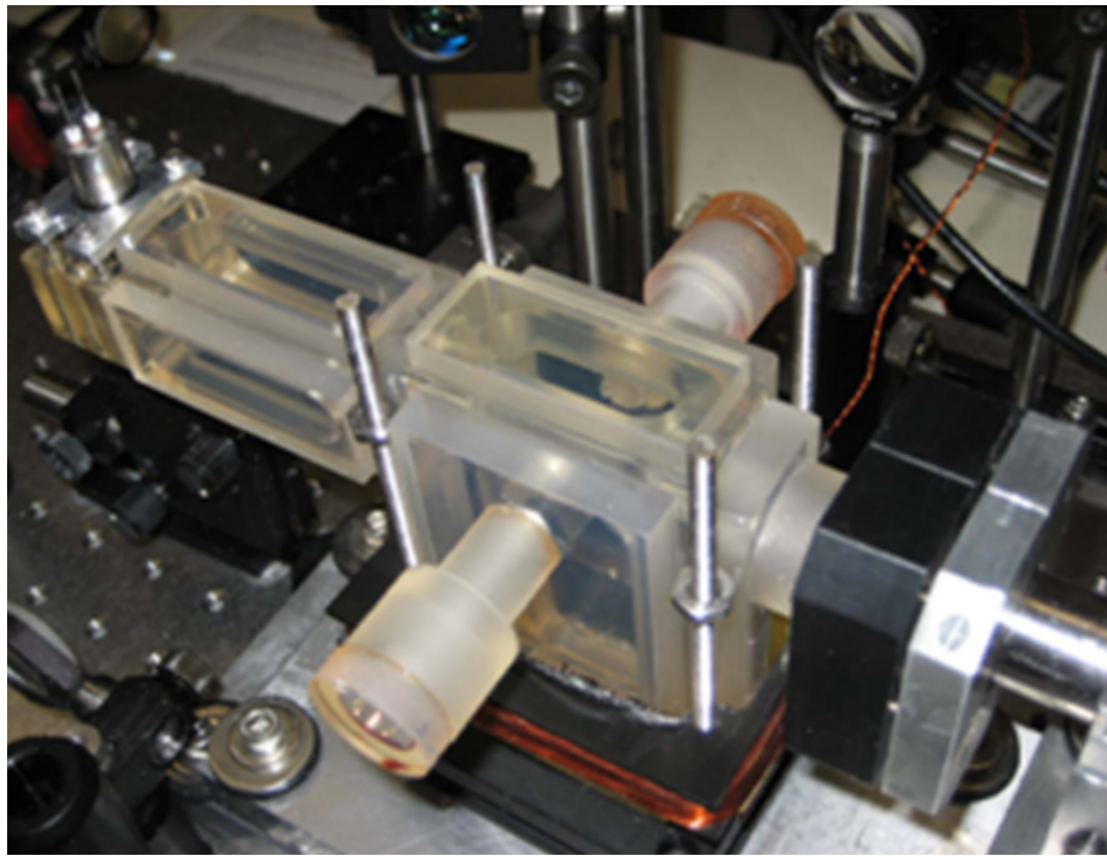


Figure 3.5: A picture of the cavity before it was installed in the apparatus.

to the original longitudinal size of the cloud inside of the lattice. The fluorescence detection setup has a technical noise floor of 1200 atoms rms which is $\sim\{15, 11\}$ dB in variance above the SQL for $\{2 \times 10^5, 5 \times 10^5\}$ atoms.

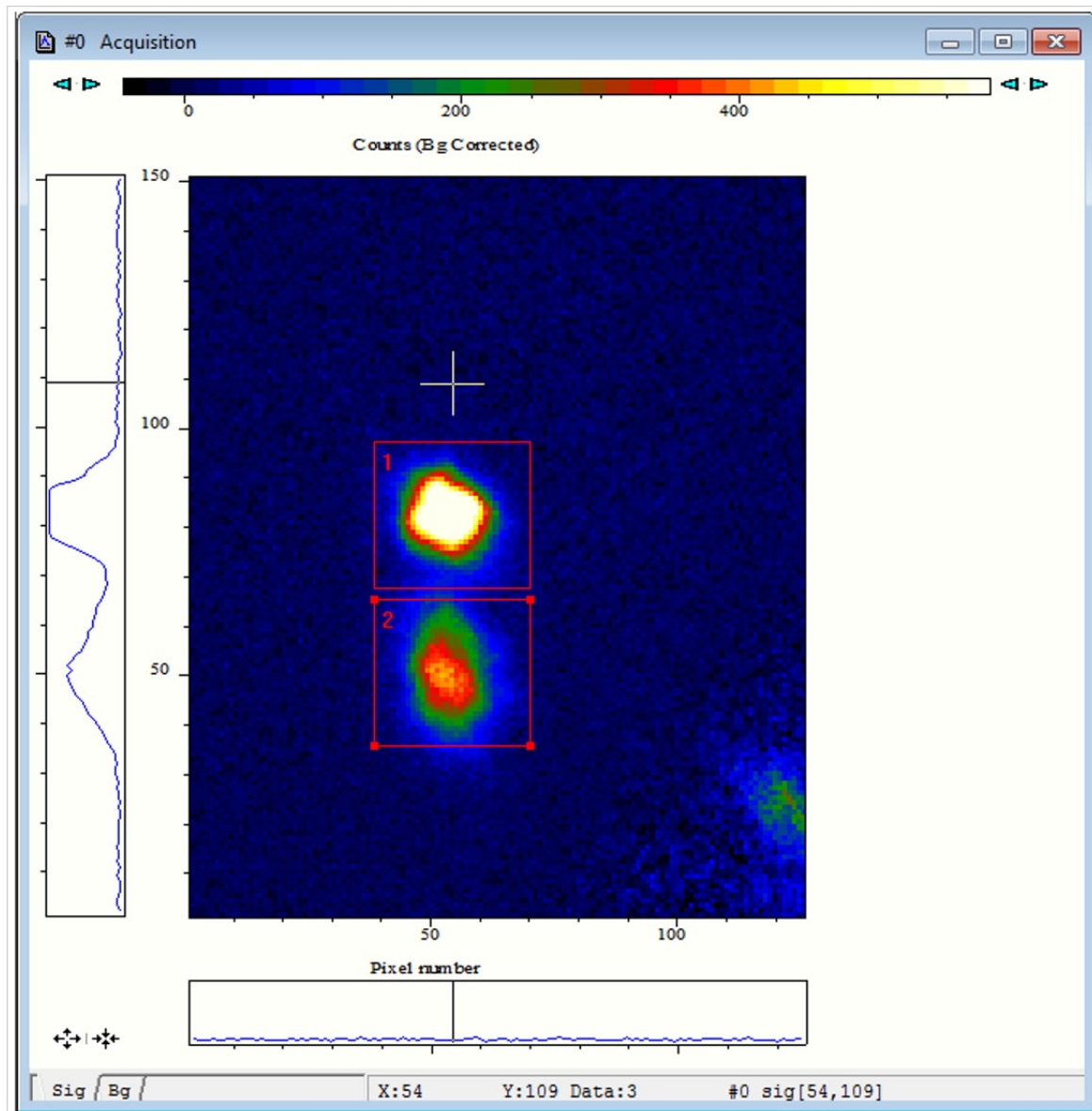


Figure 3.6: An image from our fluorescence detection showing the two states $|F = 1, m_F = 0\rangle$ (top) and $|F = 2, m_F = 0\rangle$ (bottom) after the push beam has acted on it.

Chapter 4

Measurement Based Squeezing

I will now present the work we did on creating 20dB spin-squeezed states, which was published in 2016 [7]

‘Spin-Squeezing’ [6] serves in redistributing the noise for making the observable of interest quieter than the Coherent Spin State (CSS) noise level, while still conforming to uncertainty relations. This process is non-classical as it introduces quantum entanglement into the system. The metrological improvement provided by squeezing is quantified by [17] $\chi^2 = \left(\frac{\sqrt{N}/2}{\Delta J_z} \cdot \frac{|\langle J_x \rangle|}{N/2} \right)^2$; the first factor represents noise reduction, whereas the second represents coherence loss. This quantity translates directly into reduction in resources needed to perform a specific measurement [20 dB ($\chi^2 = 100$) equivalent: 100-fold increase in atom number or reduction in averaging time].

In optical settings [37] and superconducting microwave circuits [38], squeezing in excess of 15 and 12 dB has been demonstrated respectively¹. Implementations in the interferometers of GEO-600 and LIGO gravitational wave detectors achieved 2.5 dB improvements [39]. Other demonstrations include noninvasive biological imaging [40]. Spin-squeezing has been shown in cold atomic ensembles both with interaction [41–43] and measurement [44–46] based methods. 5.6 dB-squeezed states [47] were used to obtain atomic-clock improvements up to 4.5 dB [48], and magnetometer enhancements up to 3.4 dB were observed in other experiments [49, 50]. A metrological improvement

¹There are some subtleties concerning the detection resolution of the work in ref. [38]. However this does not take away from the main thesis of their paper since the 12dB figure of merit was not the integral part of their experimental result.

of 17 dB was attained in a cavity based experiment [51] taking advantage of cycling transitions in ^{87}Rb . However, as it utilizes magnetically sensitive states, and atoms are non-uniformly coupled to the cavity, this approach is not suitable for atomic clocks and other precision sensors requiring the release of the atoms from their trapped locations in the cavity.

Due to systematic errors arising from collisions between atoms, there is typically an upper bound to the number of atoms that can be employed in state-of-the-art cold atom sensors [52–54]. Squeezing offers a universal path to surpassing this limitation in sensitivity. However, methods demonstrated thus far have fallen significantly short of achieving competitive single-shot phase readout sensitivities.

4.1 General Procedure

Here we present a quantum metrology implementation of spin squeezing using the clock states (defined in § 2.1.1) of ^{87}Rb [47, 55]. We prepare the squeezed states through a collective population difference measurement on the atoms. In the spin language, we make a J_z measurement that projects the quantum state into one with a narrower J_z -distribution than that of a CSS. The measurement is enabled by our high-finesse optical cavity: the $|\downarrow\rangle$ ($|\uparrow\rangle$) atoms increase (decrease) the index of refraction seen by the probe light. Therefore, the cavity resonance frequency shift is a direct predictor of J_z [10].

We operate with uniform atom-probe coupling: the atoms are confined by a 1560 nm optical lattice (1D), and probed by 780 nm light (Figure 4.1). This property will enable retrieval of squeezing after releasing the atoms from the optical lattice for cold atom sensors as we will elaborate. In contrast to earlier work [47, 49, 50, 55] we prepare squeezed states without resorting to spin-echo techniques required for non-uniformly coupled systems, and we base squeezing levels on the true CSS-noise level of N atoms (instead of an inferred level using lower effective numbers of atoms).

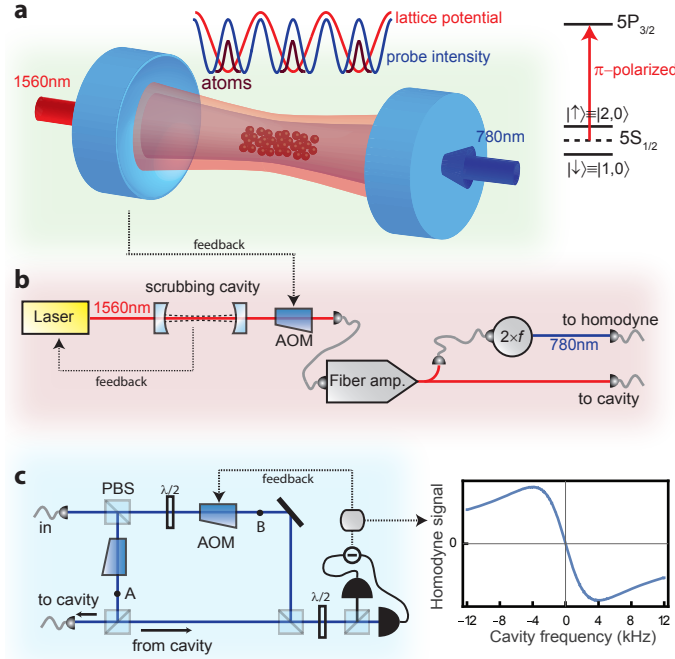


Figure 4.1: a, Uniform atom-probe coupling: atoms are trapped at the maxima of the probe by the 1560 nm lattice. 780 nm probe light is detuned by equal and opposite amounts from the two clock states. b, Probe light is generated by frequency doubling the 1560 nm light that is feedback stabilized to the main cavity. No further stabilization of the probe is required, eliminating residual 780 nm light inside of the cavity. AOM: acousto-optic modulator; PBS: polarizing beam-splitter. c, Homodyne detection system and the form of the output signal. Path ‘A’ contains two path length stabilizing side-bands, in addition to the probe frequency, also present on path ‘B’. See §3.2 for details.

4.2 The Three Pillars

4.2.1 Shot Noise Measurements

We first calibrate our CSS-noise level. We first bring the state to $J_z = 0$ as described in §3.3. Subsequently, we probe the cavity with a $200\mu s$ probe pulse. The incident probe laser power is always increased and decreased adiabatically. The duration of the measurement pulses is $200 \mu s$ – the shortest possible time while avoiding significant ringing in the homodyne signal. Typical incident probe powers are of order 10 pW

(intra-cavity photon numbers: 90 photons/pW on resonance). Since the homodyne signal is time dependent, we apply a time-dependent weighting function in the analysis of the time traces to extract the cavity frequency shift. This method gives the same signal and photon shot noise values irrespective of pulse shapes and duration as long as the pulse area is conserved and the intra-cavity power adiabatically follows the incident power. The dispersive shape of the homodyne signal as a function of cavity resonance frequency can be seen in Figure 4.1C. Quantitatively, given a time-dependent homodyne signal $s(t)$, the cavity shift is $\Delta\nu = D \int dt s(t) \rho(t) / \int dt \rho^2(t)$, where D is the frequency discriminator (Hz/V) at the peak signal level, and $\rho(t)$ is the temporal shape of the signal normalized such that its peak is at 1. $\rho(t)$ and D are determined experimentally in absence of atoms by detuning the probe from the exact cavity resonance by a small amount (well within cavity linewidth), and recording the homodyne signal. For measurements that are still within the cavity linewidth but are not in the linear regime (i.e. closer to $\pm 4\text{kHz}$ in Figure 4.1C), a correction factor is applied. This correction factor is also determined empirically in absence of atoms by detuning the probe from the exact cavity resonance by various amounts ranging from -4kHz to $+4\text{kHz}$, recording the homodyne signal, fitting it to a dispersive curve and comparing it to the signal we would expect from a linear curve given the formula for $\Delta\nu$ above.

The procedure above extracts the correct cavity shift as long as the homodyne signal is in the linear regime. We apply an additional correction factor to properly measure the shifts which are outside this linear regime. This factor is calibrated by setting the cavity-probe detuning to a known value and noting the discrepancy between the known shift and the inferred shift. This is important when establishing CSS noise levels.

We obtain a distribution of cavity shifts revealing the J_z distribution (Figure 4.2). Since we measure a balanced population difference, atom number fluctuations (2% rms) between different runs do not enter at a measurable level. Microwave rotation noise becomes noticeable towards 5×10^5 atoms.

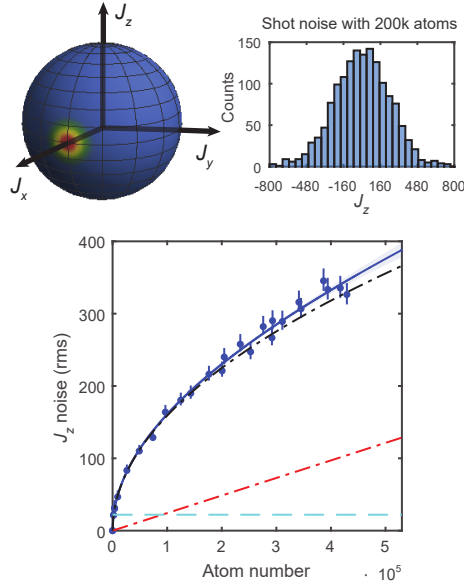


Figure 4.2: Projection noise of unentangled spins. Dot-dashed curve: the expected CSS noise; solid line: fit revealing the underlying microwave rotation noise (dot-dashed straight line); dashed line: resolution of the π -strength measurement (subtracted in quadrature from the data). Error bars: 68% statistical confidence interval.

4.2.2 Reduction in Variance

We show that the J_z -measurements indeed prepare a state with reduced J_z -noise. Irrespective of the noise on the first measurement, a second measurement should be correlated (to within the measurement strength) with the first one. We quantify the measurement strength by the amount of differential phase shift (radians) accumulated on the clock states due to probe-induced ac-Stark shifts. Figure 4.3 shows the noise in the difference between two identical strength back-to-back measurements, as a function of measurement strength (determined by incident probe power) for different atom numbers as well as spin noise reductions at optimal measurement strengths Figure 4.3 (left). The latter saturates with atom number Figure 4.3 (right), albeit slightly earlier than expected, suggesting unknown sources of additional noise. States prepared by the first measurement are input states to any subsequent metrology experiment. Due to the additional uncorrelated noise from the second measurement, these states contain 3 dB more squeezing than directly observed in the measurement difference (see [46]).

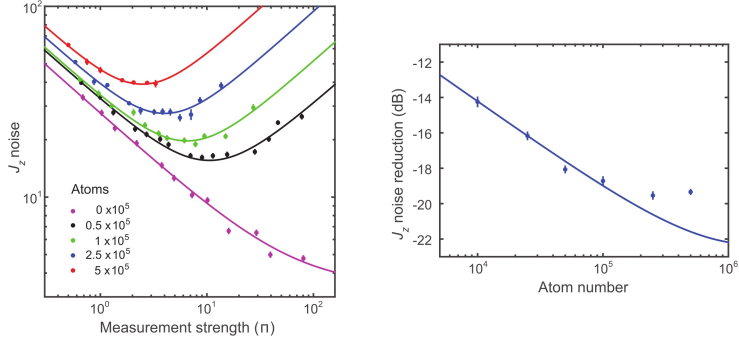


Figure 4.3: (left) Observed spin-noise (rms) for the difference between two equal-strength back-to-back measurements separated by 1.1 ms (half transverse oscillation period). No-atoms data signifies the noise floor. Solid lines: model fits (see Methods). Solid line: Gaussian decay fit. (right) Atom number dependence of maximum observed spin-noise reduction with respect to CSS noise (0 dB is no reduction). Solid line: model fit § 4.8

4.2.3 Coherence

Finally we show that our noise-reduced state also retains most of its coherence Figure 4.4. We do this by measuring Ramsey fringe contrasts after creating the measurement induced squeezed state (i.e. following the first measurement).

4.3 Metrological Enhancement

If we put the spin reduction and coherence results together, we find that the input state with the largest inferred metrological enhancement is at 5×10^5 atoms with a π measurement strength, which gives 20.1(3) dB enhancement capability including the 0.6 dB loss from the measured 93.2% coherence. To demonstrate a metrology example we decrease the first measurement strength to 0.75π while increasing the second one to 2.0π . In this configuration, coherence after the first measurement is 96.2% (with 2×10^{-3} photons/atom free-space scattering), and the second measurement recovers more information. We obtain a directly measured metrological improvement of 18.5(3) dB with respect to the SQL, with which we resolve small rotations around J_y at 6.5×10^5 atoms Figure 4.5. This corresponds to 147 rad (rms) single-shot phase

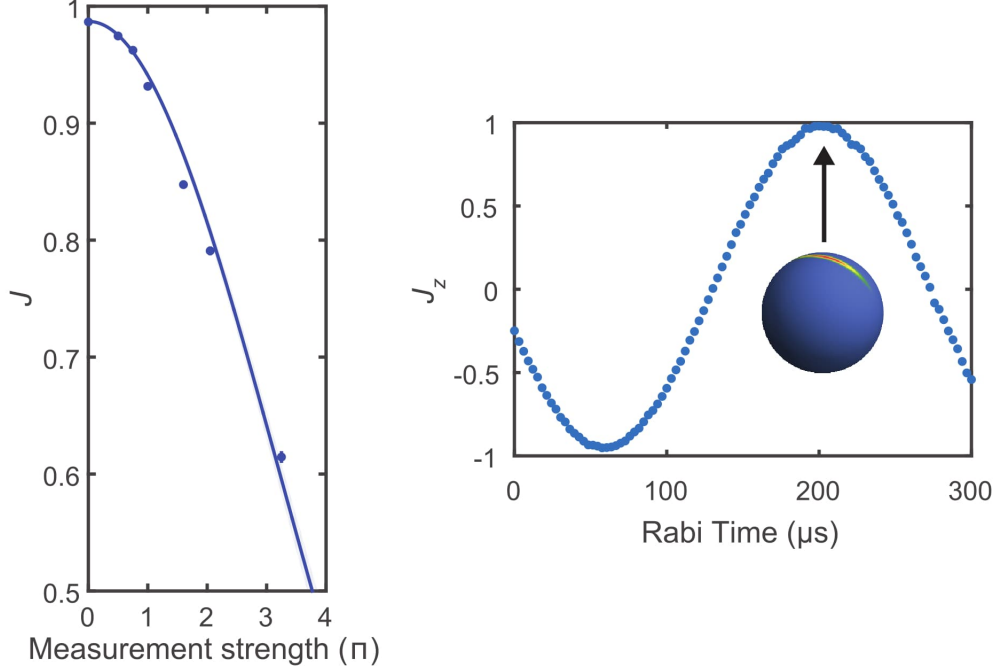


Figure 4.4: (left) Coherence of the state following the first measurement for various measurement strengths. J is the mean length of the Bloch vector (coherence), obtained by measuring Ramsey fringe contrasts following the first measurement. Loss in coherence is due to lattice induced ac-Stark shifts which are partially cancelled by probe ac-Stark shifts. Solid line: Gaussian decay fit. (right) Example of Rabi oscillations executed by the squeezed state, observed with fluorescence imaging. This image shows a 96.2% contrast.

sensitivity.

4.4 Particle Entanglement

I now show that some of the prepared states contain in excess of 680(35) particle entanglement (following [56, 57]). Particle entanglement, or "entanglement depth", is a metric used to determine how much entanglement an ensemble in a mixed state contains. More precisely, a ensemble state with n atoms that has a corresponding density operator ρ which can be composed as a convex sum of density matrices $\rho_1 \otimes \rho_2 \otimes \dots \otimes \rho_m$, has an entanglement depth of k if each ρ_i corresponds to a density

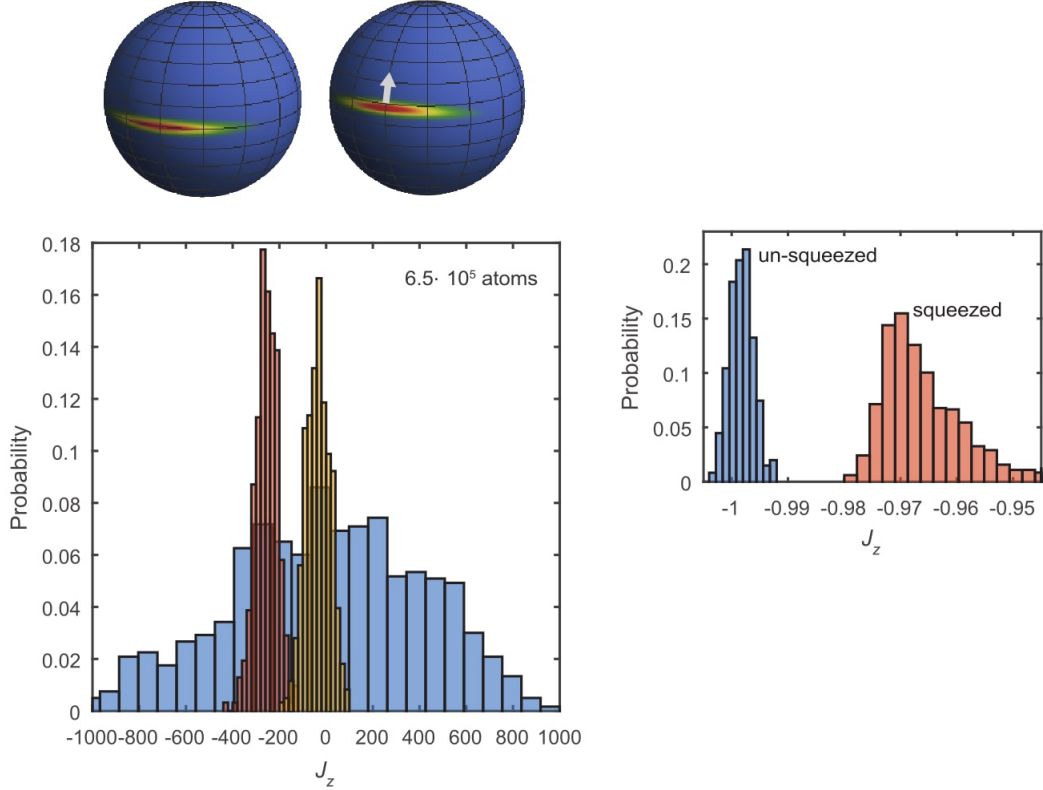


Figure 4.5: (left) Two squeezed states, one rotated by a weak microwave pulse by $660 \mu\text{rad}$. The two distributions are overlaid on the un-squeezed distribution (measurements strengths: 0.75π - 2.0π). (right) Histogram is the distribution of J_z at the indicated point in Figure 4.4. The distribution width of the un-squeezed case, shown for reference, is limited by camera read-out noise.

matrix containing at most k atoms and $m \leq n$ [58, 59]. For example, if ρ can be decomposed into a tensor product of ρ_i 's describing Bell pairs (i.e. each ρ_i represents 2 particles maximally entangled with each other) then ρ would have an entanglement depth of 2. A more in depth explanation of entanglement depth boundaries can be found in § 6.7. Measurements of the collective spin operators $J_i = \sum_{n=1}^N j_i^n$ for an ensemble of N two-level atoms can be used to quantify the amount of entanglement in the ensemble [56, 57] without further reference to the specific nature of the states. We will follow the analysis of ref. [57], where the variance and the mean-square Bloch vector length places the measured states on a plane with boundaries corresponding to

different entanglement depths.

In our experiment, due to the residual inhomogeneities in atom-cavity coupling, we measure the collective observable $J'_z = \frac{1}{Z} \sum_{n=1}^N (1 - \varepsilon_n) j_z^{(n)}$, where Z is a normalization constant and ε_n is the small fractional deviation in coupling for atom n (see §4.9). This implies that we cannot directly utilize the measured spin noise values for the purposes of calculating entanglement depths. However, even without a direct measurement of J_z itself, its maximum possible variance can be inferred as is argued in section §4.10. There, we found that there would be an additive noise of 17 dB below CSS noise if we tried to read-out the prepared states via fluorescence imaging, which we consider to be a true J_z measurement. Therefore, we infer J_z based on this analysis. Unlike the cavity based measurements, the Bloch vector length measurements, which are done via fluorescence imaging can directly be utilized for calculating entanglement depths.

In Figure 4.6 we plot the inferred variances for the 5×10^5 atom dataset using the experimentally established noise after the first measurement ($1/\sqrt{2}$ of the values in Figure 4.3). The point with the largest metrological gain (π measurement strength) gives an entanglement depth of 330(15) atoms, while the largest entanglement depth is 680(35) (0.5 π meas. strength) atoms. This exemplifies that entanglement depth is in itself not a direct predictor for metrological improvement.

The additional noise in our model in inferring J_z originates from shot-to-shot randomization of atomic positions. In the absence of this randomization, we expect the discrepancy between the variances of J'_z and J_z to be less. Thus, the quoted entanglement depths should be taken as lower bounds. For reference, had we not taken into account the coupling inhomogeneity we would have found the largest entanglement depth to be 1605(30) atoms.

4.5 Pre-Squeezing

When using high atom numbers when making the squeezing and coherence measurements in §4.2, CSS noise exceeds the linear region of the homodyne signal because the rms cavity shifts due to shot CSS noise approach the linewidth of the cavity. This quantum noise prevents us from preparing initial J_z distributions that fall purely

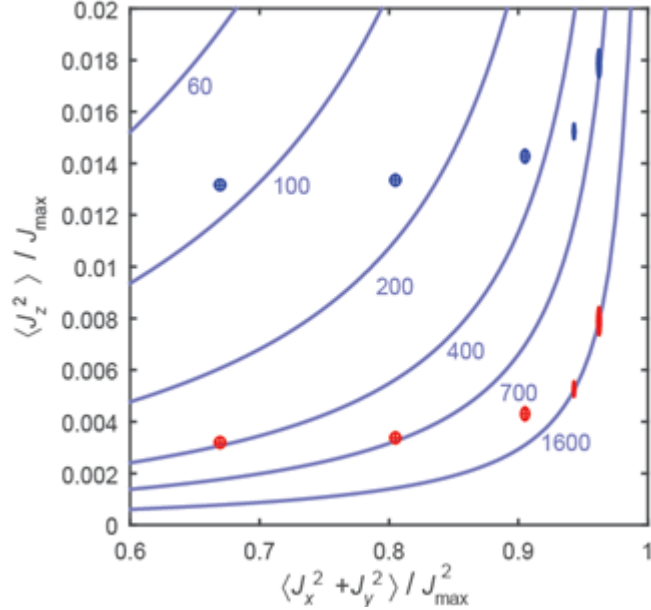


Figure 4.6: The inferred spin noise variance (y-axis) and the mean-square Bloch vector lengths (x-axis) are plotted for the 5×10^5 atom data set. Note that the probe power decreases from left to right. The x-axis values are conservatively chosen to be the most probable value of the measured Bloch vector length distributions (Figure 4.5. A state below an M-particle boundary is guaranteed to contain at least groups of M-particles whose quantum states are non-separable. The blue data set establishes a lower bound on entanglement depth taking into account the residual inhomogeneity in atom-cavity coupling. The red data set, for reference, shows what we would have obtained had we ignored the small inhomogeneity. The ellipses correspond to the 68% statistical confidence intervals on the quoted values. $J_{max} = N/2$. The third data point in each set shows the largest metrological improvement.

within the linear region of the homodyne signal using microwave rotations alone. Outside the linear region, both the measurement efficiency and the intra-cavity probe power decrease; the former degrades achievable squeezing; the latter results in varying ac-Stark shifts. We therefore resort to atom-cavity nonlinearities to deterministically pre-squeeze the state by a sufficient amount such that the distribution fits within the linear regime. The nonlinearity employed is a J_z^2 -interaction causing one-axis twisting similar to the one used in ref. [47], the procedure maps unsqueezed states from an area on the equator near the J_x -axis onto squeezed states to an area on the opposite side of the J_x -axis. The technical noise on the initial J_z preparation is also

suppressed. The pre-squeezing occurs after the composite $\pi/2$ -pulse brings the state to the equator. We send 100 nW of light at $6.25\kappa_0$ detuning from the bare cavity resonance (generating J_z^2 -interaction) and simultaneously turn on a $400\mu\text{s}$ microwave $\pi/12$ -pulse (generating rotations around Jx-axis). With the combined action, we observe up to 7 dB unconditional J_z squeezing while retaining 99% coherence.

The pre-squeezing procedure is a supplement to the J_z measurement protocol, increasing robustness and efficiency. However we note that it does not alter the nature of J_z measurements – we obtain the same final squeezing results in absence of pre-squeezing if we post-select the runs with the first measurement outcome lying within the linear regime of the homodyne signal.

4.6 Clock measurements

The following are the results of a clock measurement that compare the atomic and microwave phases to better than that allowed by CSS noise. Following J_z -squeezing, we apply a $\pi/2$ -pulse ($74\ \mu\text{s}$) to rotate the noise-ellipse into a phase-sensitive state, then wait for phase accumulation, and finally map this phase onto J_z with another rotation. High frequency microwave phase noise during the measurement interrogation period results in excess noise proportional to the atom number. To obtain the maximum quantum enhancement, we lower the atom numbers to 1×10^5 and observe up to 10.5(3) dB metrological gain in phase comparison. To put these measurements in context with clock performance, we operate with the largest Ramsey time ($\sim 228\mu\text{s}$ phase accumulation) which does not measurably degrade the comparison. We achieve 9.7×10^{-11} fractional stability at 1s averaging time. For the fixed Ramsey time, the squeezed clock reaches a given precision 11.2(8) times faster than possible without squeezing. The state evolution and results of this clock measurement can be seen in Figure 4.7. The local oscillator noise entering through the Dick effect can be circumvented using interleaved clocks [60], in which case the full advantage of squeezing can be achieved using adaptive measurements [61]. To take full advantage of the achieved sensitivity for implementing an atomic clock, we need to reduce the phase noise of our microwave local oscillator.

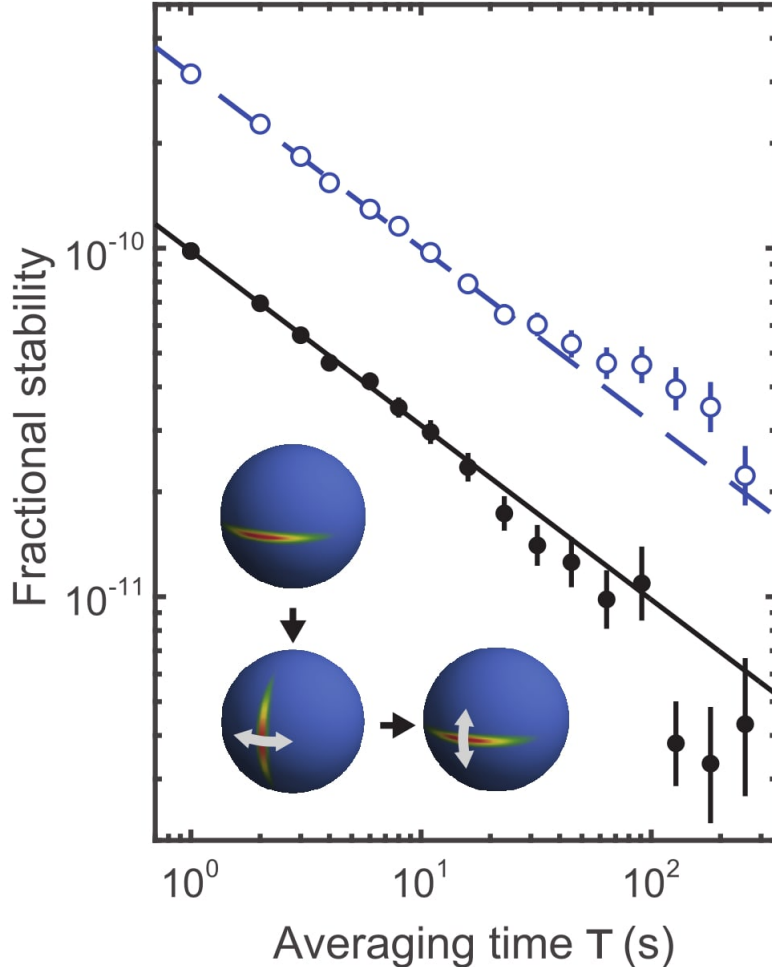


Figure 4.7: Allan deviation of a squeezed atomic clock for $228\ \mu\text{s}$ interrogation time at 1 Hz repetition rate (filled circles). The state is rotated into phase-sensitive orientation during the interrogation time. Dashed line: theoretical CSS-noise limit; open circles: measured spin CSS-noise level for the same Ramsey time. Solid line: $9.7 \times 10^{-11} s^{1/2}/\sqrt{\tau}$. The Bloch spheres illustrate the clock sequence with squeezed states; white arrows depict conversion of phase jitter into population jitter.

4.7 Anti-Squeezing

The cavity measurements, while projecting the atomic ensemble onto a state with reduced J_z noise, also act back onto the conjugate observable J_y and increase its noise. In the ideal case a measurement would preserve the area of the uncertainty

ellipse, that is, the reduction and the increase in the noises of J_z and J_y respectively would be through the same factor. However due to photon losses, inefficiencies in extracting the information in the read-out, and the additional spin-flip noise in J_z , the balance is expected to be broken. Experimentally, the variance of J_y scales linearly with measurement strength, reaching 39 dB above CSS noise at measurement strength accompanying the quoted 20.1(3) dB squeezing in J_z . This corresponds to a factor of 8.8 increase in the uncertainty ellipse area. The observed level of anti-squeezing is within 2 dB of the expectations.

4.8 Squeezing limitations

The J_z measurement resolution is determined by the competition between photon shot noise and probe induced Raman scattering (spin-flips). The former limits the precision of the cavity frequency measurements; the latter leads to a random walk in the measured observable and is elaborated in on § 2.4. We will specify these quantities as functions of the (experimentally accessible) differential phase shift $\phi_{AC} = \frac{2g^2}{\Delta} \int dt n_c(t)$ accumulated on the clock states. Here, $n_c(t)$ is the intra-cavity photon number.

The number of scattered photons is $m_s = \phi_{AC}(\Gamma/\omega_{HF})$. The hyperfine splitting enters because the atom-cavity detuning is set to $\Delta = \omega_{HF}/2$. Using the branching ratios for ^{87}Rb , it can be shown that only 1/6 of the scattering events will give rise to a spin-flip, i.e., a change of the hyperfine state. These spin-flips will give rise to a random walk on J_z with a variance of $\delta_{flip}^2 = \frac{N}{6} \frac{\Gamma}{\omega_{HF}} \phi_{AC}$. This is the spin-flip noise; it grows with atom number and probe power.

To examine the measurement noise, we analyze the information imprinted on the light transmitted from the cavity. Around zero cavity-probe detuning, the number of photons transmitted through the cavity is $n_T = \frac{\varepsilon_C(\omega_{HF}/\Gamma)}{2C} \phi_{AC}$, where $\varepsilon = 2\kappa_M/\kappa_0$ is the cavity efficiency incorporating the optical losses. As the atoms shift the cavity frequency by $\frac{2g^2}{\Delta} J_z$, the phase shift on the light upon transmission is $\phi = \frac{2C(\Gamma/\omega_{HF})}{1+NC(\Gamma/\omega_{HF})^2} J_z$. Given the quantum phase noise $\frac{1}{2\sqrt{n_T}}$ for a coherent state, the noise equivalent J_z resolution is $\frac{1+NC(\Gamma/\omega_{HF})^2}{\sqrt{8\varepsilon_C C(\Gamma/\omega_{HF})}} \frac{1}{\sqrt{\phi_{AC}}}$. For a symmetric cavity, equal amounts of information leak out from each mirror. Thus, including the information gained from the reflection would

improve the resolution by $\sqrt{2}$. Lastly, we also include the effect of photon losses on the way to the detectors, and bundle all efficiency factors into the quantity ε which is further discussed in the ‘Atom/cavity parameters’ section above. The final expression for the measurement noise is $\delta_{meas}^2 = \frac{(1+NC(\Gamma/\omega_{HF})^2)^2}{16\varepsilon C(\Gamma/\omega_{HF})} \frac{1}{\phi_{AC}}$; it decreases with increasing probe power.

As a first approximation the total noise in the estimation of J_z can be found by adding the contribution due to the two sources: $\delta^2 = \delta_{meas}^2 + \delta_{flip}^2$. An optimal ϕ_{AC} (i.e., measurement strength) minimizes this expression, at which point $\delta^2 = \frac{\sqrt{N(1+NC(\Gamma/\omega_{HF})^2)}}{\sqrt{24\varepsilon C}}$. Assuming negligible coherence loss, as is the case experimentally, we arrive at an optimal metrological enhancement $\chi_{opt}^2 = \frac{\sqrt{\varepsilon NC^3/2}}{1+NC(\Gamma/\omega_{HF})^2}$. At first, the achievable enhancement increases with atom number, attaining a maximum of $(\omega_{HF}\sqrt{3\varepsilon/8})$ at $N_{opt} = \omega_{HF}^2/\Gamma^2C$. This saturation effect can be traced back to cavity linewidth broadening from atomic absorption § 4.8.1. For $\varepsilon = 1$, the maximum achievable enhancement is around 28 dB.

Exact numerical agreement should not be expected between the naive model presented here and the experiment, since the latter is more complicated. We use the functional forms derived here to fit to the data in Figure 4.3. In particular for part ‘a’ we use $\delta^2 = \frac{\alpha}{\phi_{AC}} + \beta\phi_{AC}$ and for part ‘b’ we use $\chi_{opt}^2 = \gamma \frac{\sqrt{\varepsilon NC^3/2}}{1+NC(\Gamma/\omega_{HF})^2}$. Here, α , β and γ are the fit parameters.

The enhancement saturates with atom number due the impact of atomic absorption on measurement sensitivity, in addition to the spin-flips. For our parameters ($\varepsilon = 0.16$), the upper bound on achievable squeezing is about 24 dB.

4.8.1 Cavity broadening due to atom absorptions

At large atom numbers the cavity linewidth broadens due to atomic scattering, causing the squeezing saturation. The atom number dependent linewidth is $\kappa = \kappa_0 + \kappa_S$, with κ_S being the additional scattering contribution. The fractional change is $\kappa_S/\kappa_0 = NC(\Gamma/\omega_{HF})^2$. We incorporate this signal degrading effect into the cavity shift analysis. The change in the overall signal shape due to broadening is negligible for our parameter range. We experimentally verify that we indeed obtain $\kappa_S/\kappa_0 \approx 0.30$ at 5×10^5 atoms.

To do this, we jump the cavity frequency by a known amount (smaller than κ) between consecutive measurements and observe the signal reduction in comparison to the empty cavity case. More specifically, we first probe the empty cavity with the probe being -4kHz off resonance and look at the bottom of the dispersive signal. This gives us a baseline for $\kappa(N = 0) = 8kHz$ which we will call $S(0)$. We then repeat this measurement with the $N = 5 \times 10^5$ atoms in the cavity which gives us $S(N)$. The trick was to keep the signal on for a long time (i.e. $\sim 1ms$) so that even though at early times (up to 0.5ms), the signal is all over the place, it eventually bottoms out due to depumping (so there's an effective scanning of the cavity because of the atoms getting depumped). So we can measure the bottom of the dispersive signal with the atoms in the cavity. Using this signal we can calculate κ_s with the following:

$$\kappa(N) = \kappa_0 + \kappa_s(N)$$

where $\kappa_s(N)$ is the scattering due to the atoms. The homodyne dispersive signal is proportional to [10]

$$\frac{\kappa_0}{\kappa(N)} \frac{\frac{\delta}{\kappa/2}}{1 + \frac{\delta}{\kappa/2}^2}$$

where δ is the detuning of the probe to the empty cavity resonance frequency. If we sit at $\delta = \frac{\kappa}{2}$ (i.e. the maximum), then we get

$$S(N) = \frac{\kappa_0}{2\kappa}$$

And so we can use this to get $\kappa_s(N)$ with the equation

$$\begin{aligned} \frac{S(0)}{S(N)} &= \frac{\kappa(N)}{\kappa_0} \\ &= 1 + \frac{\kappa_s(N)}{\kappa_0} \end{aligned}$$

We then compare the signal size which is reduced due to the kappa broadening. We found a kappa increased by about 27%. So $\kappa = \kappa_0 + \kappa_s = 1.27 \times \kappa_0 \rightarrow \kappa_s = 0.27 \times \kappa_0$.

This approximately agrees with our calculated value of 0.30. This value is obtained by starting with

$$\kappa_S(N) = N_\uparrow \times \frac{g^2}{\Delta} \frac{\Gamma}{\Delta} + N_\downarrow \times \frac{g^2}{\Delta} \frac{\Gamma}{\Delta}$$

where $N_{\uparrow(\downarrow)}$ are the number of atoms in the $|\uparrow\rangle$ ($|\downarrow\rangle$) state, g is the atom-cavity coupling constant, Δ is the detuning of the probe from the $|\uparrow\rangle \rightarrow |e\rangle$ transition and Γ is the lifetime of the excited state. Taking $N_\uparrow \sim N_\downarrow = N/2$ and putting in the numbers $N=500 \times 10^3$, $g^2/\Delta = 2.75 Hz$, $\Gamma = 6 MHz$ and $\Delta = 3.4 GHz$ we obtain $\kappa_S(N = 500000)/\kappa_0 = 0.30$.

4.9 Coupling inhomogeneity

We would like to measure the collective observable $J_z = \sum_{n=1}^{N_0} j_z^{(n)}$, with N_0 the total number of atoms, and $j_z^{(n)} = \frac{1}{2}\sigma_z^{(n)}$ the z-component of the spin operator for atom n. However, due to the residual inhomogeneity in the atom-cavity coupling we measure a slightly different collective observable J'_z that is a weighted sum over $j_z^{(n)}$. If all atoms coupled identically to the cavity with the per-spin-flip cavity frequency shift for atom n given by $\delta^{(n)} = \delta_0$, the total shift would be $\Delta_0 = \sum_n \delta_0 j_z^{(n)} = \delta_0 J_z$. However, due to the small fractional deviations ε_n in the coupling constants for the atoms n, the total shift is given by

$$\begin{aligned} \Delta &= \sum_n \delta^{(n)} j_z^{(n)} \\ &= \sum_n \delta_0 (1 - \varepsilon_n) j_z^{(n)} \\ &= (\delta_0 Z) \left(\frac{1}{Z} \sum_n (1 - \varepsilon_n) j_z^{(n)} \right) \equiv \delta_{eff} J'_z \end{aligned} \quad (4.1)$$

Here Z is a normalization constant, and $\delta_{eff} = \delta_0 Z$ is the effective cavity shift per spin flip. To decide on a normalization, we utilize two properties of J'_z : its maximum $(J'_z)_{max} = \frac{N_0}{2} \frac{1}{Z} \langle 1 - \varepsilon \rangle_e$ and its projection noise with uncorrelated atoms

$\text{var}(J'_z)_{\text{proj}} = \frac{N_0}{4} \frac{1}{Z^2} \langle (1 - \varepsilon)^2 \rangle_e$. Here $\langle \cdot \rangle_e$ indicates an ensemble average. We choose Z such that the statistical condition $\frac{\text{var}(J_z)}{\langle J_z \rangle_{\text{max}}} = \frac{N_0/4}{N_0/2} = \frac{1}{2}$ satisfied by J_z is also be satisfied by J'_z . This leads to $Z = \frac{\langle (1 - \varepsilon)^2 \rangle_e}{\langle 1 - \varepsilon \rangle_e}$, and thus:

$$J'_z = \frac{\langle 1 - \varepsilon \rangle_e}{\langle (1 - \varepsilon)^2 \rangle_e} \sum_n (1 - \varepsilon_n) j_z^{(n)} \quad (4.2)$$

Consequently, one can think of the non-uniformly coupled system of N_0 atoms as a uniformly coupled system of $N \equiv N_{\text{eff}} = N_0 \frac{\langle 1 - \varepsilon \rangle_e^2}{\langle (1 - \varepsilon)^2 \rangle_e} = 0.995 N_0$ effective atoms in conjunction with an effective cavity shift $\delta_{\text{eff}} = \delta_0 \frac{\langle (1 - \varepsilon)^2 \rangle_e}{\langle 1 - \varepsilon \rangle_e}$ per spin-flip. Here δ_0 is the cavity shift for an atom on cavity axis averaged over the distribution along the tightly trapped longitudinal direction. This gives $\delta_{\text{eff}} = 0.83 \delta_{\text{max}} = 5.5 \text{ Hz}$, where δ_{max} is the cavity shift for an atom localized at a peak of the probe mode profile.

4.10 Maintaining squeezing after the release of atoms into free space

The squeezed states prepared in this work can be released from the confining lattice for precision sensing applications. To infer the retrievable squeezing in a configuration where the second cavity measurement is replaced with fluorescence imaging in free space, we analyze the noise modulations observed in back-to-back cavity measurements (Figure 4.8) as a function of delay time between the measurements. These modulations are evidently due to residual atom-probe coupling inhomogeneities, and based on our model, we can in theory retrieving up to 14.6 dB squeezing.

Although we have uniform atom-cavity coupling, we still have residual inhomogeneities due to thermal motion. Figure 4.8 shows the noise between back-to-back measurements for varying measurement separations: noise is smallest when the separation is half-integer multiples of the 2.2 ms transverse-oscillation period. We model this behavior to make an estimate of retrievable squeezing with fluorescence imaging.

The observed effect can be explained with the statistical fluctuations in atomic

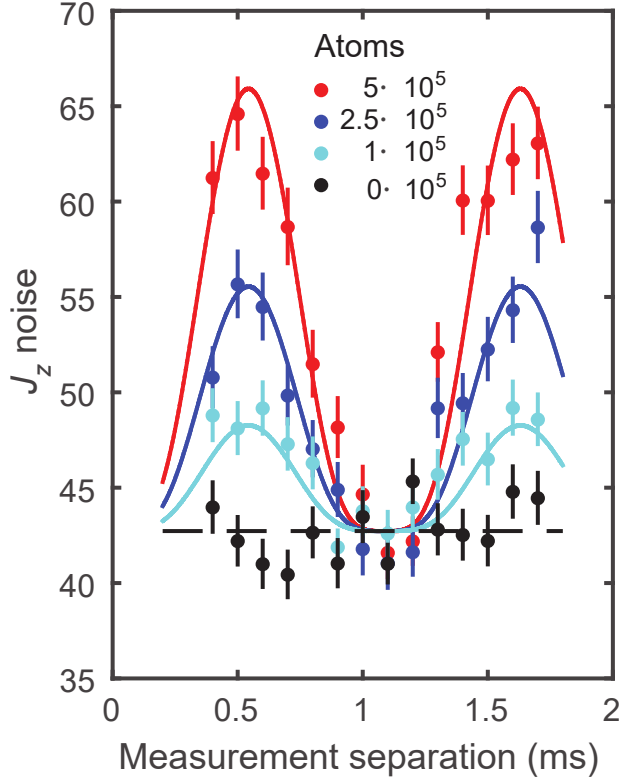


Figure 4.8: Back-to-back measurement noise as a function of measurement separation time. No matching pattern in mean J_z -difference between the measurements is observed; only the noise is modulated. Measurement strengths are chosen to make the noise minima equal for different atom numbers. Solid lines are predictions with no free parameters.

positions from one experimental cycle to the next. A classical trajectory analysis on the atoms in a harmonic trap (transverse motion) suffices to predict the noise in two consecutive cavity measurements as a function of measurement separation time. Given their initial phase space points during the first measurement, the location of the atoms during the second measurement, and hence the cavity frequency difference can be deterministically predicted. However, each time the experiment is repeated, the atoms will start at a different configuration in phase space giving rise to a slightly different cavity frequency difference. We calculate this additional noise assuming a thermal distribution for the atoms. The resulting prediction is $\langle J_z^2 \rangle^{1/2} = \sqrt{N}(1 - \alpha^2) \left(\frac{1}{1+2\alpha^2} + \frac{1}{1+2\alpha^2+\alpha^4(1-\cos^4 \omega t)} - \frac{2}{1+2\alpha^2+\alpha^4 \sin^2 \omega t} \right)^{1/2}$, where ω is the transverse

oscillation angular frequency and $\alpha = 2\sigma_r/w_{780}$ with σ_r the transverse size of the atomic cloud and w_{780} the probe beam waist ($\alpha^2 = 0.076$). The solid lines in Figure 4.8 are the addition of this function in quadrature with the baseline without any free parameters.

A similar analysis could be used to predict the additional noise that will arise when the first measurement is done using the cavity and the second one using fluorescence imaging. The second measurement is insensitive to atomic positions; hence the noise comes only from the statistical fluctuations in atomic positions during the first measurement. The estimate for the additional noise is $\langle \Delta J_z^2 \rangle^{1/2} = \sqrt{N}\alpha^2/\sqrt{1+2\alpha^2}$, which is 17 dB below CSS noise for our experiment. In particular an 18.5 dB squeezed state would read 14.6 dB with fluorescence imaging.

Preliminary results for demonstrating that the squeezing was still retrievable after releasing the atoms into free space are shown in Figure 4.9 and Figure 4.10. The procedure for demonstrating this was the same as the procedure for showing squeezing while maintaining the atoms in the lattice (see § 4.2) with the extra step of turning off and on the lattice in between the two squeezing measurements. It is important to note that when we turn on and off the lattice, the cloud expands in size, and so when the second measurement is done, the atom-cavity coupling changes and the cavity shift per change in J_z is reduced and this change in coupling had to be measured. The results of the change in coupling can be seen in Figure 4.11.

As seen in the Figure 4.9, we manage to maintain squeezing even when the atoms are released into free space for over 1ms. In addition, Figure 4.10 shows that the coherence of the states do not decrease with release time and remain at about 95%. This is expected, since our main source of decoherence is from the ac-stark shift of the 1560nm lattice, which is turned off during the release time. This shows promising results which will be investigated and further improved upon in the next few months.

In addition, the next step is to try and measure squeezing directly using a camera. Below are some calculations about the setup we would need in order to achieve this objective.

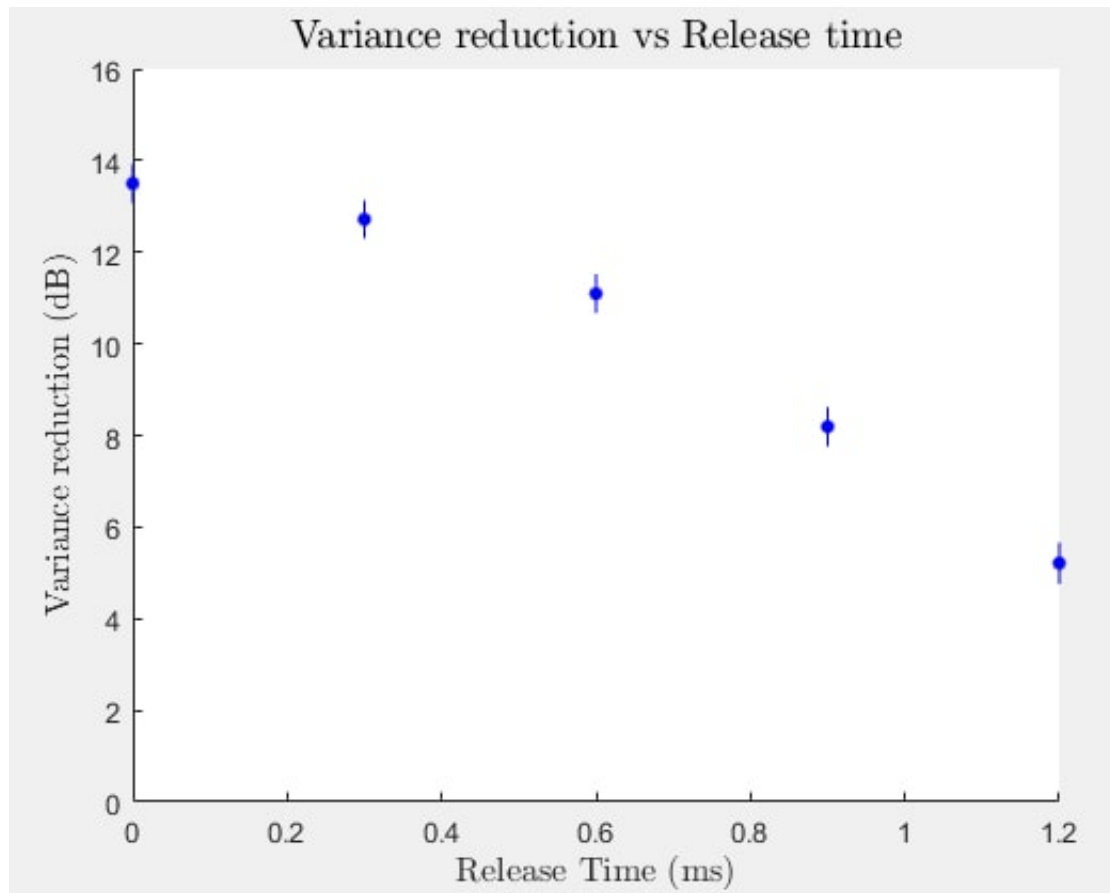


Figure 4.9: Observed spin-noise (rms) for the difference between two equal-strength back-to-back measurements as a function of release time.

4.10.1 Photons needed to image atoms with fluorescence below shot noise

Here I calculate the amount of photons required to be collected by the camera if we want our fluorescence measurement to have a resolution below the shot noise.

$$\frac{\text{Photon noise}}{\text{Photon signal}} = \frac{\text{Atom number noise}}{\text{Atom number signal}}$$

$$\sqrt{n \times N}(n \times N) = \frac{\frac{1}{\beta} \frac{\sqrt{N}}{2}}{N} \quad (4.3)$$

where N is total number of atoms, n is photon per atom detected and β is the

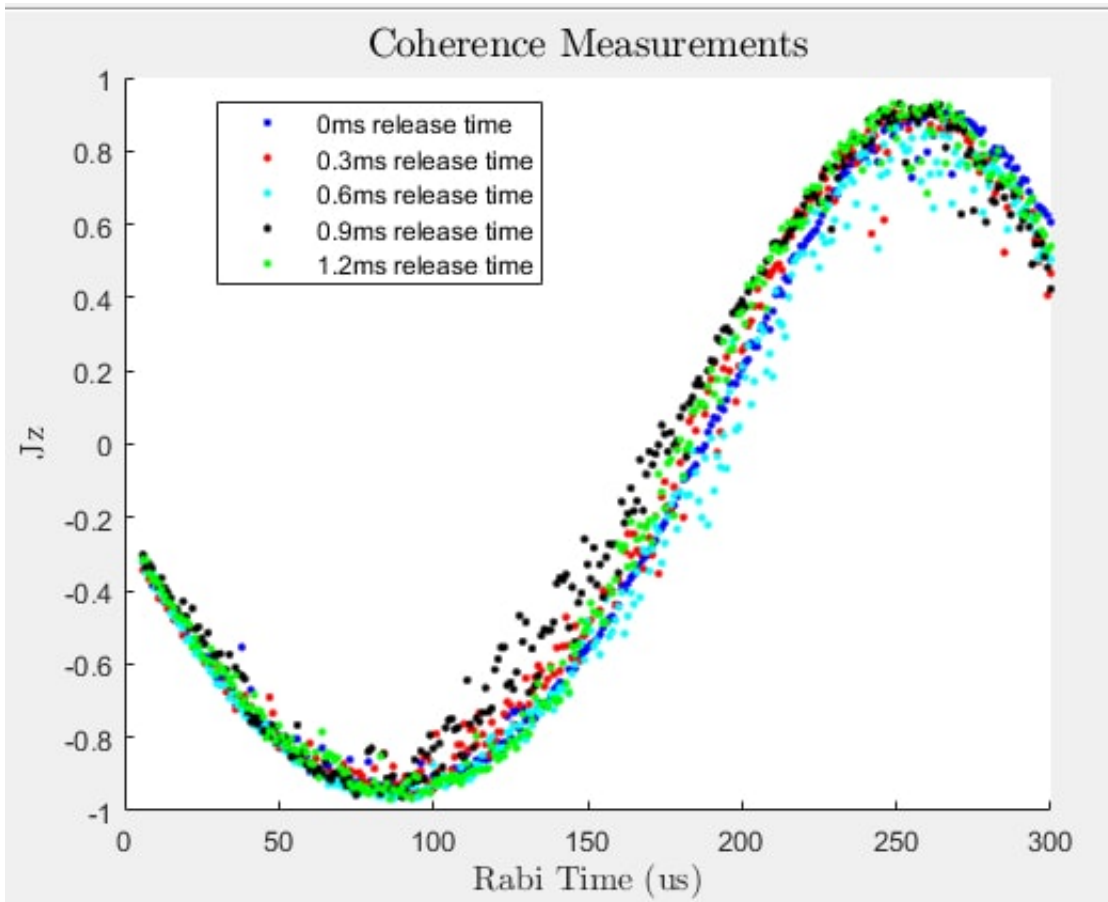


Figure 4.10: (left) Coherence of the state following the first measurement for various measurement strengths. J is the mean length of the Bloch vector (coherence), obtained by measuring Ramsey fringe contrasts following the first measurement. Loss in coherence is due to lattice induced ac-Stark shifts which are partially canceled by probe ac-Stark shifts. The different colors represent different release times.

amount below shot noise you want your atom noise to be (e.g. 10 for 20dB squeezing). Rearranging Equation 4.3 and taking shot noise to be $\sqrt{N}2$ gives us $n = 4\beta^2$. The same result can be obtained using the following equation

$$\begin{aligned}\text{Inferred atom number} &= \frac{\text{photon signal + photon noise}}{\text{photons per atom}} \\ &= \frac{N \times n + \sqrt{N \times n}}{n}\end{aligned}$$

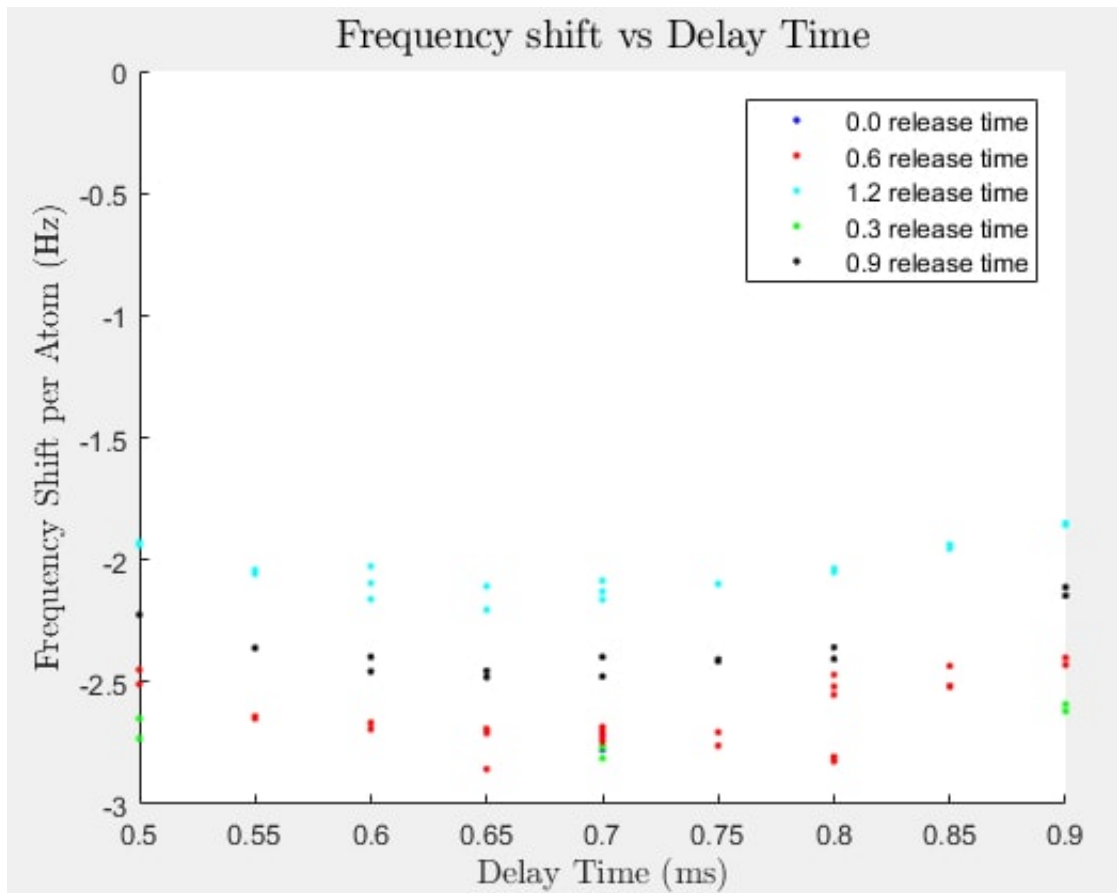


Figure 4.11: Observed atom-cavity coupling as a function of wait time after being recaptured. The data was taken by preparing a state where a known number of atoms were all in the $| \downarrow \rangle$ state (i.e. $J_z = -N/2$ where N is the total number of atoms) and looking at change in cavity resonance. The different colors represent different release times and for each release time and wait time, several results were taken with varying atom numbers.

and require that the noise term ($\sqrt{N \times n}$) be equal to some factor of atom shot noise (i.e. $\frac{1}{\beta} \frac{\sqrt{N}}{2}$)

Chapter 5

Quantum phase magnification

In the following chapter I will discuss the work we did establishing and demonstrating the quantum phase magnification protocol which was published in 2016 [8].

The prospect of using quantum entanglement to improve the precision of atomic and optical sensors has been a topic of discussion for more than two decades. Exemplary work using atomic ensembles include preparation of spin-squeezed states [7, 41–47, 49–51, 62] Dicke states [57, 58, 63] and other states with negative Wigner functions [64]. An assumption common to all this work is that low-noise detection methods are required to properly measure and utilize the prepared quantum states. In fact, detection noise has thus far been the bottleneck in the performance of these systems. To this end, there has been dedicated work on improving state-selective detection of atoms with both optical cavity aided measurements [65, 66] and fluorescence imaging [67, 68]. Here we describe the concept and the implementation of a quantum phase magnification technique that relaxes stringent requirements in detection sensitivity for quantum metrology. This method is a generalization of a recent proposal for approaching the Heisenberg limit in measurement sensitivity without single-particle detection [69]. We demonstrate the method in an ensemble of ^{87}Rb atoms. As in a typical atomic sensor or clock, the goal is to measure a differential phase shift accumulated between a pair of quantum states during a time interval. To make this measurement, the phase shift is first converted into a population difference [7, 48], and then the population difference is measured. Our scheme magnifies this population

difference before the final detection, in effect magnifying the initial phase shift. The atomic ensemble is first spin-squeezed using atomic interactions aided by an optical cavity, and then small rotations – to be sensed – are induced on the atomic state. These rotations are magnified by stretching the rotated states Figure 5.1A, using cavity-aided interactions, and are finally detected via fluorescence imaging. Magnification allows for substantial reduction in the noise requirements for the final detection. While the method is demonstrated in an atom/cavity system, it is broadly applicable to any quantum system which has a suitable nonlinear interaction (see § 5.8).

5.1 General Procedure

The magnification procedure (Figure 5.1A) starts with a mapping of J_z onto J_y (Figure 5.1B) via a shearing interaction. A rotation of J_y into z follows to complete the sequence. The interaction leading to the mapping (shearing) generates a rotation of the state about the J_z -axis with the rotation rate depending on J_z , and is represented by the one-axis twisting Hamiltonian [6] $H = \hbar\chi J_z^2$, where χ is the shearing strength.

The Heisenberg equations of motion for the vector operator \mathbf{J} yields $\dot{\mathbf{J}} = \frac{1}{2}(\boldsymbol{\Omega} \times \mathbf{J} - \mathbf{J} \times \boldsymbol{\Omega})$, where the rotation vector $\boldsymbol{\Omega} = \hat{\mathbf{z}}2\chi J_z$ is also an operator. We will assume that the angular shifts we seek to measure are small (otherwise, they would readily be measurable without magnification), and that the uncertainties of the states after magnification occupy a small fraction of the Bloch sphere. With these assumptions and working with near-maximal initial x-polarization $J_x \approx J = N/2$, we can linearize the problem and focus our attention to a planar patch of the spherical phase space (Figure 5.1B-D). The equations of motion then yield $J_z(t) = J_z(0)$ and $J_y(t) = J_y(0) + MJ_z(0)$ with $M = N \int_0^t dt' \chi(t')$. Thus the initial J_z is mapped onto J_y with a magnification factor M. This is analogous to free expansion of a gas if one identifies J_z with a particle's momentum and J_y with its position.

We implement the one-axis twisting Hamiltonian through a dispersive interaction between atoms and light in an optical cavity [47]. The underlying mechanism is a coupling between the intra-cavity power and atomic populations. The atom-cavity detuning is set such that the shift in the cavity resonance due to the atoms is

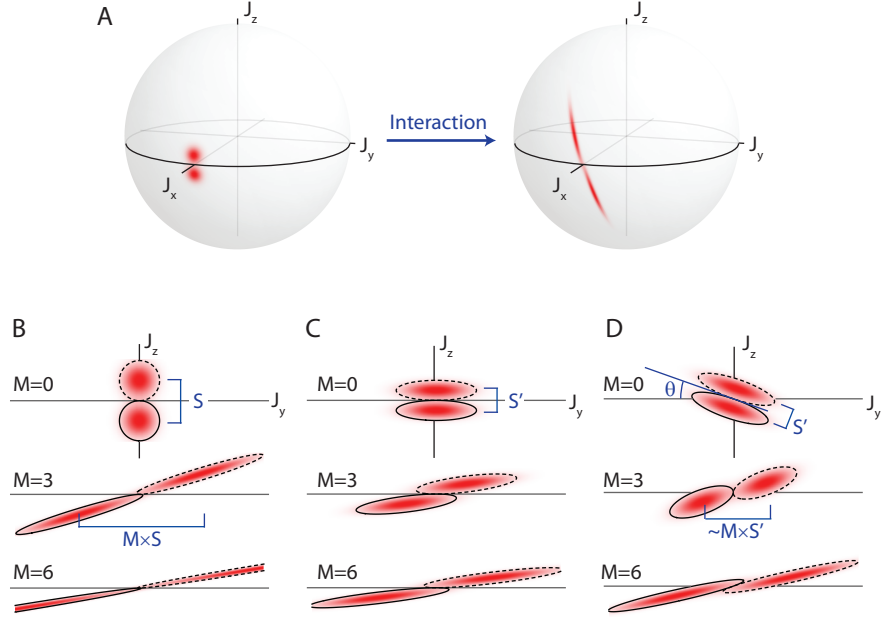


Figure 5.1: (A) Illustration of the magnification protocol on the Bloch sphere. The Wigner quasi-probability distributions are shown for two separated initial CSSs (left), and after the states are magnified through collective interactions (right). Here this is shown with $N = 900$ atoms and a magnification of $M = 3$ for pictorial clarity. Experimentally we use up to $N = 5 \times 10^5$ and $M = 100$, permitting us to concentrate on a planar patch of the Bloch sphere. (B-C) Effect of the J_z^2 (shearing) interaction used for mapping J_z onto J_y for a pair of different initial states with separations S and $S' = S/2$; each panel shows three different magnification factors. Note that a $\pi/2$ rotation about the J_x -axis needs to follow to complete the protocol. (B) shows CSSs and (C) shows 6 dB squeezed states, together illustrating the requirement of larger magnifications to separate two initially squeezed states. (D) A small rotation θ about the J_x -axis is added before the shearing step, eliminating the requirement of larger magnifications for squeezed states by giving rise to a re-focusing of the J_y noise. At an optimal magnification (here $M = 3$), the noise re-focusing scheme maps the initial J_z onto J_y preserving the SNR associated with the two initial states.

proportional to J_z . The frequency is labeled as ω_p in Figure 2.3. Thus J_z sets the cavity-light detuning, which in turn sets the intra-cavity power §5.4. Figure 5.2, which in turn provides a J_z -dependent ac-Stark shift – hence the J_z^2 interaction. Implemented this way, there is also a J_z -independent part of the ac-Stark shift, causing global

rotations of the state about the J_z -axis even for $J_z = 0$. The rotation angle due to this effect is proportional to the pulse area of the interaction light incident on the cavity. By directly measuring ϕ_{AC} and offsetting the phase of the microwave oscillator by the same amount, we effectively work in a frame where the center of the states remains in the $J_x - J_z$ plane: for a fixed total amount of light that passes through the cavity when $J_z = 0$ (i.e. when the J_z^2 Hamiltonian does not contribute to the phase shift), the ac-Stark shifts induce a differential phase shift of $\phi_{AC} = \int dt \delta_c n(t)$ on the clock states. Here $n(t)$ is the instantaneous mean intra-cavity photon number when $J_z = 0$, and δ_c is the differential ac-Stark shift between the clock states per photon – also equivalent to the cavity resonance shift per spin-flip. ϕ_{AC} is the experimentally controlled quantity that goes into the calculation of magnification factors. To measure this quantity for each injection of light into the cavity throughout the experimental sequence, we do Ramsey sequences centered around these injections. We start with the state on the J_x -axis, and after the light pulse we apply a $\pi/2$ rotation about the J_x -axis, which converts the accumulated phase ϕ_{AC} into population difference, which we consecutively read out via fluorescence. Together with each injection of light, we offset the phase of the microwave oscillator by the measured ϕ_{AC} so that the relative phase between the microwave oscillator and the atoms remains unaltered.

The magnification parameter

$$M = N \frac{\delta_c \delta_0}{\delta_0 + (\kappa/2)^2} \delta_{AC} \quad (5.1)$$

obtained in this implementation of the one-axis twisting Hamiltonian directly relates to the measured quantity ϕ_{AC} . Here, $\delta_c = 2\pi \times 5.5\text{Hz}$ is the cavity frequency shift per unit J_z , $\kappa = \{2\pi \times 8.0, 2\pi \times 10.4\}\text{kHz}$ is the cavity full-linewidth at $N = 5 \times 10^5$, and δ_0 is the empty cavity-light detuning. The decay of the cavity field results in back-action noise that is not taken into account in the simple Hamiltonian analysis above. However, these effects are insignificant in the parameter range we use for the magnification protocol, and can be ignored §5.4.

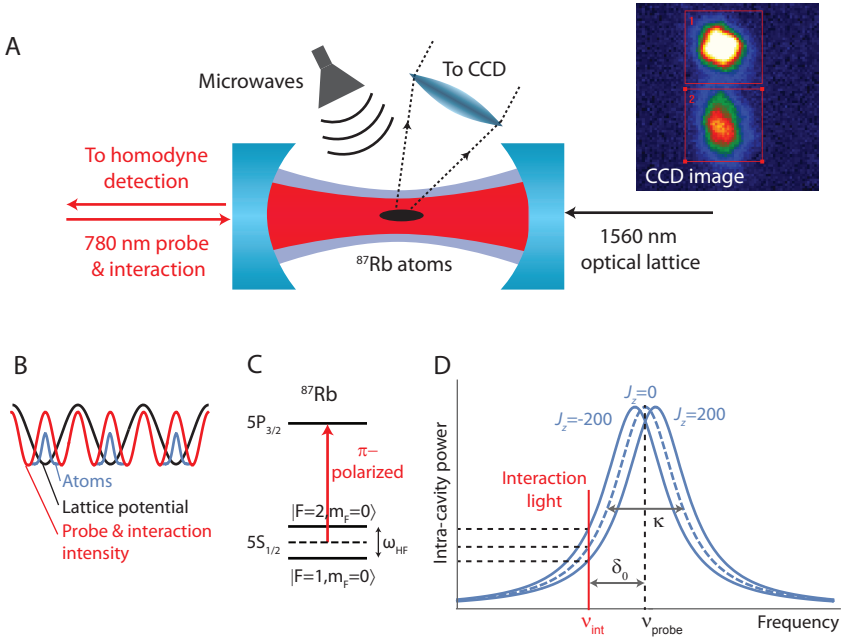


Figure 5.2: (A) ^{87}Rb atoms are trapped inside a 10.7 cm long high-finesse cavity using a 1560 nm cavity mode as a 1D optical lattice. A 780 nm mode is used to generate collective atomic interactions and to probe the cavity resonance frequency (J_z measurements) by recording the phase of a reflected $\sim 10\text{pW}$, $200\mu\text{s}$ probe pulse. Microwaves are for atomic state rotations. A CCD imaging system measures the population difference between the hyperfine states after releasing the atoms from the lattice and spatially separating the states. (B) Due to the commensurate frequency relationship between the trapping and the interaction/probe lasers, all atoms are uniformly coupled to the 780 nm mode. (C) The 780 nm mode couples the two hyperfine clock states separated by ω_{HF} to the excited manifold with opposite detunings. Thus, the two states pull the index of refraction seen by the light in opposite directions, leading to a cavity frequency shift proportional to J_z . (D) The mechanism leading to the collective atomic interactions (J_z^2 Hamiltonian) that enables the magnification process: linking of the intra-cavity power to J_z , producing a J_z -dependent ac-Stark shift. The frequencies of the interaction, ν_{int} , and probe beams ν_{probe} are indicated.

5.2 Coherent state magnification

We load up to 5×10^5 atoms at 25 mK into a 520 mK-deep optical lattice inside the cavity. The 780 nm standing-wave cavity mode is used for generating the collective

interactions and probing the atoms.

In what follows, the low-noise cavity probe will be used to obtain reference information about the states before magnification, which will then be compared to the noisy fluorescence measurements after magnification.

We first prepare a CSS aligned with the J_x -axis of the Bloch sphere using 2×10^5 atoms, then apply a small microwave-induced rotation about the J_y -axis (± 2 mrad) to displace the center of the CSS to a J_z value of either plus or minus 200.

To prepare CSSs aligned with the J_x -axis of the Bloch sphere — the starting point of our experiments — we apply a $\pi/2$ rotation about the J_y -axis. Physically, this rotation is accomplished by driving the $F = 1$ to $F = 2$ clock transition with on-resonance microwaves. The $\pi/2$ rotation is implemented in two-steps: $\pi/2 - \pi_{2\pi/3}$ (subscripts indicate relative phase between pulses). This composite rotation suppresses the microwave pulse area noise, suppressing technical J_z noise levels below the relevant CSS noise level § 4.2.1. Experimentally, the absolute rotation angle is fine-tuned until the mean cavity resonance frequency shift is nulled.

As characterized by cavity measurements, the widths of the resulting distributions read within 0.5 dB of the calibrated CSS noise level [7] (Figure 5.3A). We illustrate the magnification protocol (Figure 5.1) using these characterized states. We implement the following sequence: excite the cavity with a 200 ms light pulse, detuned by $\delta_0 = 36$ kHz, to shear the state; apply a microwave $\pi/2$ -rotation about the J_x -axis; and count the atoms state selectively using fluorescence imaging (§ 3.5B).

The magnification increases linearly with incident shearing light power (Figure 5.3B), quantified by , and has the expected dependence on cavity-light detuning (Figure 5.3C). In the large-M limit, the signal-to-noise ratio (SNR) associated with the two states after magnification approaches the value measured by the cavity (Figure 5.3D), set by the intrinsic sensitivity of the quantum state. Here, SNR is defined as the separation between the centroids of the two distributions divided by the rms width of their distributions.

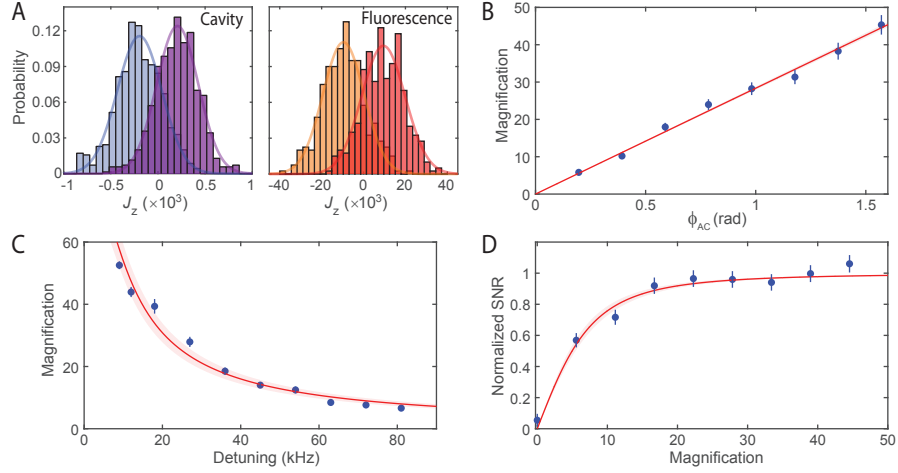


Figure 5.3: Characterization of the basic magnification process with CSSs. (A) Sample distributions (400 samples each) comparing the cavity based measurements of J_z with fluorescence imaging based measurements after a magnification of $M = 45$. The two distributions in each plot correspond to different initial states with $\langle J_z \rangle = \pm 200$ prepared using 2×10^5 atoms. (B-C) Magnification of the separation between the two distributions as a function of (B) accumulated ac-Stark phase shift ϕ_{AC} imparted on the atoms at fixed cavity-light detuning of 36 kHz, (C) cavity-light detuning δ_0 at fixed $\phi_{AC} = 0.6\text{rad}$. Solid lines: fits to the data as a function of ϕ_{AC} and δ_0 respectively in the magnification formula given in text. Fitted curves agree to within 10% with theoretical curves (not shown). (D) SNR associated with the two distributions as a function of the magnification parameter, normalized to that obtained by the cavity measurements (Normalized SNR). Magnification is varied by changing ϕ_{AC} . Solid line: fit of the form $M/(\alpha^2 + M^2)^{1/2}$; fit parameter α contains information primarily about fluorescence detection noise. Error bars and shaded regions in all panels: 68% statistical confidence interval for data and fits respectively.

5.3 Squeezed state magnification

For the mapping to be accurate in this protocol, the magnified J_z noise $\Delta J_z(0)$ should exceed the initial J_y noise $\Delta J_y(0)$. If we magnify a J_z -squeezed state which has $\Delta J_z = \Delta_{CSS}\xi$ and $\Delta J_y(0) = \Delta_{CSS}\xi'(\xi' \cdot \xi \geq 1, \xi \leq 1)$, the final noise becomes $\Delta J_y((\Delta_{CSS}\xi')^2 + (M\Delta_{CSS}\xi)^2)^{1/2}$. To set the fractional noise contribution of the second term to $1 - \varepsilon$, a magnification of $M_\varepsilon = (2\varepsilon)^{-1/2}\xi'\xi$ is required. This quantity grows unfavorably (at least quadratically) with the squeezing factor ξ .

The unfavorable scaling can be eliminated using a noise re-focusing version of the protocol (Figure 5.1D) which enables, in principle, perfect mapping at a chosen magnification. By adding a small rotation θ before magnification, the J_y noise can be made to focus down through the course of magnification. The action of the small rotation is formally analogous to that of a lens on a beam of light. The final noise in this version reads

$$\Delta J_y = [(1 - M\theta)^2(\Delta_{CSS}\xi)^2 + (M\Delta_{CSS}\xi)^2]^{1/2} \quad (5.2)$$

For $\theta = \theta_0$, the initial J_z noise becomes the sole noise contribution at $M = M_0 \equiv 1/\theta_0$.

5.3.1 Squeezed state generation

To generate squeezed states, we use the same shearing interaction used for magnification. The manner in which a state becomes squeezed due to the shearing interaction can be seen in Figure 5.1B. Starting from a CSS, the Wigner distribution becomes narrower in a particular direction as the shearing is increased. To obtain J_z -squeezing, a small final microwave rotation about the J_x -axis needs to be applied.

The squeezed state generation closely follows the one described in ref. [47]. The difference here lies in our use of large cavity-light detunings ($\delta_0 \sim 4\kappa$ instead of $\delta_0 \sim \kappa/2$). We choose a sufficiently large detuning such that the assumed linear intra-cavity power dependence on J_z is valid for the entire CSS noise distribution: At 5×10^5 atoms, the 4-sigma J_z noise for a CSS is equivalent to $\sim \kappa$ in terms of cavity shift. This is to be compared with our $\sim 4\kappa$ detuning. In this further detuned regime [70] the back-action on J_y due to cavity decay (the measurement back-action) is reduced at the expense of a decreased shearing strength for the same amount of input light (Figure 5.4C). In principle, this makes the interaction more ideal in terms of noise-area preservation for a given target squeezing level, until the point at which the spin-flips due to spontaneous emission become the limiting factor to the achievable squeezing.

Although the shearing interaction should be near-area preserving for our range

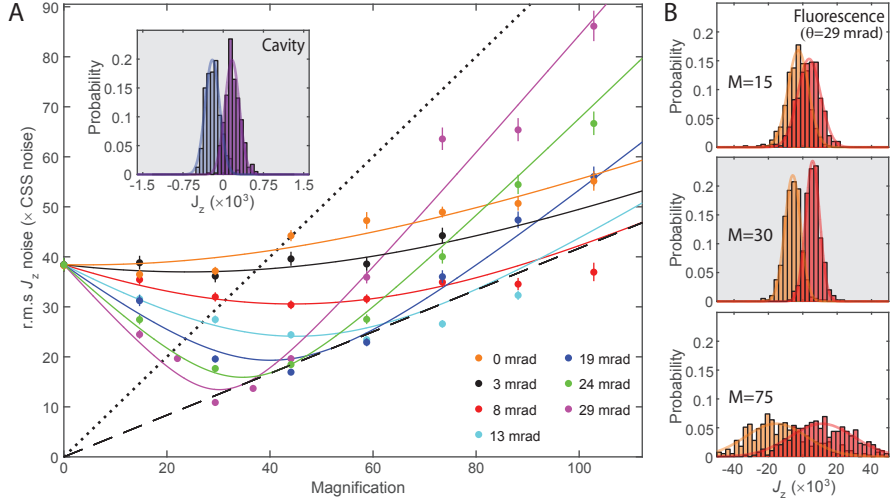


Figure 5.4: (A) Post-magnification J_z noise in units of CSS noise for different amounts of prior rotation θ about the J_x -axis Figure 5.1D. Solid lines are a global fit to the entire data set with two free parameters: $d\theta/dt$, the rate of change in θ with microwave pulse time; and the J_z noise of the initial squeezed states. Obtained values are within 15% of the calculated values. The inset shows the distribution of two separated 8 dB squeezed initial states (5×10^5 atoms) as identified by cavity measurements [to be compared with the $M = 30$ distribution in (B)]. Dashed line: M times the J_z noise contribution from the initial squeezed states. Dotted line: M times the CSS noise – the SQL. Error bars: 68% statistical confidence interval. (B) The distributions after the magnification protocol at the indicated M values for $\theta = 29$ mrad. The normalized SNR becomes 0.96 ± 0.06 at $M \approx 1/|\theta|$ (middle histogram), where the dashed line is tangent to the $\theta = 29$ mrad noise curve in (A). For M values to either side of $1/|\theta|$, the two distributions blur into each other (top and bottom histograms).

of parameters, as is evident from the generated squeezed states with 8 dB squeezing and 32 dB anti-squeezing, there is apparent area non-preservation. This area non-preservation is a result of statistical ensemble averaging in presence of technical noise, effectively giving rise to mixed states. There are two main contributions. The first contribution is from the technical pulse area noise of the light generating the shearing. The J_y noise increases with pulse power due to increasing absolute ac-Stark shift precession noise. The second contribution is from the microwave phase noise. The mean J_z value of the generated squeezed states after the microwave rotation that concludes state preparation is crucially dependent on the location of the rotation

axis. For 5×10^5 atoms, we observe 10-15 dB above CSS noise uncertainty in the rotation axis location due to microwave phase noise. Because of these effects, at low shearing powers we do not observe noise levels below the CSS noise, and at higher levels ($\phi_{AC} = \pi/8$) squeezing saturates around 8 dB.

5.3.2 Pulse sequences for the experiments

The sequences A and B in Figure 5.5 were used for characterizing the basic magnification protocol with CSSs. Sequence A was used for generating the cavity-based histograms (Figure 5.3A, left). Sequence B was used for generating the fluorescence-based histograms (Figure 5.3A, right) and for exploring the parametric dependencies of the magnification protocol (Figure 5.3B-D). Sequences C and D were used for characterizing the noise re-focusing scheme with squeezed spin states. Sequence C was used to show the existence of an optimum magnification (Figure 5.3A) for each tilting angle $\theta > 1$ (Figure 5.1D). Sequence D was used for exploring the magnification dependence of the obtained distributions (Figure 5.4B) for fixed θ . The inset of Figure 5.4A was generated using a sequence where the state preparation part of sequence D was followed by a measurement of J_z with the cavity.

All sequences (Figure 5.5) start with a composite $\pi/2$ -pulse to prepare a CSS aligned with the J_x -axis, as described above in § 3.3, and end with either a cavity measurement or fluorescence imaging. In absence of any atoms, the light pulses labeled ‘Measure’ are on resonance with the cavity, and the ones labeled ‘Shear’ are detuned by δ_0 (Figure 5.1). The microwaves with e-pulse area are tuned to displace the states from $\langle J_z \rangle = 0$ to $\langle J_z \rangle = \pm 200$, and the microwaves with y-pulse area are tuned to align the minimum-noise direction of the prepared squeezed states with the J_z direction. The microwave phase-shift keying (labelled PSK in the figure) is performed by doing a fixed duration frequency-shift key on the microwave frequency. The extra PSK angle $\pm\varphi$ (Figure 5.5D) is tuned to ensure that the squeezed states with $\langle J_z \rangle = \pm 200$ maintain the $\langle J_y \rangle = 0$ condition.

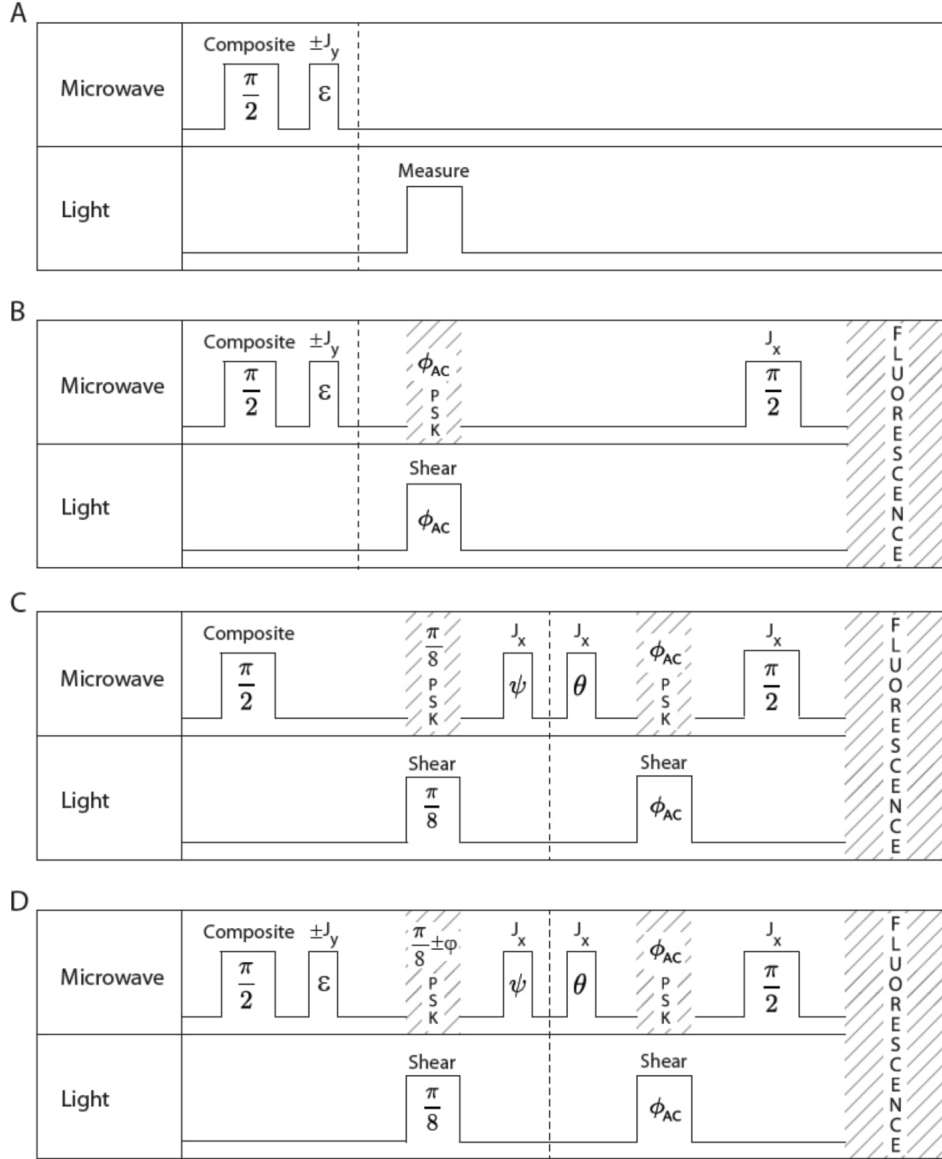


Figure 5.5: The sequences are split into two parts with dashed lines; to the left are the state preparations, to the right are the magnification protocols and measurements. The axis of rotation is indicated above each microwave pulse. The pulse areas for light are given in terms of the mean ac-Stark phase shifts induced on the atomic states. (A) Preparation of CSSs at $\langle J_z \rangle = \pm 200$ followed by a measurement of J_z with the cavity. (B) Preparation of the same CSSs followed by the basic magnification protocol and fluorescence imaging. The induced ac-Stark phase shift ϕ_{AC} due to the shearing pulse is compensated for by shifting the phase of the microwave oscillator (shaded region with PSK label). (C) Preparation of squeezed states with $\langle J_z \rangle = \langle J_y \rangle = 0$ followed by the noise re-focusing magnification protocol and fluorescence imaging. (D) Preparation of squeezed states with $\langle J_z \rangle = \pm 200$ followed by the noise re-focusing magnification protocol and fluorescence imaging

5.3.3 Noise re-focusing with squeezed states

We demonstrate the noise re-focusing protocol using squeezed spin states with 5×10^5 atoms (Figure 5.4). We start with states 8 dB squeezed in J_z and 32 dB anti-squeezed in J_y ($\xi \sim 0.4, \xi' \sim 40$) – the best we can currently achieve without measurement based methods. We apply a small microwave rotation θ about the J_x -axis, and investigate the noise measured at the end of the magnification protocol (Figure 5.4A). We observe a different optimal magnification value for each θ . The shown family of model curves (using the Equation 5.2) is a fit to the entire data set with only two free parameters, and the small deviations from these curves are attributable to slow drifts in the initial squeezing level (~ 1 dB). For the specific example of $\theta = 29$ mrad (Figure 5.4B) we explicitly show that the optimal magnification $M \sim 30$ replicates the SNR of the initially prepared states. Had we not utilized noise re-focusing, the required magnification would have been $M_{0.05} \sim 320$ (for an infidelity $\varepsilon = 0.05$), which would have started wrapping the states around the Bloch sphere. In assessing metrological gain obtained from spin squeezing, the degree of Bloch vector length (coherence) preservation is essential in order not to degrade signal levels. Throughout all state preparation and magnification, the coherence of the states measured by Ramsey fringe contrasts remains above 96%. The small reduction arises from residual atom-cavity coupling inhomogeneities (§ 4.9).

5.4 The shearing interaction in the atom-cavity system

A systematic treatment of the shearing interaction in a driven atom-cavity system is examined in the supplemental materials of ref. [69] using the Lindblad master equation formalism. In this section we derive the specific equations used in the main text for the magnified mean and noise expressions. We do this in a targeted fashion using the Heisenberg-Langevin formalism starting from an atom-cavity-reservoir Hamiltonian. We first elucidate the connection between the one-axis twisting Hamiltonian used in the main text and the experimentally realized dispersive atom-cavity system. We then

then clarify why the former is sufficient to explain the results of the current work. We use the derived results to analyze the limitations of the magnification scheme in the next section.

We take the interaction picture Hamiltonian for the physical system as

$$\begin{aligned} H^{(I)} = & \hbar\delta_c J_z a^\dagger a - \hbar\delta_c J_z |\alpha(0, t)|^2 - \hbar (\beta^*(t)e^{i\delta_0 t} a + \beta(t)e^{i\delta_0 t} a^\dagger) \\ & - \hbar \sum_k \sqrt{\frac{\kappa c}{2L}} (a_k^\dagger a e^{i(\omega_k - \omega_c)t} + a_k a^\dagger e^{-i(\omega_k - \omega_c)t}) \end{aligned}$$

The first term is the dispersive atom-cavity interaction shifting the cavity resonance frequency by δ_c per spin-flip, or equivalently generating a differential ac-Stark shift δ_c on the clock states per intra-cavity photon; a is the cavity mode annihilation operator. The second term is a specific choice of a rotating frame for taking out the mean precession; $|\alpha(0, t)|^2$ is the time dependent mean intra-cavity photon number for $J_z = 0$. The third term accounts for the excitation of the cavity mode with an incident laser; $\beta(t)$ is the driving amplitude, δ_0 is the cavity-light detuning. The last term phenomenologically induces the decay of the cavity modes at a rate κ to a continuum of modes with dispersion relation $\omega_k = ck$ in a 1D-space extending from $-L/2$ to $L/2$ ($L \rightarrow \infty$ limit is taken); a_k are the decay mode annihilation operators, ω_c is the cavity resonance frequency. Since this decay is phenomenological we also include the loss due to atomic scattering in this term: $\kappa = \kappa_0 + N\delta_c\Gamma/\omega_{HF}$; κ_0 is the measured empty cavity decay rate, the second term is the total atomic scattering rate assuming $J_z \sim 0$ and atom-cavity detunings of $\pm\omega_{HF}/2$ as shown in Figure 5.1.

The relevant Heisenberg equations of motion that can be derived from the above Hamiltonian using the standard methods of the Heisenberg-Langevin approach [71] are

$$\begin{aligned} J_z(t) &= J_z(0) \\ \dot{a} &= \left(-i\delta_c J_z - \frac{\kappa}{2}\right) a + i\beta(t)e^{-\delta_0 t} + f_a \\ \dot{J}_y &= -\delta_c |\alpha(0, t)|^2 J_z + \delta_c a^\dagger J_x a \end{aligned}$$

Here $f_a(t) = i \sum_k \sqrt{\frac{\kappa c}{2L}} a_k(0) e^{-i(\omega_k - \omega_c)t}$ is a noise operator. This operator and the decay term in the second equation encapsulate the effects of the reservoir.

Now we show that the intra-cavity field amplitude becomes linked to J_z in the limit of slowly varying drive amplitude; $|\dot{\beta}(t)/\beta(t)| \ll |\delta_c J_z - i\kappa/2|$. We integrate the equation for \dot{a} by parts assuming $\beta(0) = 0$, drop the arising integration involving $\dot{\beta}(t)$, and take the long time limit $t \gg 1/\kappa$ to obtain $a(t) = -\alpha(J_z) - f'_a(J_z, t)$. Here $\alpha(J_z, t) = \frac{\beta(t)e^{-i\delta_0 t}}{\delta_0 - \delta_c J_z(0) + i\kappa/2}$, and yields $\alpha(J_z, t) \sim \alpha(0, t) \left(1 + \frac{\delta_c}{\delta_0 + i\kappa/2} J_z\right)$ when Taylor expanded around $J_z = 0$ to obtain the lowest order correction to the field amplitude due to the atoms. $f'_a(J_z, t)$ is a noise operator proportional to $a_k(0)$. Since the decay modes are assumed to be initially in vacuum state, this noise operator will vanish when acting on the initial reservoir state. To facilitate such simplifications we adhere to normal operator ordering.

At this stage we invoke the simplifying assumption that restricts us to a planar patch on the surface of the Bloch sphere, linearizing the equations, with the substitution $J_z \rightarrow J \equiv N/2$. This approximation works well if the J_y values remain within $\pm 0.2J$, covering the experimentally relevant range. Substituting the obtained lowest order $a(t)$ into the equation for \dot{J}_y and dJ_y^2/dt , and taking the expectation values both over the decay modes and the spins, we get

$$\begin{aligned}\langle J_y \rangle &= \langle J_y(0) \rangle + M \langle J_z(0) \rangle \\ \langle J_z^2 \rangle &= \langle J_y^2(0) \rangle + M \langle J_z J_y(0) + J_y J_z(0) \rangle + M^2 \langle J_z^2(0) \rangle + \frac{N}{4} M \frac{\kappa}{\delta_0}\end{aligned}$$

Here $M = N \frac{\delta_c \delta_0}{\delta_0 + |\kappa/2|^2} \phi_{AC}$ with $\phi_{AC}(t) = \int_0^t dt' \delta_0 |\alpha(0, t')|^2$. Note that $|\alpha(0, t)|^2$ is the instantaneous mean intra-cavity photon number $n(t)$ for $J_z = 0$ (equivalently, in absence of atoms). The second equation utilizes the intermediate step of obtaining $\langle J_z J_y + J_y J_z \rangle = \langle J_z J_y(0) + J_y J_z(0) \rangle + 2M \langle J_z^2(0) \rangle$ using the first one. These equations allow one to calculate the mean and variance of J_y after magnification in terms of expectation values of initial means and symmetrized (co)variances. We obtain

$$\text{var}(J_y) = \text{var}(J_y(0)) + 2M\text{cov}(J_y(0), J_z(0))_{\text{sym}} + M^2\text{var}(J_z(0)) + \frac{N}{4}M\frac{\kappa}{\delta_0}$$

The last term is the only addition to the result that would have been obtained from the one-axis twisting Hamiltonian. It represents the effect of cavity decay (measurement back-action). It is negligible in comparison to the previous terms for our range of parameters, and hence can be dropped. The formula for ΔJ_y in the main text for the noise re-focusing version can be obtained by using the (co)variances appropriate for initially J_y -squeezed states rotated by a small angle θ about the J_x -axis, and making the small angle and large magnification approximations. The (co)variances are

$$\begin{aligned}\text{var}(J_y(0)) &= \sin^2 \theta \text{var}(J'_Z) + \cos^2 \theta \text{var}(J'_y) \\ \text{var}(J_z(0)) &= \cos^2 \theta \text{var}(J'_Z) + \sin^2 \theta \text{var}(J'_y) \\ \text{cov}(J_y(0), J_z(0))_{\text{sym}} &= -\frac{1}{2} \sin^2 \theta (\text{var}(J'_y) - \text{var}(J'_z))\end{aligned}$$

Here the primed variances belong to the J_z -squeezed state before rotation. The $\theta = 0$ limit recovers the noise for the basic version of the protocol.

5.5 Experimental Extraction of the magnification parameters

In Figure 5.3 we do measurements to calibrate magnification values, whereas in Figure 5.4 we use these calibrations to calculate magnifications. The calibrated values are extracted through a comparison of cavity and fluorescence measurements. In particular, we measure the separations between the centroids of two distributions, first with the cavity (Figure 5.3A, left), and then with fluorescence imaging after magnification (Figure 5.3A, right). The ratio of the measured separations gives the magnification. We typically use 800 measurements to determine a given centroid separation with each method.

Note that prior to these measurements, the J_z values measured by the cavity and the ones measured by fluorescence imaging are directly calibrated with respect to each other as follows. Two separate CSSs are prepared whose central J_z values are sufficiently separated, such that they can be resolved by both the cavity measurements and the fluorescence measurements (without magnification). By comparing the results of the two methods, counts measured on the CCD camera are calibrated with respect to cavity frequency shifts. Note that since these separations do not fit in one cavity linewidth, we hop the frequency of the probe laser to measure the cavity frequency separation associated with the two states. Finally, the $\delta_c = 5.5\text{Hz}$ value (calculated and experimentally verified to within 10% through ac-Stark shift measurements) is used to convert the measured cavity frequency shifts into J_z .

5.6 Effects of fluctuations in experimental parameters

Although we do not observe any degradation in the measured SNRs after magnifications with optimal parameters, we will nevertheless analyze the effects of noisy experimental parameters. The Hamiltonian that we implement is given by $H = \hbar J_z^2 + \hbar \bar{\beta} J_z$ (equivalently $H = \hbar \chi J_z^2 + \hbar \delta \beta J_z$), where $\chi = \frac{\delta_c \delta_0}{\delta_0^2 + (\kappa/2)^2}$ and $\beta = \delta_c n(t)$, and $\int dt \beta(t) \equiv \phi_{AC}$. Here and in what follows, we split noisy experimental parameters into their means and their small fluctuations; e.g. $\beta = \bar{\beta} + \delta \beta$, where the first term of the Hamiltonian implements the magnification, the second term comes from the J_z -independent global rotations, and the third term represents our compensation of the global rotation by going into a rotating frame that maintains the $\langle J_y \rangle = 0$ condition. The equation of motion dictated by this Hamiltonian (under the linearizing approximation $J_z \rightarrow J = N/2$) is $J_y = J_y(0) + \bar{M} J_z(0) + \delta J_y$. The small deviation δJ_y from the ideal mapping due to the fluctuating experimental parameters is $\delta J_y = (J_z(0) \bar{M}) \delta N / \bar{N} + (J_z(0) \bar{M} + \frac{1}{2} \bar{N} \bar{\phi}_{AC}) \delta \phi_{AC} / \bar{\phi}_{AC}$, where the mean magnification parameter is given by $\bar{M} = \frac{\delta_c \delta_0}{\delta_0^2 + (\kappa/2)^2} \bar{\phi}_{AC}$. Note that the fluctuating parameters $\delta \phi_{AC}$ and δN , and consequently δJ_y are random variables with zero mean. In order to obtain actual

noise values, an ensemble average needs to be taken. Assuming uncorrelated ϕ_{AC} and $\delta N(\langle\phi_{AC}\delta N\rangle_e = 0)$, the variance of J_y is found to be

$$\text{var}_e(J_y) \equiv \langle\delta J_y^2\rangle_e = J_z^2(0)\bar{M}^2\text{var}_e\left(\frac{\delta N}{\bar{N}}\right) + \left(J_z(0)\bar{M} + \frac{1}{2}\bar{N}\bar{\phi}_{AC}\right)^2 \text{var}_e\left(\frac{\delta\phi_{AC}}{\bar{\phi}_{AC}}\right) \quad (5.3)$$

Here, the subscript ‘e’ denotes averages over an ensemble of experimental parameters to prevent confusion with quantum expectation values. We see that the variance contains a magnification-independent part (originating from the global ac-Stark rotations) in addition to magnification-dependent parts (originating from the magnification noise) which grow larger as the center of the pre-magnification states goes farther away from $J_z = 0$. The magnification-independent contribution dominates for our range of parameters. As an example, we will use $\bar{M} = 30$, $\bar{N} = 5 \times 10^5$ corresponding to $\phi_{AC} \approx \pi/7$ (as in Figure 5.4B, middle), with initial states localized well within $|J_z| = 1 \times 10^3$. If we further use the measured 2% rms noise on atom numbers and the upper bound of 1% rms on the shearing pulse area noise, the technical noise contribution to the fluctuations on J_y can be approximated by $\langle\delta J_y^2\rangle_e^{1/2} \approx \frac{1}{2}\bar{N}\langle\delta\phi_{AC}^2\rangle_e^{1/2} \leq 1.1 \times 10^3$. This noise adds in quadrature with the magnified quantum noise which is approximately $10\Delta_{CSS} = 3.5 \times 10^3$ (Figure 5.4A, $\theta = 29\text{mrad}$, $M = 30$), and thus gives rise to an excess noise of a maximum of 5%. This difference is not statistically resolvable in the measurements, and hence the measured normalized SNR of 0.96 ± 0.06 is compatible with the noise estimations presented here.

5.7 Limits

In ref. [69] it has been shown that using the one-axis twisting Hamiltonian $h = \hbar\chi J_z^2$ in the shear-unshear mode, it is in principle possible to reach the Heisenberg limit to measurement precision with a required detection resolution only at the CSS noise level. It was also shown that for an implementation of the sort described in our work, the Heisenberg limit is not achieved due to the atomic and cavity decays, but instead

a metrological gain that is limited by $\sim \sqrt{NC}$ is obtained. Here C is the single atom cooperativity. In this section, we analyze the minimum squeezed-state noise that can be resolved using the noise re-focusing magnification protocol that we presented. We build upon the formulas derived in the previous section. We find a similar \sqrt{NC} scaling in the metrological gain with a universal saturation limit of ~ 30 dB for ^{87}Rb atoms. The important difference is that with the current method, in principle, the detection sensitivity requirement can be relaxed to arbitrarily chosen levels.

We will use the following relations in the derivation: The cooperativity C is defined as $C = 4g^2/\kappa_0\Gamma \approx 0.78$ with g , the atom-cavity coupling; Γ , the atomic excited state decay rate; κ_0 , the empty cavity decay rate. The atomic-absorption-broadened cavity linewidth is denoted by κ with $\kappa/\kappa_0 = 1 + NC(\Gamma/\omega_{HF})^2$. The per spin-flip cavity frequency shift is $\delta_c = 4g^2/\omega_{HF}$.

We assume a given initial J_z -squeezed state with $\Delta J(0) = \xi\Delta_{CSS} = \xi\sqrt{N}/2$. Working at the optimal magnification point $M = 1/\theta$ ($\theta \ll 1$) of the noise re-focusing scheme, the variance after magnification is given by $\text{var}(J_y) = \frac{N}{4}M^2\xi^2 + \frac{N}{4}M\frac{\kappa}{\delta_0}$. The first term comes purely from the initial J_z noise. The second term is the spurious contribution from the cavity decay, and can be suppressed by increasing the cavity-light detuning δ_0 at the expense of an increased amount of light to achieve the same magnification M . Thus, at large detunings one needs to carefully consider the effects of spontaneous emission, which will effectively limit δ_0 . As described in ref.[7], spin-flips caused by spontaneous emission events gives rise to a diffusion of with a variance given by $\sigma_{flip}^2 = \frac{N}{6}\frac{\Gamma}{\omega_{HF}}\phi_{AC} = \frac{1}{6C}M\frac{\delta_0}{\kappa_0}$. The second equality assumes $\delta_0 \gg \kappa/2$.

For the magnification to work properly, by the time one reaches the optimal magnification point, the total spin-flip noise due to spontaneous emission should not exceed the initial J_z noise ($\sigma_{flip}^2 \leq \xi^2\frac{N}{4}$). This sets the maximum usable detuning to $\delta_0 = \frac{3}{2}NC\kappa_0\xi^2/M$. Inserting this into the post-magnification J_z variance we obtain: $\text{var}(J_y) = \frac{N}{4}M^2\xi^2 + M^2\frac{1+NC(\Gamma/\omega_{HF})^2}{\xi^2}\frac{1}{6C}$. We will assume that the initial state is no longer accurately resolvable when the second term becomes equal to the first one. Equating the two terms gives us an estimate of the best resolving power for the magnification scheme that our atom-cavity implementation with ^{87}Rb atoms can achieve in principle. The smallest squeezing parameter that can be resolved is given

by

$$\xi_{min}^2 = \sqrt{\frac{1 + NC(\Gamma/\omega_{HF})^2}{\frac{3}{2}NC}} \quad (5.4)$$

It appears that the achievable limits do not depend on the choice of magnification as long as one operates at the optimal point of the noise re-focusing scheme. ξ_{min}^2 first decreases with atom number as $1/\sqrt{\frac{3}{2}NC}$ and saturates at $\xi_{sat}^2 = \sqrt{\frac{2}{3}}(\Gamma/\omega_{HF}) \equiv -31\text{dB}$ due to the effects of atomic absorption. For our experimental parameters with $N = 5 \times 10^5$, we obtain $\xi_{min}^2 \sim -28\text{dB}$.

5.8 Generalization to many systems

If the magnification technique developed here is used as the read-out stage for the more effective measurement-based squeezing methods, we expect superior results to be obtained due to the improved the read-out – fundamentally through bypassing inefficiencies due to photon losses. The magnification protocol can be used on any kind of exotic initial state to ease characterization. Examples include the yet to be demonstrated Schrodinger-cat spin states [72, 73]), where cat-fringe spacing can be magnified, or other states that possess negative Wigner functions [64]. Since the only required key element is a nonlinear phase shift, the method could find broad use in systems utilizing, e.g., collisional interactions in Bose-Einstein condensates [42, 74, 75], Rydberg blockade interactions in neutral atoms [69], Ising interactions in ion traps [76], nonlinearities in superconducting Josephson junctions, and nonlinearities in optics.

The state magnification concept investigated in the context of atomic systems has an optical analogue. The method carries over to optical self-phase modulation in a medium with Kerr nonlinearity. This system magnifies the amplitude of an optical excitation by mapping it onto its phase, which can then be read out with homodyne detection.

The interaction picture Kerr Hamiltonian is given by $H^{(I)} = -\hbar\chi a^{\dagger 2}a^2 + 2\hbar\chi|a|^2a^\dagger a$

[6]. Here the first term is the actual Kerr Hamiltonian, and the second term is a choice of a rotating frame (in phase space) that takes out the residual linear phase evolution induced by the first term.

We are interested in initial states with slightly differing mean amplitudes centered about a reference value $|\alpha| \gg 1$, i.e., $(\langle X \rangle^2 + \langle Y \rangle^2)^{1/2} \approx |\alpha|$. Here $X = (a + a^\dagger)/2$ and $Y = (a - a^\dagger)/2i$ are the quadrature operators with the commutation relation $[X, Y] = i/2$. To simplify the problem, we go into a displaced picture using the displacement operator $D \equiv D(\alpha)$ (with $\alpha = |\alpha|e^{i\phi}$), whose action can be summarized by the relation $D^\dagger(\alpha)aD(\alpha) = a + \alpha$. This takes out the large quantity $|\alpha|$ from the states, and makes it explicitly a part of the new Hamiltonian $H^{(DI)} = D^\dagger H^{(I)} D$. The displaced-picture quantum states are related to the original picture by $|\psi^{(D)}\rangle = D^\dagger |\psi\rangle$. In terms of the displaced-picture operators \tilde{X}, \tilde{Y} and \tilde{a} , the original operators are $X \equiv \tilde{X} + \alpha_{Re}$, $Y \equiv \tilde{Y} + \alpha_{Im}$ and $a \equiv \tilde{a} + \alpha$.

Ignoring the small terms proportional to $|\alpha|^1$ and $|\alpha|^0$, and dropping the constant terms as they arise, the displaced-picture Hamiltonian is given by

$$H^{(DI)} \approx -\hbar\chi (\alpha^2 \tilde{a}^{\dagger 2} + \alpha^{*2} \tilde{a}^2 + 2|\alpha|^2 \tilde{a}^\dagger \tilde{a}) = -\hbar 4\chi |\alpha|^2 (\cos \phi \tilde{X} + \sin \phi \tilde{Y})^2 \quad (5.5)$$

For simplicity, we assume that the states of interest are near the X-axis in phase space, and thus we set $\phi = 0$, $\alpha_{Im} = 0$, and obtain $H^{(DI)} = -4\hbar\chi |\alpha|^2 \tilde{X}^2$. The Heisenberg equations of motions are given by

$$\dot{\tilde{X}} = 0 \quad (5.6)$$

$$\dot{\tilde{Y}} = 4\chi |\alpha|^2 \tilde{X} \quad (5.7)$$

Solving these equations, for the original observables we obtain

$$\langle X(t) \rangle = \langle \tilde{X}(0) \rangle + \alpha_{Re} \quad (5.8)$$

$$\langle Y(t) \rangle = \langle \tilde{Y}(0) \rangle + M \langle \tilde{X}(0) \rangle \quad (5.9)$$

$$var(X(t)) = var(\tilde{X}(0)) \quad (5.10)$$

$$2var(Y(t)) = var(\tilde{Y}(0)) + 2M cov(\tilde{X}(0), \tilde{Y}(0))_{sym} + M^2 var(\tilde{X}(0)) \quad (5.11)$$

Here $M = 4\chi|\alpha|^2t$, and expectation values are taken using the displaced-picture states. These equations are directly analogous to the shearing interaction we implement for our atomic system: The initial amplitude quadrature signal is mapped onto the phase quadrature with magnification M , which can be detected with homodyne detection. With appropriate initial states, containing correlations between the two quadratures, i.e., $\text{cov}(\tilde{X}(0), \tilde{Y}(0))_{\text{sym}} \neq 0$, noise re-focusing schemes are possible here as well.

The analysis provided here is valid as long as the mean X values are much larger than the values associated with the post-magnification Y distributions. Failure to satisfy this condition makes the approximation for the simplified displaced-picture Hamiltonian invalid. Outside of the regime considered here, the states are driven into crescent shapes in phase space [6]

Chapter 6

Bell Correlation Measurements

In this final chapter I will introduce the concept of a Bell's Witness and explain how the squeezed states that we created (Chapter 4) demonstrate strong Bell correlations. This work was published in 2017 [9].

The progress in the control of quantum systems has been accompanied by the development of metrics quantifying quantum correlations in many-body systems [77–80]. A widely adopted measure for systems with large numbers of particles is the depth of entanglement [81–83]. This measure characterizes the minimal number of particles that are mutually entangled in a system. However, not all types of quantum correlations can be classified using the concept of entanglement alone [84]¹. An example is the Bell-type correlations which are exhibited by quantum systems violating Bell's inequalities [85].

Demonstrating nonlocal Bell correlations was restricted to small systems in which the individual components of a composite quantum system can be measured directly. Bell correlations have been shown with photons [86–89], ions [90], atoms [91], solid state spins [92] and NV centers [93]. To extend the investigation of Bell correlations to larger systems, a new framework was developed in [94] that enables observation of Bell correlations without accessing individual components of a system. This

¹A set of examples is displayed in the Werner states, which are mixed states defined by the density matrix $\rho = p|\phi_+\rangle\langle\phi_+| + (1-p)I/4$. Here, $|\phi_+\rangle = \frac{1}{\sqrt{2}}(|\uparrow\uparrow\rangle + |\downarrow\downarrow\rangle)$ is a Bell state and the identity matrix I represents a maximally mixed state. For $1/3 < p < 1/2$ these states are entangled but do not violate any Bell inequalities.

framework provides a method to witness whether a quantum many-body system features nonlocality, as evidenced by Bell correlations. The method was employed in [95] with measurements that access only the collective observables of a Bose-Einstein condensate of 480 ^{87}Rb atoms to demonstrate Bell correlations with a statistical significance of 3.8 standard deviations. In this chapter, we show Bell correlations in spin-squeezed states in a thermal ensemble of 5×10^5 ^{87}Rb atoms at $25\ \mu\text{K}$ which are statistically significant to 124 standard deviations. While our result demonstrates the presence of Bell correlations, it cannot be used to perform loophole free tests of Bell's inequalities, as the measurement duration is longer than the time of flight for light across the sample (the no-communication loophole [84]), and the Bell correlation witness (Equation 6.2) a priori assumes quantum mechanics in its derivation [95].

6.1 Theory

We model our atomic ensemble as a system of N spin-1/2 particles. Experimentally, we utilize the clock states of ^{87}Rb and define $|F = 2, m_F = 0\rangle \equiv |\uparrow\rangle$ and $|F = 1, m_F = 0\rangle \equiv |\downarrow\rangle$ as our pseudo-spin states. For a measurement of the i th spin on a given axis \mathbf{m} only two measurement outcomes are possible, $j_{\mathbf{m}}^{(i)} = \pm 1/2$. Considering two possible axis choices, defined by the unit vectors \mathbf{m} and \mathbf{n} , the quantities relevant for constructing a Bell inequality are the expectation values $\langle j_{\mathbf{m}}^{(i)} \rangle$, and the correlations $\langle j_{\mathbf{m}}^{(i)} j_{\mathbf{m}}^{(k)} \rangle$, $\langle j_{\mathbf{m}}^{(i)} j_{\mathbf{n}}^{(k)} \rangle$, $\langle j_{\mathbf{n}}^{(i)} j_{\mathbf{n}}^{(k)} \rangle$. Simple algebraic combinations of these one- and two-body correlators, such as, $\mathcal{S}_{\mathbf{m}} = 2 \sum_{i=1}^N \langle j_{\mathbf{m}}^{(i)} \rangle$ and $\mathcal{S}_{\mathbf{mn}} = 4 \sum_{i,k=1, i \neq k}^N \langle j_{\mathbf{m}}^{(i)} j_{\mathbf{n}}^{(k)} \rangle$ lead to a Bell inequality under the assumption of permutation symmetry of the spins in the system [94]:

$$2\mathcal{S}_{\mathbf{m}} + \mathcal{S}_{\mathbf{mm}}/2 + \mathcal{S}_{\mathbf{mn}} + \mathcal{S}_{\mathbf{nn}}/2 + 2N \geq 0. \quad (6.1)$$

This Bell inequality can be used to derive a Bell correlation witness requiring measurements of only the collective spin vector $\mathbf{J} \equiv \sum_{i=1}^N \mathbf{j}^{(i)}$ where $\mathbf{j}^{(i)} = [j_x^{(i)}, j_y^{(i)}, j_z^{(i)}]$. The presence of Bell correlations can then be probed with measurements of these

collective observables alone [95, 96]. This is analogous to the widely adopted entanglement depth measure for characterizing entanglement in systems with large numbers of particles [81–83], which makes an inference on the size of entangled clusters from measurements of collective observables. Note that these kinds of inferences require repeated observations of identically prepared states of the system.

A particular class of collective states that can violate Equation 6.1 are spin-squeezed states [97]. For a symmetric collective state of N spins, assuming a mean polarization along the x -direction, the uncertainty of two orthogonal components of \mathbf{J} is limited by the relation $\Delta J_z \cdot \Delta J_y \geq N/4$. Spins that are each independently polarized along the x -direction comprise a coherent spin state (CSS), an unentangled minimum uncertainty state where $\Delta J_z = \Delta J_y = \sqrt{N}/2$ define the CSS noise. Spin-squeezing redistributes the uncertainty from one conjugate variable to the other, generating entanglement between the spins in the process. As a consequence of the uncertainty principle, reduction in uncertainty in one conjugate variable (squeezing) comes at the expense of a corresponding increase in the uncertainty for the other conjugate variable (antisqueezing). For sufficient amounts of squeezing, the squeezed states may also contain Bell correlations.

Choosing a specific set of measurement axes determined by two unit vectors \mathbf{z} and \mathbf{n} (Figure 6.1A), the witness function can be expressed in terms of the expectation values of the normalized collective spin operators $\mathcal{J}_{1,\mathbf{n}} \equiv \langle 2J_{\mathbf{n}}/N \rangle$ and $\mathcal{J}_{2,\mathbf{z}} \equiv \langle 4J_{\mathbf{z}}^2/N \rangle$, where $J_{\mathbf{z}} \equiv \mathbf{z} \cdot \mathbf{J}$ and $J_{\mathbf{n}} \equiv \mathbf{n} \cdot \mathbf{J}$. The witness inequality then reads [95]

$$\langle W \rangle = -|\mathcal{J}_{1,\mathbf{n}}| + (\mathbf{z} \cdot \mathbf{n})^2 \mathcal{J}_{2,\mathbf{z}} + 1 - (\mathbf{z} \cdot \mathbf{n})^2 \geq 0 \quad (6.2)$$

In this expression, the total particle number N inside the expectation values is allowed to be a fluctuating random variable, which in our experiment has a 3% standard deviation from one realization to the next. The first term can be measured by rotating the collective spin state, which amounts to changing the angle between \mathbf{z} and \mathbf{n} . $\mathcal{J}_{1,\mathbf{n}}$ can then be found by measuring the projection of the state on the z -direction after the rotation. The second term, when $\langle J_z \rangle = 0$, is simply proportional to the variance of $J_{\mathbf{z}}$ normalized to the CSS noise. Equation 6.2 is the first criterion that we will use

to demonstrate Bell correlations. From Equation 6.2 it follows that the inequality

$$\mathcal{J}_{2,\mathbf{z}} < \frac{1}{2} \left[1 - (1 - \mathcal{J}_{1,\mathbf{x}}^2)^{1/2} \right] \quad (6.3)$$

also guarantees Bell correlations (a full derivation can be found in the supplementary material of [95]). Here, assuming a squeezed state with $\langle J_z \rangle = 0$, the quantity $\mathcal{J}_{1,\mathbf{x}}$ is simply the coherence of the state. This second criterion is more robust to experimental noise and it is with this criterion we get the most statistically significant violation. Similarly to the entanglement depth criterion the Bell violation witness function is fully parametrized by the coherence (the length of the Bloch vector) and the amount of squeezing in the state [81, 82].

6.2 General Procedure

The experimental apparatus and preparation of the squeezed states is described in [7]. We trap up to 7×10^5 cold atoms in an optical lattice generated by 1560 nm light inside of an optical cavity. The cavity mirrors are coated to support both 780 nm and 1560 nm modes. A 780 nm mode is used to perform quantum non-demolition (QND) measurements of the collective state of the atoms to prepare the squeezed states. We set the detuning between the atomic resonance and the 780 nm cavity mode such that the effect of the atoms is a state-dependent change in refractive index—equal in magnitude but opposite in sign for the $|\uparrow\rangle$ and $|\downarrow\rangle$ states. The refractive index change then manifests as a cavity resonance shift, whose measurement serves as a QND measurement of $J_{\mathbf{z}}$. The technical noise limit of this QND measurement is 41 dB below the CSS noise limit, which means the QND measurement of J_z is limited only by quantum noise [7].

For the purposes of showing Bell correlations, we seek to measure the symmetric collective observable $J_{\mathbf{z}} = \sum_{i=1}^N j_z^{(i)}$. A cavity where each atom is identically coupled to the probe mode would measure this observable. In this experiment, the 1560 nm light traps the atoms at the peaks of the 780 nm standing wave intensity profile, enabling uniform coupling of the atoms to the probe. However, there is still some residual

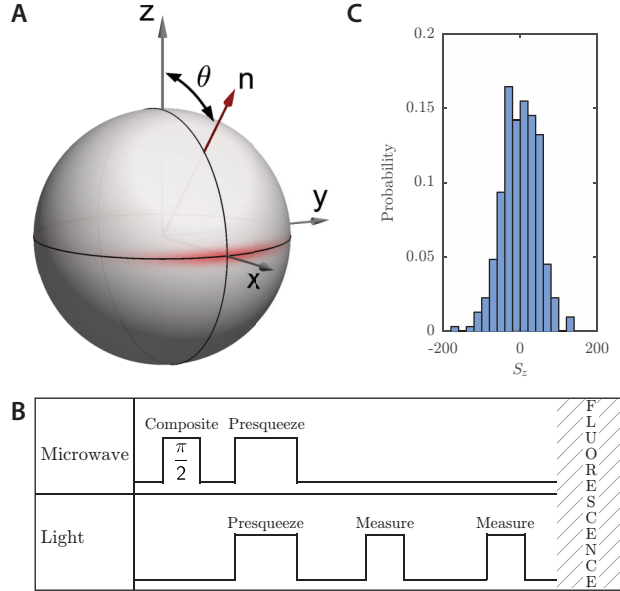


Figure 6.1: **A:** Illustration of a squeezed spin state. An example Wigner distribution of a 10 dB squeezed state with 30 atoms, polarized along the x -axis. Squeezing is along the z -direction, antisqueezing is along the y -direction. Also shown is the axis \mathbf{n} used to calculate the Bell witness in Equation 6.2. **B:** The sequence used for squeezing. The initial state preparation consists of a composite $\pi/2$ -pulse and a presqueezing procedure that squeezes the state in S_z such that the initial uncertainty is smaller than the cavity linewidth. The two QND measurements then follow before a final fluorescence measurement that measures the atom number. **C:** Histogram of the differences in S_z between the first and second measurements for 18.5(3) dB squeezed states of 6.5×10^5 atoms.

inhomogeneity due to the finite temperature of the atoms. We can therefore measure only the collective observable $S_{\mathbf{z}} = (1/Z) \sum_{i=1}^N (1 - \epsilon_i) j_z^{(i)}$ where Z is a normalization constant and ϵ_i is a small quantity parametrizing the reduction from unity in coupling of atom i . In our setup, we have measured a $\sim 5 \times 10^{-3}$ fractional variance in the atom-probe coupling (see [7] for details on the measurement of the atom-cavity coupling). This determines the deviation from symmetry in the measurement of the collective spin observables.

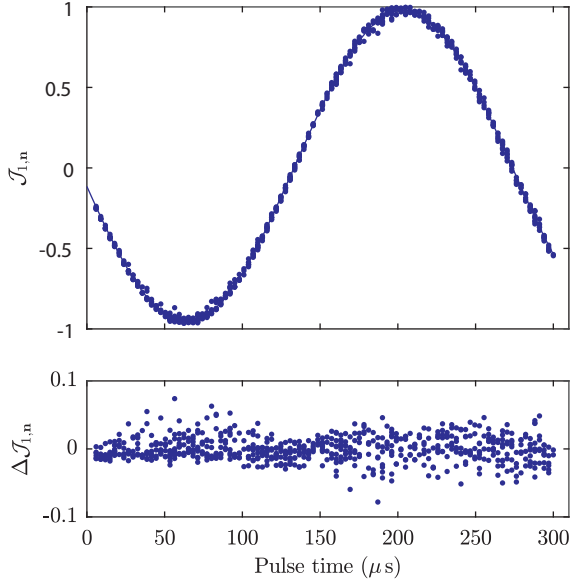


Figure 6.2: Rabi oscillations of squeezed states of 6.5×10^5 atoms. Upper panel: $\mathcal{J}_{1,n}$ as a function of the microwave pulse time. The fit is sinusoidal and is used to extract the angle for the witness function in Figure 6.3. The fit shows a contrast of $94.9(1)\%$. Lower panel: Residuals from subtracting the sine fit from the data points. The increased noise at the $\mathcal{J}_{1,n} \approx \pm 1$ points is due to antisqueezing. While fluorescence detection noise dominates at low pulse times, microwave amplitude noise takes over at larger times. Pulse times below $5\ \mu\text{s}$ were not achievable due to control system limitations.

6.3 Obtaining a Bell's witness with squeezed states

To generate squeezing in our apparatus, the atoms, initially prepared in the $|\downarrow\rangle$ state, are put in an equal superposition of the $|\uparrow\rangle$ and $|\downarrow\rangle$ states using a microwave drive (Figure 6.1B). Two QND measurements are then performed. The first measurement projects the collective spin state into one with reduced S_z uncertainty and increased S_y uncertainty. The second measurement verifies the squeezing by showing better correlation with the first measurement than allowed with unentangled states. Using this method we generate and characterize up to 20 dB of spin-squeezing by the Wineland criterion $\left[|\langle S_x \rangle| / (\sqrt{N} \Delta S_z)\right]^2$ [98]. Following the first measurement generating the squeezing, we can choose to drive Rabi oscillations using microwaves, amounting to a rotation of the collective spin state about the y -axis. This way, a subsequent

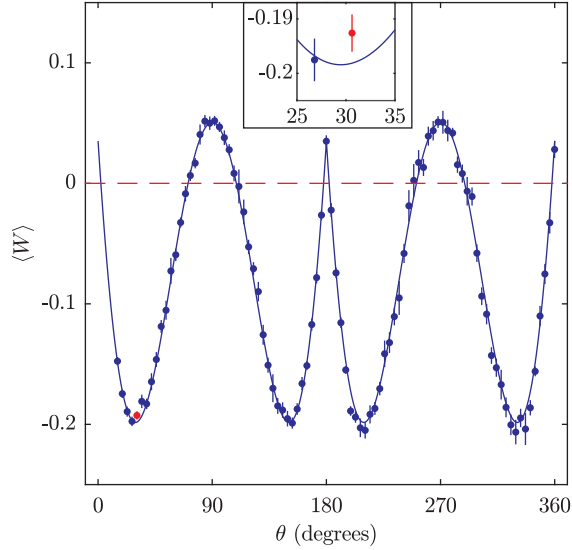


Figure 6.3: The data points show the Bell correlation witness $\langle W \rangle$ as a function of θ . The θ values are extracted from the fit in Figure 6.2. The error bars show the combined statistical error from the measured $\mathcal{J}_{1,\mathbf{n}}$ and the total error in the estimated $\mathcal{J}_{2,\mathbf{z}}$ value. Points below the dashed red line show violation of the inequality in Equation 6.2. The highest violation is from the point shown in red (also in inset) which is 56 standard deviations from the boundary. The solid blue line is calculated from the contrast of the fit to the Rabi fringe and the squeezing level. For a maximally squeezed state with 100% coherence, the minimum of the witness function would approach -0.25.

measurement of $S_{\mathbf{z}}$ allows us to determine $S_{\mathbf{n}}$ for any chosen angle θ between \mathbf{z} and \mathbf{n} . Since the squeezing is conditional on the outcome of the QND measurement, the inferred $\langle S_z \rangle$ for the prepared squeezed states is different in each realization. In order to show Bell correlations, we therefore choose an axis \mathbf{z}' at each realization such that the inferred $\langle S_{\mathbf{z}'} \rangle = 0$. The shot-to-shot variation in the chosen axis can be accounted for as noise in θ in Equation 6.2 (see § 6.5). For our parameters, this noise is small compared to the noise added by microwave rotation noise.

To relate the measured $S_{\mathbf{z}}$ observable to the properties of $J_{\mathbf{z}}$, we use a conservative procedure based on a model that was verified experimentally [7]. In this model ϵ_i depends on the specific position of the atom, and is randomized in each experimental run. The randomization of the position can be modeled as an additive noise that would appear in a measurement of the uniform observable $J_{\mathbf{z}}$. In our setup, this

additive noise is 16.8(7) dB below the CSS noise [7]. The error on this quantity is estimated from the additive noises found at three different atom numbers. According to this model, the squeezed state shown in Figure 6.1C, for example, which is 18.5 dB squeezed in S_z is guaranteed to be squeezed by at least 14.5 dB in J_z . For all Bell correlation data presented below, we calculate $\mathcal{J}_{2,z}$ according to this model. The error on this quantity is obtained by adding in quadrature the error in squeezing measurements and the error from the J_z estimation model.

While we measure the squeezing levels using the cavity probe, the Rabi oscillations needed to determine $\mathcal{J}_{1,n}$ are characterized using fluorescence imaging since the cavity does not have the dynamic range to make these measurements. The fluorescence imaging is done by first releasing the atoms from the optical lattice then pushing the atoms in the $|\uparrow\rangle$ state with a laser resonant with the $|F=2\rangle \rightarrow |F'=3\rangle$ transition. After a 1.2 ms time of flight the spatially separated states are imaged for 2 ms with resonance fluorescence. The signal from the pushed $|\uparrow\rangle$ atoms is 20% lower due to lower fluorescence beam intensity at their location. We performed a calibration to correct for this and applied it to the raw data. The error in the calibration procedure is insignificant compared to statistical errors for the presented data.

For a data set containing 15.0(7) dB inferred squeezing in J_z , we plot the observed Rabi oscillations in Figure 6.2. Combining the Rabi oscillation data with the squeezing level, we plot the witness function $\langle W \rangle$ in Figure 6.3. All data points below the dashed line indicate nonlocal correlations in the prepared squeezed states. The dominant contribution to the error bars is the noise of the microwave rotation which amounts to an uncertainty in the angle θ between \mathbf{z} and \mathbf{n} . This leads to increasing uncertainties with increasing microwave drive time.

6.4 Entanglement depth

In Figure 6.4 we plot our data with the Bell correlation boundary and entanglement depth boundaries on the $\mathcal{J}_{1,x}^2$ - $\mathcal{J}_{2,z}$ plane. Here, the $\mathcal{J}_{1,x}$ values of the states were determined by first performing the squeezing measurement, then making a microwave $\pi/2$ -rotation about the y-axis to turn J_x into J_z . The observable J_z was then measured

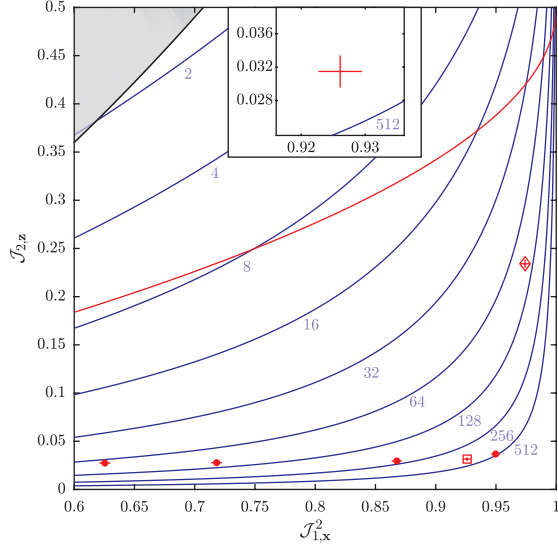


Figure 6.4: Entanglement depth and Bell correlation boundaries. Red line shows the Bell violation boundary according to Equation 6.3. Blue lines show the boundary for $k = 2^n$ entanglement depth for $n = 1 \dots 9$ (labeled below each line). The area below the black line contains entangled states according to the Wineland criterion for entanglement [81]. The data points, taken with 5×10^5 atoms and approximately 450 measurements each, have measurement strengths going from higher on the left to lower on the right. The error bars represent 68% confidence intervals. The open-square data point shows the most statistically significant demonstration of Bell correlations (the inset is a zoomed in version of this data point). The open-diamond data point shows the result from a data set of 3286 runs with unconditional squeezing.

using fluorescence imaging in 200 repetitions. For error estimation, the fluorescence calibration errors as well as the statistical errors are taken into account. In Figure 6.4, we also show a dataset that was unconditionally squeezed by 8.5 dB. These states were prepared using a similar method to that in [7]. The best conditionally squeezed data is 124 standard deviations from the boundary; the corresponding number for unconditional squeezing is 33 (see § 6.5 for details). The largest entanglement depth obtained in this analysis is approximately 500. However, using a more optimal entanglement depth criterion tailored for nonsymmetric probing [99], the best entanglement depth becomes 1590(130) (see § 6.7 for details).

In [95], it was shown that there exists non-Gaussian states that do not contain Bell correlations, but nevertheless violate the witness inequalities in Equation 6.2

and Equation 6.3. These non-Gaussian states can only be ruled out by performing of order N measurements. As there exists no known mechanism to generate these non-Gaussian states in our experiment, throughout we assumed that the generated squeezed states are Gaussian states.

In conclusion we have shown statistically significant Bell correlations in a large, thermal ensemble of ^{87}Rb atoms. Bell correlations measure nonlocality which can be used as a resource in quantum information. While the use of Bell correlations in many-body systems is still unknown, they have been used to generate random numbers in smaller systems [100]. Recent experiments have shown large spatial separation of quantum superpositions of atomic wavepackets [101]. Combining the ideas of spin squeezing with spatially separated superpositions, the Bell correlations discussed in this Letter could perhaps be used to test quantum mechanics in new ways.

6.5 Conditional squeezing and Bell witnesses

The Bell correlation witnesses stated in Equation 6.2 and Equation 6.3 require a measurement of the scaled second moment in one direction (chosen to be the **z** direction throughout the paper), a measurement of the collective spin operator in the direction **n** and knowledge of the angle between **n** and **z**. According to the witnesses, the reduction of the second moment $\langle J_z^2 \rangle$ below its CSS value is a necessary requirement to establishing Bell correlations. Experimentally we generate conditionally squeezed states, where, for the i th realization of the squeezing we infer a mean J_z value following the first measurement, and establish that the variance $\text{Var } J_z$ is reduced with a follow up measurement. However, from one realization to the next, the inferred mean J_z value of the prepared squeezed states vary as much as the CSS noise, since this is the width of J_z distribution prior to the first measurement. Thus, there is no reduction in the unconditional second moment of J_z . In principle, since the mean J_z value is inferred at each squeezing realization, a tuned follow-up rotation can bring this value to zero each time, and the unconditional second moment can be made equal to the conditionally squeezed variance. In practice however, this action is not necessary. Instead of choosing the **z** unit vector for Equation 6.2 at each realization, we can

choose a specific unit vector \mathbf{z}'_i that differs slightly at each realization. This unit vector should be chosen such that $\langle J_{z'_i} \rangle = 0$. Since the angle between \mathbf{z} and \mathbf{z}'_i is of order 10^{-3} rad, the squeezing level associated with this new direction remains essentially the same, i.e., $\text{Var } J_{z'_i} \sim \text{Var } J_z$. In this new picture, the variance and the second moment of $J_{z'_i}$ at each realization becomes identical by definition, allowing us to use the witness equations without alteration. However, the act of choosing a different axis each time contributes to the uncertainty in the angle θ between the two unit vectors we called \mathbf{n} and \mathbf{z} . To account for this we add $\delta\theta = 1/\sqrt{N}$ to our error budget for the data plotted in Figure 6.3 A similar argument can be applied to the violations shown according to Equation 6.2, but here $\delta\theta$ is much smaller than the uncertainty due to the microwave rotation to the top of the Bloch sphere to measure the coherence. No such considerations apply for the unconditionally squeezed case which was also shown in Figure 6.4, where we directly measure the squeezed second moment of J_z .

6.6 Modeling atom-cavity coupling inhomogeneities

We will here model the inhomogeneity of the atom-cavity coupling, which is the cause of the residual asymmetry in the preparation and characterization of the squeezed states. The treatment is used to give an upper bound on the symmetric, two-body correlators used to witness Bell correlations and to find the entanglement depth of these slightly nonsymmetric squeezed states. We will consider $s_v^{(i)} = \eta_i j_v^{(i)}$ the inhomogeneous spin operator on the i th atom in the v direction with coupling coefficient $\eta_i \in [0, 1]$. We can then define full collective inhomogeneous operators as

$$S_v = \frac{1}{Z} \sum_i s_v^{(i)} \quad (6.4)$$

where

$$Z = \frac{\sum_i \eta_i}{\sum_i \eta_i^2}. \quad (6.5)$$

Z is chosen such that $\text{Var } S_z / \langle S_x \rangle_{\text{CSS}} = 1/2$.

We now seek to estimate the coupling coefficients in the cavity experiment conducted here. First we consider the density of atoms as a function of transverse distance from the center of the optical lattice,

$$\rho(x, y) \propto \exp\left(-\frac{x^2 + y^2}{2\sigma_r^2}\right) \quad (6.6)$$

where $\sigma_r = 15.2(3)\text{ }\mu\text{m}$ is the Gaussian width of the density distribution of the atoms in the trap calculated from temperature measurements, and x and y are the transverse coordinates centered at the lattice axis. Since the trapping and probing of the atoms are done with the TEM00 modes of the cavity, the center of the cloud and the center of the probe beam are well aligned. The probe has a waist of $w_{780} = 111\text{ }\mu\text{m}$ and its intensity governs the cavity coupling coefficients for atoms. We can now consider $\eta_i = 1 - \epsilon_i$ as the coupling coefficient for the i th atom. For $x = y = 0$, $\eta_i = 1$ and we therefore have maximal coupling. Utilizing Equation 6.6, we then have that for the Gaussian TEM00 mode of the cavity,

$$\eta(x, y) = \exp\left(\frac{-2(x^2 + y^2)}{w_{780}^2}\right). \quad (6.7)$$

The magnitude of the inhomogeneity for our experimental parameters is in fact quite small. The variance of η over the ensemble of atoms evaluates to $\sim 5 \times 10^{-3}$. The model was verified experimentally in [7], where the inhomogeneity calculated from temperature measurements was found to numerically agree with the values inferred from cavity measurements.

6.7 Calculating entanglement depth with nonsymmetric coupling

As shown in [99, 102], we can put tighter bounds on the entanglement depth of our slightly nonsymmetric states. The main message from this section is that for the level of inhomogeneities we are dealing with, the full non-symmetric calculation and the symmetric calculation ignoring the inhomogeneities in our system virtually give

the same entanglement depths of up to ~ 1600 particles. The predictions of the full calculation is in fact $\sim 1\%$ lower.

In order to generate entanglement boundaries for our particular nonsymmetric probing, we first generate random positions distributed according to Equation 6.6 and calculate individual coupling coefficients from Equation 6.7. Following the procedure in [99], we consider n ensembles of k particles, where each ensemble indexed by i has the same coupling coefficient η_i . It is shown in [99] that ensembles of k entangled atoms with identical coupling coefficients minimize the variance of the ensemble thus this is a suitable assumption to place entanglement boundaries. We then have the following two equations for the normalized coherence

$$\frac{\langle S_x \rangle}{\langle S_x \rangle_{\text{CSS}}} = \frac{1}{\langle S_x \rangle_{\text{CSS}}} \sum_{i=1}^n \langle S_x^{(i)} \rangle_{\text{CSS}} \frac{\langle S_x^{(i)} \rangle}{\langle S_x^{(i)} \rangle_{\text{CSS}}} \quad (6.8)$$

and variance

$$\frac{(\Delta S_z)^2}{(\Delta S_z)_{\text{CSS}}^2} = \frac{1}{(\Delta S_z)_{\text{CSS}}^2} \sum_{i=1}^n (\Delta S_z^{(i)})_{\text{CSS}}^2 \frac{(\Delta S_z^{(i)})^2}{(\Delta S_z^{(i)})_{\text{CSS}}^2} \quad (6.9)$$

of the collective state. Here, for an inhomogeneously coupled ensemble we have defined

$$\langle S_x \rangle_{\text{CSS}} = \frac{1}{Z} \sum_i \frac{\eta_i}{2} \quad (6.10)$$

$$(\Delta S_x)_{\text{CSS}}^2 = \frac{1}{Z^2} \sum_i \frac{\eta_i^2}{4} \quad (6.11)$$

Since each ensemble of k atoms has the same coupling coefficient η_i , we can place entanglement depth boundaries based on previous work in uniformly coupled ensembles [81, 82]. We can now minimize Γ defined as follows

$$\Gamma \left(\{(\Delta S_z^{(i)})^2\}, \{\langle S_x^{(i)} \rangle\}, \mu \right) = \sum_{i=1}^n \left[\frac{k\eta_i^2}{4} \frac{(\Delta S_z^{(i)})^2}{(\Delta S_z^{(i)})_{\text{CSS}}^2} - \mu \frac{\langle S_x \rangle}{\langle S_x \rangle_{\text{CSS}}} \right] \quad (6.12)$$

where μ is a Lagrange multiplier to enforce the constraint of coherence and Γ is the variance of the full collective state, subject to the constraint. From [81], we also have that

$$(\Delta S_z)^2 \geq \frac{k}{2} F_{k/2} \left(\frac{\langle S_x \rangle}{k/2} \right) \quad (6.13)$$

for each ensemble of k atoms. We use the numerical method described in [82] to find this upper bound on $(\Delta J_z)^2$ for each ensemble of k atoms. We minimize Γ with respect to $\langle S_x \rangle$ for each individual ensemble using the numerically calculated entanglement bounds. We insert the minimized variance and the corresponding coherence into Equation 6.8 and Equation 6.9 to find the bounds on entanglement for our inhomogeneity. Now, we sample coupling strengths calculated from randomly generated positions within the distribution in Equation 6.7, and use the bounds on the individual ensembles along with the coupling coefficients to produce an overall bound from Equation 6.9 and Equation 6.8. To produce conservative bounds we use $\sigma_r = 20\mu\text{m}$. We use $\sqrt{\langle J_x^2 + J_y^2 \rangle}$ in place of $\langle S_x \rangle$ paralleling the procedures outlined in [82] and [103] since it places a tighter bound on the entanglement depth of states with large antisqueezing. We then arrive at the bounds shown in Figure 6.5. The validity of this procedure is shown in the following two sections S2.1 and S2.2.

The largest entanglement depth obtained with this method yields 1590(130) particles. We have also carried out the calculations where we pretended we were measuring completely symmetric observables with our cavity and employed an analysis that does not take into account inhomogeneities following [82]. The resulting entanglement depth for the corresponding data set was 1605(30), implying that the boundaries quantifying the quantum correlations are in fact smooth functions of the inhomogeneity.

6.7.1 Use of $\sqrt{S_x^2 + S_y^2}$ for the calculation of entanglement depth

In [82] and [103] it was shown that for the calculation of entanglement depth in symmetric states, $\langle J_x^2 + J_y^2 \rangle$ can be used in place of $\langle J_x \rangle$ when $N \gg k$. Here, we follow the same general procedure to show that this also works in the nonsymmetric case.

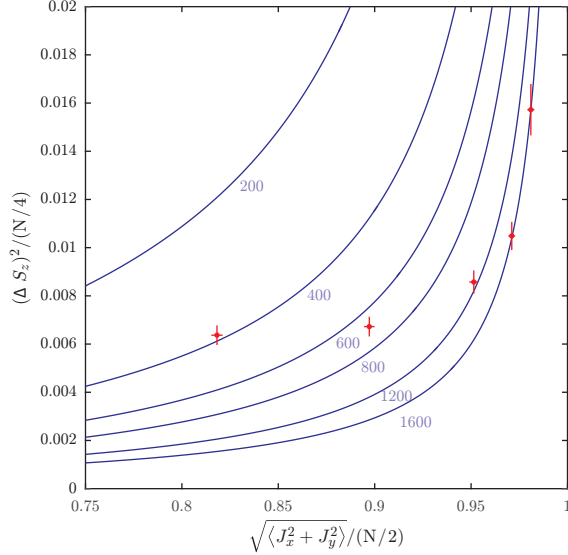


Figure 6.5: The figure shows the entanglement depth bounds calculated by the procedure described in § 6.7. The lowest measurement strength point here has the largest entanglement depth of 1590(130). Error bars show 68% confidence intervals.

We will consider groups of k_i particles and use the inhomogeneous operators. Using the standard definition of the variances in the x and y direction and the fact that the variance of the entire ensemble is the sum of the variances of the subensembles, we obtain

$$\begin{aligned} \langle (\Delta S_x)^2 \rangle + \langle (\Delta S_y)^2 \rangle &= \frac{1}{Z^2} \sum_i (\Delta s_x^{(i)})^2 + (\Delta s_y^{(i)})^2 \\ &\leq \frac{1}{Z^2} \sum_i \frac{k_i \eta_i^2}{2} \left(\frac{k_i}{2} + 1 \right) - \langle (s_z^{(i)})^2 \rangle - \langle s_x^{(i)} \rangle^2 - \langle s_y^{(i)} \rangle^2. \end{aligned} \quad (6.14)$$

The inequality holds as

$$\begin{aligned}
& (\Delta s_x^{(i)})^2 + (\Delta s_y^{(i)})^2 \\
&= \eta_i^2 \left[(\Delta j_x^{(i)})^2 + (\Delta j_y^{(i)})^2 \right] \\
&\leq \eta_i^2 \left[\frac{k_i}{2} \left(\frac{k_i}{2} + 1 \right) - \langle (j_z^{(i)})^2 \rangle - \langle j_x^{(i)} \rangle^2 - \langle j_y^{(i)} \rangle^2 \right]
\end{aligned} \tag{6.15}$$

Since $\langle (j_z^{(i)})^2 \rangle \geq 0$ we neglect it. We now expand the variances and move the squared means to the RHS and obtain

$$\langle S_x^2 + S_y^2 \rangle \leq \langle S_x \rangle^2 + \langle S_y \rangle^2 + \frac{1}{Z^2} \sum_i \frac{k_i \eta_i^2}{2} \left[\left(\frac{k_i}{2} + 1 \right) - \frac{k_i}{2} \frac{\langle j_x^{(i)} \rangle^2 + \langle j_y^{(i)} \rangle^2}{k_i^2/4} \right] \tag{6.16}$$

We now define $\zeta = (1/Z^2) \sum_i k_i \eta_i^2$, then set the term inside the square bracket to its maximum, where $k_i = k$ for all i .

$$\langle S_x^2 + S_y^2 \rangle \leq \langle S_x \rangle^2 + \langle S_y \rangle^2 + \frac{\zeta}{2} + \frac{1}{Z^2} \sum_i \frac{k_i \eta_i^2}{2} \left[\frac{k}{2} \left(1 - \frac{\langle j_x^{(i)} \rangle^2 + \langle j_y^{(i)} \rangle^2}{k^2/4} \right) \right] \tag{6.17}$$

We can now use Jensen's inequality to show that

$$-\sum_i k_i \left(\frac{\langle s_v^{(i)} \rangle}{k_i} \right)^2 \leq -\frac{1}{N} \left(\sum_i k_i \frac{\langle s_v^{(i)} \rangle}{k_i} \right)^2 = -\frac{Z^2}{N} \langle S_v \rangle^2 \tag{6.18}$$

for $v = x, y, z$, where we used that $\sum_i k_i = N$. Applying this inequality on Equation 6.17, we obtain

$$\langle S_x^2 + S_y^2 \rangle - \frac{\zeta}{2} \left(\frac{k}{2} + 1 \right) \leq \left(1 - \frac{k}{N} \right) (\langle S_x \rangle^2 + \langle S_y \rangle^2). \tag{6.19}$$

Now we choose to consider states polarized in the x -direction and, without loss of

generality, set $\langle S_y \rangle = 0$. If we then divide by $(1 - k/N)$ and take the square root, we obtain

$$\left\{ \frac{1}{1 - k/N} \left[\langle S_x^2 + S_y^2 \rangle - \frac{\zeta}{2} \left(\frac{k}{2} + 1 \right) \right] \right\}^{1/2} \leq \langle S_x \rangle \quad (6.20)$$

For the inhomogeneity of our experiment, $\zeta \sim 0.995N$. As $\langle S_x^2 + S_y^2 \rangle \sim \zeta^2$ is large compared to $(\zeta/2)(k/2 + 1)$ we neglect $(\zeta/2)(k/2 + 1)$ and take $(1 - k/N) \sim 1$. We can then use $\sqrt{\langle S_x^2 + S_y^2 \rangle}$ in place of $\langle S_x \rangle$ to calculate our entanglement depth.

6.7.2 Symmetric and nonsymmetric coherence

Since the coherence measurements are done with fluorescence imaging, we in fact measure the coherence associated with the symmetric collective observables. In this subsection we will show that these coherence measurements give a lower bound on the coherence associated with the nonsymmetric collective observables which go into the entanglement depth calculations in the nonsymmetric case.

Using a similar method to that shown in Section S2 we can model our decoherence. We choose states polarized in the x -direction. Consider the Heisenberg picture operators for J_x , J_y , S_x and S_y :

$$J_x = \sum_i (\cos \theta_n j_x^{(n)} + \sin \theta_n j_y^{(n)}) \quad (6.21)$$

$$J_y = \sum_i (\cos \theta_n j_x^{(n)} + \sin \theta_n j_y^{(n)}) \quad (6.22)$$

$$S_x = \frac{1}{Z} \sum_n \eta_i (\cos \theta_n j_x^{(n)} + \sin \theta_n j_y^{(n)}) \quad (6.23)$$

$$S_y = \frac{1}{Z} \sum_n \eta_i (\cos \theta_n j_x^{(n)} + \sin \theta_n j_y^{(n)}) \quad (6.24)$$

Here θ_n parametrizes the amount of decoherence, essentially modeling the decoherence as a mixing in of the orthogonal operator $j_y^{(n)}$. The origin of this is the inhomogeneous ac-Stark shifts from the probe beam. Thus the model adopts Equation 6.7 to define

a $\theta_n = \beta r_n^2$ where $r_n = (x_n^2 + y_n^2)^{1/2}$ is the n th particle's distance from the center of the probe beam. Using this model and inserting positions sampled from the same distribution used earlier, we calculated numerically that

$$\frac{\sqrt{J_x^2 + J_y^2}}{N/2} \leq \frac{\sqrt{S_x^2 + S_y^2}}{(1/Z) \sum_i \eta_i / 2}. \quad (6.25)$$

We are therefore justified in using the LHS of Equation 6.25 as a lower bound on the coherence for entanglement depth calculations in the nonsymmetric case.

6.8 Standard Error Calculations

In order to characterize the statistical significance of our results, we compute the minimum number of standard deviations the point is from the Bell violation boundary. This amounts to minimizing r , defined as

$$r = \left[\left(\frac{\mathcal{J}_{1,\mathbf{x}} - x_{\text{bell}}}{\Delta \mathcal{J}_{1,\mathbf{x}}} \right)^2 + \left(\frac{\mathcal{J}_{2,\mathbf{z}} - y_{\text{bell}}}{\Delta \mathcal{J}_{2,\mathbf{z}}} \right)^2 \right]^{1/2} \quad (6.26)$$

where x_{bell} and y_{bell} describe the line that forms the boundary and ΔX denotes the empirically determined standard deviation of the quantity X . r is then the number of standard deviations from the point on the boundary described by $(x_{\text{bell}}, y_{\text{bell}})$. We use Eq. 3 from the main text to describe the boundary such that

$$y_{\text{bell}} = \frac{1}{2} \left(1 - \sqrt{1 - x_{\text{bell}}^2} \right). \quad (6.27)$$

The variance of the empirical second moment for the unconditional squeezing was computed using the formula

$$\text{Var}(\langle J_z^2 \rangle) = \frac{2(\Delta J_z)^4 + 4 \langle J_z \rangle^2 (\Delta J_z)^2}{n} \quad (6.28)$$

whereas the variance of the empirical second moment for the conditional squeezing was computed using the usual chi-squared distribution for the variance of a sample variance. The derivation of Equation 6.28 can be found in § A.3

Appendix A

Uncertainty Calculations

In this appendix I look at the statistical calculations of the error bars in our experiments. In §A.1 I will show how to obtain a confidence interval of $Var(J_z)$ from first principles. In § A.2 I will discuss how to obtain an estimate of a “pooled variance”, i.e. how to estimate $Var(J_z)$ after having done several runs and calculated the $Var(J_z)$ for each run. Finally I will end with how to derive the variance of the empirical second moment which was stated in Equation 6.28.

A.1 Confidence interval on the variance of a normally distributed variable

The objective of this section is to derive a confidence interval for a calculated value of $Var(J_z)$ given that a set of independent and identical measurements were performed to obtain several values of J_z for a given state. We assume that the outcome of a measurement of J_z is a normally distributed random variable X that has a true mean μ and a true variance σ^2 i.e. $X \sim N(\mu, \sigma)$. I will start off by showing that the square of a standard normal random variable has a χ^2 -distribution. Then I will show that the sum of χ^2 -distributed variables is also a χ^2 -distributed variable. Then using the previous 2 derivations, I will demonstrate that the empirical variance of a normally distributed variable has a χ^2 -distribution.

A.1.1 The square of a standard normal random variable

We start off with a random variable $Z \sim N(0, 1)$. Starting the cumulative distribution function $F(x) = \Pr(Z^2 \leq x)$ and following [104] we obtain

$$\begin{aligned} F(x) &= \Pr(-\sqrt{x} \leq Z \leq \sqrt{x}) \\ &= \int_{-\sqrt{x}}^{\sqrt{x}} \frac{1}{\sqrt{2\pi}} e^{-z^2/2} dz \\ &= 2 \int_0^{\sqrt{x}} \frac{1}{\sqrt{2\pi}} e^{-z^2/2} dz \\ &= 2 \int_0^{\sqrt{x}} \frac{1}{\sqrt{2\pi}} e^{-y/2} \frac{1}{2\sqrt{y}} dy \text{ (using } y = z^2) \\ f(x) &= \frac{dF(x)}{dx} = \frac{1}{\Gamma(\frac{1}{2}) \sqrt{2}} e^{-x/2} \frac{1}{\sqrt{x}} \end{aligned} \tag{A.1}$$

where the last line of Equation A.1 is the probability density function of a χ_1^2 -distributed variable (i.e. a variable with a χ^2 -distribution with 1 degree of freedom).

A.1.2 Sum of χ^2 -distributed variables

Following [104] we take the sum of N χ^2 -distributed variables X_i that each have a different degree of freedom r_i i.e. $X_i \sim \chi_{r_i}^2$ and proceed with

$$\begin{aligned} Y &= \sum_i X_i \\ M_Y(t) &= \prod_{i=1}^N (1 - 2t)^{\frac{-r_i}{2}} \\ &= (1 - 2t)^{\frac{\sum_{i=1}^N r_i}{2}} \\ \Rightarrow Y &\sim \chi_{\sum_{i=1}^N r_i}^2 \end{aligned} \tag{A.2}$$

where $M_Y(t)$ is defined as $E[e^{Yt}]$ and is known as the moment generating function for Y . This is because taking the n th derivative of this expression will give you the n th moment of Y (this can be seen by expanding e^{Yt} and taking its expectation). If

two random variables have the same moment generating function then they must have the same probability distribution [105].

A.1.3 The variance of the empirical variance

In this subsection we will use the results from § A.1.1 and § A.1.2 and following the same method in [104] we will derive the variance on the measured $Var(X)$ given that we draw N identical and independent X_i 's from a normal distribution $N(\mu, \sigma^2)$.

$$\begin{aligned}
W &\equiv \sum_{i=1}^N \left(\frac{X_i - \mu}{\sigma} \right)^2 \sim \chi_N^2 \text{ (from Equation A.2)} \\
&= \sum_{i=1}^N \left(\frac{(X_i - \bar{X}) + (\bar{X} - \mu)}{\sigma} \right)^2 \\
&= \sum_{i=1}^N \left(\frac{(X_i - \bar{X})}{\sigma} \right)^2 + \sum_{i=1}^N \left(\frac{(\bar{X} - \mu)}{\sigma} \right)^2 + 2 \frac{(\bar{X} - \mu)}{\sigma} \sum_{i=1}^N (X_i - \bar{X}) \\
&= \frac{\sum_{i=1}^N (X_i - \bar{X})^2}{\sigma^2} + \frac{N(\bar{X} - \mu)^2}{\sigma^2} \\
&= \frac{(N-1)s^2}{\sigma^2} + \frac{N(\bar{X} - \mu)^2}{\sigma^2}
\end{aligned} \tag{A.3}$$

(A.4)

where \bar{X} is the empirical mean of X i.e. $\frac{1}{N} \sum_{i=1}^N X_i$ and s is the unbiased sample variance of the X_i 's i.e. $\frac{1}{N-1} \sum_{i=1}^N (X_i - \bar{X})^2$. According to the central limit theorem [106–108] we know that $\frac{\sqrt{N}(\bar{X} - \mu)}{\sigma} \sim N(0, 1)$. The second term on the RHS of Equation A.3 is the square of this, so it must be χ_1^2 -distributed (Equation A.1). And since the LHS of Equation A.3 is χ_N^2 -distributed, the first term on the RHS of Equation A.3 must be χ_{N-1}^2 -distributed (Equation A.2). So to obtain a confidence interval for a

confidence interval for the true variance σ^2 of $1 - \alpha$ (e.g. $1 - \alpha = 68\%$) we have

$$\begin{aligned} \chi_{N-1,1-\alpha/2}^2 &\leq \frac{(N-1)s^2}{\sigma^2} \leq \chi_{N-1,\alpha/2}^2 \\ \frac{(N-1)s^2}{\chi_{N-1,\alpha/2}^2} &\leq \sigma^2 \leq \frac{(N-1)s^2}{\chi_{N-1,1-\alpha/2}^2} \end{aligned} \quad (\text{A.5})$$

(A.6)

It is worth noticing that that in general, since χ^2 distributions are not symmetric, the confidence intervals of σ^2 tend to be asymmetric about s^2 . It is useful to note that the χ^2 distribution is a special case of the Γ distribution. More explicitly

$$\begin{aligned} \frac{(N-1)s^2}{\sigma^2} &\sim \chi_{N-1}^2 \equiv \Gamma\left(\frac{N-1}{2}, \frac{1}{2}\right) \\ \Rightarrow s^2 &\sim \Gamma\left(\frac{N-1}{2}, \frac{\sigma^2}{2(N-1)}\right) \end{aligned} \quad (\text{A.7})$$

(A.8)

where the $\frac{N-1}{2}$ is the shape parameter and $\frac{1}{2}$ is the rate parameter [109]. The $\Gamma(k, \beta)$ distribution has a variance of $\frac{k}{\beta^2}$ and has the property that if $X \sim \Gamma(k, \beta)$ then $cX \sim \Gamma(k, \frac{\beta}{c})$ where c is a constant.

A.2 The pooled variance

Now I will discuss how to estimate s^2 after having done several runs and calculated the s^2 for each run. This is useful in the context of our experiment because sometimes we take data throughout the course of the day during which the mean of our J_z values could shift (and hence we cannot treat all the measurements as coming from the same dataset). This “average” of variances is known as a pooled variance.

If we define $s_i^2 = \text{Var}(\vec{X}_i)$ where \vec{X}_i is a set of data collected from the i th run. We now want to estimate the best weighted average variance of all the data points after N runs i.e. the a_i 's that will give us the smallest variance in $\sum_{i=1}^N a_i s_i^2$. We can do this by minimizing the variance of this function along with the constraint that

$\sum_{i=1}^N a_i = 1$. We define a Lagrangian

$$\mathcal{L} = \text{Var} \left(\sum_{i=1}^N a_i s_i^2 \right) - \lambda \left(\sum_{i=1}^N a_i - 1 \right) \quad (\text{A.9})$$

where λ is the Lagrange multiplier. Taking the derivative of this and setting it to zero we obtain

$$\begin{aligned} \frac{\partial \mathcal{L}}{\partial a_j} &= a_j^2 \text{Var}(s_j^2) - \lambda a_j = 0 \\ a_j &= \frac{\lambda}{\text{Var}(s_j^2)} \\ \sum_{i=1}^N a_i &= 1 \\ \Rightarrow \sum_{i=1}^N \frac{\lambda}{\text{Var}(s_i^2)} &= 1 \\ \lambda &= \sum_{i=1}^N \text{Var}(s_i^2) \\ \Rightarrow a_j &= \frac{\sum_{i=1}^N \text{Var}(s_i^2)}{\text{Var}(s_j^2)} \end{aligned} \quad (\text{A.10})$$

Looking at the variance of a single s_i^2 we obtain

$$\begin{aligned} \text{Var}(s_i^2) &= \text{Var} \left(\frac{(n_i - 1)s_i^2}{\sigma^2} \times \frac{\sigma^2}{n_i - 1} \right) \\ &= \text{Var} \left(\frac{(n_i - 1)s_i^2}{\sigma^2} \right) \times \frac{\sigma^4}{(n_i - 1)^2} \\ &= 2(n_i - 1) \times \frac{\sigma^4}{(n_i - 1)^2} \\ &= \frac{2\sigma^4}{n_i - 1} \end{aligned} \quad (\text{A.11})$$

where n_i is the number of data points used when calculating s_i^2 and $\text{Var}(\chi_k^2) = 2k$ [109]. Using Equation A.11 in Equation A.10 we obtain

$$\begin{aligned}
a_j &= \frac{\sum_{i=1}^N \frac{2\sigma^4}{n_i - 1}}{\frac{2\sigma^4}{n_j - 1}} \\
&= \frac{n_j - 1}{\sum_{i=1}^N n_i - 1}
\end{aligned} \tag{A.12}$$

Taking the values of the weights a_i from Equation A.12 we can now see the minimum pooled variance is

$$\sum_{i=1}^N a_i \text{Var}(s_i^2) = \sum_{i=1}^N \frac{(n_i - 1) \text{Var}(s_i^2)}{\sum_{j=1}^N (n_j - 1)} \tag{A.13}$$

A.3 Variance of the empirical second moment

In this section I derive the expression for the variance of the empirical second moment of the set of J_z measurements i.e. the variance of \bar{J}_z^2 . The question we are trying to answer is if we take many J_z measurements, square each measurement and take the mean of all the squares, what is my uncertainty in this mean?

The result below is actually a general one, and to be more formal I am deriving the variance of the second moment of a set of random variables that I am calling $J_{z,i}$ which are drawn independently and identically from a normal distribution with mean μ and variance σ^2 . First I will define some terms:

$J_{z,i}$ - a single J_z measurement

n - total number of measurements of J_z

\bar{J}_z - empirical mean of all the J_z measurements (the same as $\langle J_z \rangle$) defined as $\frac{1}{n} \sum_{i=1}^n J_{z,i}$

\bar{J}_z^2 - the empirical second moment of all the J_z measurements (same as $\langle J_z^2 \rangle$) defined as $\frac{1}{n} \sum_{i=1}^n J_{z,i}^2$

$(\bar{J}_z)^2$ - the square of the empirical mean of all J_z measurements (same as $\langle J_z \rangle^2$)

$\text{Var}(J_z)$ - the sample variance of all the J_z measurements, i.e. $\langle J_z^2 \rangle - \langle J_z \rangle^2$

μ - the true mean of J_z

σ^2 - the true variance of J_z

Our objective is to find the variance of the second moment i.e. $\text{Var}(\bar{J}_z^2)$. The derivation is as follows:

$$\begin{aligned}
 \text{Var}(\bar{J}_z^2) &= E[(\bar{J}_z^2)^2] - [E(\bar{J}_z^2)]^2 \\
 &= E\left[\left(\frac{1}{n} \sum_{i=1}^n J_{z,i}^2\right)^2\right] - \left[E\left(\frac{1}{n} \sum_{i=1}^n J_{z,i}^2\right)\right]^2 \\
 &= \frac{1}{n^2} E\left[\left(\sum_{i=1}^n J_{z,i}^2\right)^2\right] - \frac{1}{n^2} \left[E\left(\sum_{i=1}^n J_{z,i}^2\right)\right]^2
 \end{aligned} \tag{A.14}$$

The equation above (i.e. Equation A.14) has two terms on the right hand side. Let's look at these two terms separately. First term:

$$\begin{aligned}
 E\left[\left(\sum_{i=1}^n J_{z,i}^2\right)^2\right] &= E\left(\sum_{i=1}^n J_{z,i}^4 + \sum_{i=1}^n \sum_{j \neq i} J_{z,i}^2 J_{z,j}^2\right) \\
 &= \sum_{i=1}^n E[J_{z,i}^4] + \sum_{i=1}^n \sum_{j \neq i} E[J_{z,i}^2] E[J_{z,j}^2] \\
 &= n(\mu^4 + 6\mu^2\sigma^2 + 3\sigma^4) + n(n-1)(\sigma^2 + \mu^2)^2 \\
 &= n(\mu^4 + 6\mu^2\sigma^2 + 3\sigma^4) + (n^2 - n)(\sigma^4 + 2\mu^2\sigma^2 + \mu^4) \\
 &= n^2(\mu^4 + 2\mu^2\sigma^2 + \sigma^4) + n(4\mu^2\sigma^2 + 2\sigma^4)
 \end{aligned} \tag{A.15}$$

Second term:

$$\begin{aligned}
\left[E \left(\sum_{i=1}^n J_{z,i}^2 \right) \right]^2 &= \left[\sum_{i=1}^n E(J_{z,i}^2) \right]^2 \\
&= n^2 (E[J_z^2])^2 \\
&= n^2 (\sigma^2 + \mu^2)^2 \\
&= n^2 (\sigma^4 + 2\mu^2\sigma^2 + \mu^4)
\end{aligned} \tag{A.16}$$

And now we take the two terms we calculated in Equations A.15 and A.16 and plug them into Equation A.14 to obtain:

$$\begin{aligned}
Var(\bar{J}_z^2) &= \frac{1}{n^2} n(\mu^4 + 2\mu^2\sigma^2 + \sigma^4) + n(4\mu^2\sigma^2 + 2\sigma^4) - \frac{1}{n^2} n^2(\sigma^4 + 2\mu^2\sigma^2 + \mu^4) \\
&= \frac{2\sigma^4 + 4\sigma^2\mu^2}{n}
\end{aligned}$$

I would like to acknowledge Prof. Jaya Krishnakumar for her help and insight she contributed to the derivation above.

Appendix B

Quantum Fisher Information

The original derivation of the quantum Cramér-Rao bound was published by C.W. Helstrom in 1967 [110]. Although brilliant, it is very terse, and I thought it would be a useful exercise to re-derive the bound by following his original derivation. This re-derivation is what is presented in this chapter. Section 1 begins with some definitions that I will use throughout the derivation. Section 2 just lists properties of mathematical objects which I will be using throughout the main derivation i.e. Section 3. Feel free to skip Section 2 and come back to it whenever you do not understand a step in Section 3. The equations/properties used for each step in the main derivation are clearly marked so it's easy to exactly which equations were used from Section 2 at a given step.

B.1 Definitions

θ - the parameter of interest (that we want to estimate).

$\hat{\theta}$ - estimate of parameter θ .

$\rho(\theta) = \rho$ - density operator of a quantum system (which depends on θ).

$E(y)$ - expectation value of a variable y .

X - measurement operator associated with the parameter θ (i.e. it is Hermitian). A very simple example would be, taking a pure state $|\theta\rangle$ with parameter θ , this operator would be defined as $X|\theta\rangle = \theta|\theta\rangle$.

We can now write down the following definitions

$$\begin{aligned} E(\hat{\theta}) &= \text{Tr}(X\rho) \\ E(\hat{\theta}^2) &= \text{Tr}(X^2\rho) \end{aligned} \quad (\text{E1})$$

B.2 Properties of Mathematical Objects

B.2.1 Density operator properties

$$\text{Tr}\rho(\theta) = \text{Tr}\rho = 1 \quad (\text{D1})$$

$$\frac{\partial}{\partial\theta}\text{Tr}(\rho) = \text{Tr}(\partial\rho/\partial\theta) = 0, \quad (\text{D2})$$

$$\text{by definition } \rho = \rho^\dagger \Rightarrow \partial\rho/\partial\theta = (\partial\rho/\partial\theta)^\dagger, \quad (\text{D3})$$

B.2.2 Trace properties

$$\text{Tr}(ABC) = \text{Tr}(CAB) = \text{Tr}(BCA) \quad (\text{T1})$$

$$\alpha\text{Tr}(A) = \text{Tr}(\alpha A) \quad (\text{T2})$$

$$\text{Tr}(A) + \text{Tr}(B) = \text{Tr}(A + B) \quad (\text{T3})$$

B.2.3 Hermitian Conjugate Properties

$$(A + B)^\dagger = A^\dagger + B^\dagger \quad (\text{HC1})$$

$$(AB)^\dagger = B^\dagger A^\dagger \quad (\text{HC2})$$

B.2.4 Cauchy Schwarz Inequality for complex matrices.

The Cauchy Schwarz Inequality states that

$$\langle x, y \rangle \leq \sqrt{\langle x, x \rangle \langle y, y \rangle} \quad (\text{CS1})$$

where \langle , \rangle represents the inner product.

We can define the inner product for square complex matrices as

$$\langle A, B \rangle = \text{Tr}(AB^\dagger) \quad (\text{CS2})$$

since this satisfies all the requirements for inner products.

Therefore we can rewrite the Cauchy Schwarz Inequality as

$$\text{Tr}(AB^\dagger) \leq \sqrt{\text{Tr}(AA^\dagger)\text{Tr}(BB^\dagger)} \quad (\text{CS3})$$

B.3 Calculating the Quantum Cramér-Rao Bound

First, let take the bias of $\hat{\theta}$, defined as $b(\hat{\theta}) \equiv E(\hat{\theta}) - \theta$, which gives us

$$\begin{aligned} b(\hat{\theta}) &\equiv E(\hat{\theta}) - \theta = \text{Tr}(X\rho) - \theta\text{Tr}(\rho) && \text{Using Equations E1 and D1} \\ &= \text{Tr}(\rho X) - \text{Tr}(\rho\theta) && \text{Using Equations T2 and T1} \\ &= \text{Tr}(\rho(X - \theta)) && \text{Using Equation T3} \end{aligned} \quad (1)$$

The variance of the estimator, defined as $E(\hat{\theta} - \theta)^2$, can be written as

$$\begin{aligned}
E(\hat{\theta} - \theta)^2 &= E(\hat{\theta}^2 - 2\theta\hat{\theta} + \theta^2) \\
&= E(\hat{\theta}^2) - E(2\theta\hat{\theta}) + E(\theta^2) \\
&= E(\hat{\theta}^2) - 2\theta E(\hat{\theta}) + \theta^2 && \text{Using } E(\theta) = \theta \\
&= \text{Tr}(X^2\rho) - 2\theta\text{Tr}(X\rho) + \theta^2\text{Tr}(\rho) && \text{Using Equations E1 and D1} \\
&= \text{Tr}(X^2\rho - 2\theta\rho + \theta^2\rho) && \text{Using Equations T3 and T2} \\
&= \text{Tr}(\rho(X - \theta)^2) && \text{Using Equation T1} \quad (2)
\end{aligned}$$

We shall now proceed to find the lower bound on this equation.

Rearranging Equation 1 and taking the derivative with respect to θ we obtain

$$\begin{aligned}
1 + b'(\hat{\theta}) &= E'(\hat{\theta}) \\
&= \frac{\partial}{\partial\theta}\text{Tr}(X\rho) \\
&= \text{Tr}(\partial(X\rho)/\partial\theta) \\
&= \text{Tr}(X\partial\rho/\partial\theta) && X \text{ is independent of } \theta \\
&= \text{Tr}(X\partial\rho/\partial\theta) - \theta\text{Tr}(\partial\rho/\partial\theta) && \text{Using Equation D2} \\
&= \text{Tr}(X\partial\rho/\partial\theta) - \text{Tr}(\theta\partial\rho/\partial\theta) && \text{Using Equation T2} \\
&= \text{Tr}(X\partial\rho/\partial\theta - \theta\partial\rho/\partial\theta) && \text{Using Equation T3} \\
&= \text{Tr}((X - \theta)\partial\rho/\partial\theta) \quad (3)
\end{aligned}$$

Now let us define L where

$$2\partial\rho/\partial\theta = \rho L + L\rho \quad (4)$$

This is called the symmeterized logarithmic derivative of ρ , i.e. if ρ and L were functions then we could define L as $\partial(\log\rho)/\partial\theta = \frac{1}{\rho}\partial\rho/\partial\theta$ or $\partial\rho/\partial\theta\frac{1}{\rho}$. However, since ρ and L are operators, we take the value of $\partial\rho/\partial\theta$ to be a combination of the 2 possibilities, leading to Equation 4, and hence the name ‘symmeterized logarithmic

derivative of ρ' . A more in depth explanation can be found in ref. [111].

We can show that L is Hermetian as follows

$$\begin{aligned}
 \partial\rho/\partial\theta &= (\partial\rho/\partial\theta)^\dagger && \text{Using Equation D3} \\
 (\rho L + L\rho)/2 &= ((\rho L + L\rho)/2)^\dagger && \text{Using Equation 4} \\
 \rho L + L\rho &= (\rho L)^\dagger + (L\rho)^\dagger && \text{Using Equation HC1} \\
 &= L^\dagger\rho^\dagger + \rho^\dagger L^\dagger && \text{Using Equation HC2} \\
 &= L^\dagger\rho + \rho L^\dagger && \text{Using Equaton D3} \\
 0 &= \rho(L - L^\dagger) + (L - L^\dagger)\rho \\
 L &= L^\dagger
 \end{aligned} \tag{5}$$

Now going back and taking the square of Equation 3 we obtain

$$\begin{aligned}
 (1 + b'(\theta))^2 &= [\text{Tr}((X - \theta)\partial\rho/\partial\theta)]^2 \\
 &= [\text{Tr}((X - \theta)(\rho L + L\rho)/2)]^2 && \text{Using Equation 4} \\
 &= [\text{Tr}((X - \theta)((L\rho)^\dagger + L\rho)/2)]^2 && \text{Using Equation HC2} \\
 &= [\text{Tr}((X - \theta)\mathcal{R}[L\rho])]^2 && \mathcal{R}[L\rho] \text{ is the real part of } L\rho \\
 &= \{\mathcal{R}[\text{Tr}((X - \theta)L\rho)]\}^2
 \end{aligned} \tag{6}$$

Using the fact that $[\mathcal{R}(z)]^2 \leq |z|^2$ we can write

$$\begin{aligned}
 (1 + b'(\theta))^2 &= \{\mathcal{R}[\text{Tr}((X - \theta)L\rho)]\}^2 \leq |\text{Tr}((X - \theta)L\rho)|^2 \\
 &\leq |\text{Tr}(L\rho(X - \theta))|^2 && \text{Using Equation T1} \\
 &\leq |\text{Tr}(L\rho^{\frac{1}{2}}\rho^{\frac{1}{2}}(X - \theta))|^2
 \end{aligned} \tag{7}$$

Using the Cauchy Schwarz Inequality from Equation CS3 we obtain that

$$\begin{aligned} |\text{Tr}(L\rho^{\frac{1}{2}}\rho^{\frac{1}{2}}(X - \theta))|^2 &\leq \text{Tr}[L\rho^{\frac{1}{2}}(L\rho^{\frac{1}{2}})^\dagger]\text{Tr}[\rho^{\frac{1}{2}}(X - \theta)(\rho^{\frac{1}{2}}(X - \theta))^\dagger] \\ &\leq \text{Tr}(\rho L^2)\text{Tr}(\rho(X - \theta)^2) \end{aligned} \quad \begin{matrix} \text{Using Equations HC2 and T1} \\ (8) \end{matrix}$$

Now going back and using to Equation 7 we get

$$(1 + b'(\theta))^2 \leq |\text{Tr}(L\rho(X - \theta))|^2 \leq \text{Tr}(\rho L^2)\text{Tr}(\rho(X - \theta)^2) \quad \text{Using Equation 8} \quad (9)$$

Rearranging this we get

$$\begin{aligned} \text{Tr}(\rho(X - \theta)^2) &\geq (1 + b'(\theta))^2 / (\text{Tr}[\rho L^2]) \\ E(\hat{\theta} - \theta)^2 &\geq (1 + b'(\theta))^2 / (\text{Tr}[\rho L^2]) \end{aligned} \quad \begin{matrix} \text{Using Equation 2} \\ (10) \end{matrix}$$

This last equation is called the Quantum Cramér-Rao Bound. Note that if the estimator $\hat{\theta}$ is unbiased, then

$$E(\hat{\theta}) = \theta \Rightarrow b(\theta) = 0 \quad (11)$$

$$\Rightarrow E(\hat{\theta} - \theta)^2 \geq 1 / (\text{Tr}[\rho L^2]) \quad \text{Using Equation 10} \quad (12)$$

where the term $\text{Tr}[\rho L^2]$ is referred to as the Quantum Fisher Information $F(\theta)$ [112]. The reason being that the greater $F(\theta)$ is, the lower the bound on the variance of the estimator becomes and so each data point gathered provides a greater amount of information about the parameter θ .

B.4 Acknowledgements

Many thanks to Akash Maharaj for helping me with the derivation, to Ken Van Tilburg and Kasper Sakmann for their insights, to Onur Hosten for his proofreading and corrections and to Brannon Klopfer for his help with L^AT_EX. Cheers guys!

Appendix C

Cavity Optomechanics of our system

This chapter looks at the optomechanical effects on our system. Taking our system to be an atom cloud trapped in a harmonic potential, we use the following assumptions:

- we have 500,000 atoms in our trap
- our atoms are placed at the antinode of the cavity field
- the oscillation period of our trap is 1.1ms
- our atom cloud FWHM is 50 nm

In our system, since we are in the Lamb-Dicke regime and our ensemble is placed at the antinode of the cavity field (i.e. we are in the quadratic regime), the optomechanical coupling term in the Hamiltonian is [113]

$$H_{quad} = \hbar g_{om} k Z_{ho} \cos(2\phi_0) \left(\frac{Z_{cm}^2}{Z_{ho}^2} + \frac{\sigma^2}{Z_{ho}} \right) a^\dagger a$$

where

- k is the wave-vector of the cavity field
- Z_{cm} is the center of mass position of the atom cloud

- σ is the atom cloud HWHM
- $\phi_0 = kz_0$
- $Z_{ho} = \sqrt{\hbar/2Nm\omega_k}$ is the natural length of the harmonic oscillator (where N is the atom number, m is the mass of a Rb atom and ω_k is the oscillation frequency of the atom cloud) and
- g_{om} is the optomechanical coupling constant defined as

$$g_{om} = N \frac{g_0^2}{\Delta} \sin(2\phi_0) k Z_{ho}$$

In order to see the effect of this term compared to our dispersive phase-imparting term ($\hbar \frac{g_0^2}{\Delta} a^\dagger a N$) we take the ratio of the 2, which gives us

$$k Z_{ho} \sin(2\phi_0) k Z_{ho} \cos(2\phi_0) \left(\frac{Z_{cm}^2}{Z_{ho}^2} + \frac{\sigma^2}{Z_{ho}^2} \right)$$

Taking the maximum of $\sin(2\phi_0) \cos(2\phi_0)$ for the sake of argument, and plugging in the numbers, we get

$$3.2 \times 10^{13} m^{-2} Z_{cm}^2 + 7.2 \times 10^{-12}$$

where in this case m stands for meters.

Bibliography

- [1] M. Kasevich. Atom interferometry in an atomic fountain. PhD thesis. Stanford: Stanford University, 1992.
- [2] P. Forman. Atomichron #174;; The atomic clock from concept to commercial product. *Proceedings of the IEEE*, 73(7):1181–1204, 1985. DOI: [10.1109/PROC.1985.13266](https://doi.org/10.1109/PROC.1985.13266).
- [3] V. B. Braginskij, F. Y. Khalili, and K. S. Thorne. *Quantum measurement*. eng. 1. paperback ed., with corr., transferred to digital printing. OCLC: 255282309. Cambridge: Cambridge Univ. Press, 1999.
- [4] W. Heisenberg. Über den anschaulichen Inhalt der quantentheoretischen Kinematik und Mechanik. de. *Zeitschrift für Physik*, 43(3-4):172–198, 1927. DOI: [10.1007/BF01397280](https://doi.org/10.1007/BF01397280).
- [5] V. Giovannetti, S. Lloyd, and L. Maccone. Advances in quantum metrology. *Nature Photonics*, 5(4):222–229, 2011. DOI: [10.1038/nphoton.2011.35](https://doi.org/10.1038/nphoton.2011.35).
- [6] M. Kitagawa and M. Ueda. Squeezed spin states. *Physical Review A*, 47(6):5138–5143, 1993. DOI: [10.1103/PhysRevA.47.5138](https://doi.org/10.1103/PhysRevA.47.5138).
- [7] O. Hosten, N. J. Engelsen, R. Krishnakumar, and M. A. Kasevich. Measurement noise 100 times lower than the quantum-projection limit using entangled atoms. *Nature*, 529(7587):505–508, 2016. DOI: [10.1038/nature16176](https://doi.org/10.1038/nature16176).
- [8] O. Hosten, R. Krishnakumar, N. J. Engelsen, and M. A. Kasevich. Quantum phase magnification. en. *Science*, 352(6293):1552–1555, 2016. DOI: [10.1126/science.aaf3397](https://doi.org/10.1126/science.aaf3397).

- [9] N. J. Engelsen, R. Krishnakumar, O. Hosten, and M. A. Kasevich. Bell Correlations in Spin-Squeezed States of 500 000 Atoms. *Physical Review Letters*, 118(14):140401, 2017. DOI: [10.1103/PhysRevLett.118.140401](https://doi.org/10.1103/PhysRevLett.118.140401).
- [10] N. J. Engelsen. Quantum metrology using large ensembles of entangled atoms. PhD thesis. Stanford: Stanford University, 2016.
- [11] D. A. Steck. Rubidium 87 D Line Data. English. Los Alamos, 2003.
- [12] J. Ye, S. Swartz, P. Jungner, and J. L. Hall. Hyperfine structure and absolute frequency of the ^{87}Rb $5\text{P}_{3/2}$ state. EN. *Optics Letters*, 21(16):1280–1282, 1996. DOI: [10.1364/OL.21.001280](https://doi.org/10.1364/OL.21.001280).
- [13] S. Bize, Y. Sortais, M. S. Santos, C. Mandache, A. Clairon, and C. Salomon. High-accuracy measurement of the ^{87}Rb ground-state hyperfine splitting in an atomic fountain. en. *EPL (Europhysics Letters)*, 45(5):558, 1999. DOI: [10.1209/epl/i1999-00203-9](https://doi.org/10.1209/epl/i1999-00203-9).
- [14] M. Born and P. Jordan. Zur Quantenmechanik. de. *Zeitschrift für Physik*, 34(1):858–888, 1925. DOI: [10.1007/BF01328531](https://doi.org/10.1007/BF01328531).
- [15] H. P. Robertson. The Uncertainty Principle. *Physical Review*, 34(1):163–164, 1929. DOI: [10.1103/PhysRev.34.163](https://doi.org/10.1103/PhysRev.34.163).
- [16] E. Schrödinger. *Zum Heisenbergschen Unschärfeprinzip*. de. Google-Books-ID: VxCFmgEACAAJ. 1930.
- [17] D. J. Wineland, J. J. Bollinger, W. M. Itano, and D. J. Heinzen. Squeezed atomic states and projection noise in spectroscopy. en. *Physical Review A*, 50(1):67–88, 1994. DOI: [10.1103/PhysRevA.50.67](https://doi.org/10.1103/PhysRevA.50.67).
- [18] J. K. Stockton, J. M. Geremia, A. C. Doherty, and H. Mabuchi. Characterizing the entanglement of symmetric many-particle spin-1/2 systems. *Physical Review A*, 67(2):022112, 2003. DOI: [10.1103/PhysRevA.67.022112](https://doi.org/10.1103/PhysRevA.67.022112).
- [19] E. C. G. Sudarshan. Equivalence of Semiclassical and Quantum Mechanical Descriptions of Statistical Light Beams. *Physical Review Letters*, 10(7):277–279, 1963. DOI: [10.1103/PhysRevLett.10.277](https://doi.org/10.1103/PhysRevLett.10.277).

- [20] R. J. Glauber. Coherent and Incoherent States of the Radiation Field. *Physical Review*, 131(6):2766–2788, 1963. DOI: [10.1103/PhysRev.131.2766](https://doi.org/10.1103/PhysRev.131.2766).
- [21] F. T. Arecchi, E. Courtens, R. Gilmore, and H. Thomas. Atomic Coherent States in Quantum Optics. *Physical Review A*, 6(6):2211–2237, 1972. DOI: [10.1103/PhysRevA.6.2211](https://doi.org/10.1103/PhysRevA.6.2211).
- [22] D. F. Walls and G. J. Milburn. *Quantum optics*. eng. 2. ed. OCLC: 254897076. Berlin: Springer, 2008.
- [23] K. Husimi. Some Formal Properties of the Density Matrix. *Proceedings of the Physico-Mathematical Society of Japan. 3rd Series*, 22(4):264–314, 1940. DOI: [10.11429/ppmsj1919.22.4_264](https://doi.org/10.11429/ppmsj1919.22.4_264).
- [24] C. T. Lee. Q representation of the atomic coherent states and the origin of fluctuations in superfluorescence. *Physical Review A*, 30(6):3308–3310, 1984. DOI: [10.1103/PhysRevA.30.3308](https://doi.org/10.1103/PhysRevA.30.3308).
- [25] E. Wigner. On the Quantum Correction For Thermodynamic Equilibrium. *Physical Review*, 40(5):749–759, 1932. DOI: [10.1103/PhysRev.40.749](https://doi.org/10.1103/PhysRev.40.749).
- [26] J. P. Dowling, G. S. Agarwal, and W. P. Schleich. Wigner distribution of a general angular-momentum state: Applications to a collection of two-level atoms. *Physical Review A*, 49(5):4101–4109, 1994. DOI: [10.1103/PhysRevA.49.4101](https://doi.org/10.1103/PhysRevA.49.4101).
- [27] E. Jaynes and F. Cummings. Comparison of quantum and semiclassical radiation theories with application to the beam maser. *Proceedings of the IEEE*, 51(1):89–109, 1963. DOI: [10.1109/PROC.1963.1664](https://doi.org/10.1109/PROC.1963.1664).
- [28] T. Donner. *Frontiers of Quantum Gas Research: Few- and Many-Body physics (FS2015)*. 2015.
- [29] M. H. Schleier-Smith. Cavity-enabled spin squeezing for a quantum-enhanced atomic clock. PhD thesis. Massachusetts Institute of Technology, 2011.
- [30] H. J. Metcalf. *Laser cooling and trapping*. Graduate texts in contemporary physics. New York: Springer, 1999.
- [31] G. Vrijen. Collective quantum behavior of atomic ensembles in high-finesse optical cavities. PhD thesis. Stanford: Stanford University, 2011.

- [32] J. Lee, G. Vrijen, I. Teper, O. Hosten, and M. A. Kasevich. Many-atom–cavity QED system with homogeneous atom–cavity coupling. EN. *Optics Letters*, 39(13):4005–4008, 2014. DOI: [10.1364/OL.39.004005](https://doi.org/10.1364/OL.39.004005).
- [33] J. Hecht. *The laser guidebook*. eng. 2. ed. Optical and electro-optical engineering series. OCLC: 27988649. New York: McGraw-Hill, 1992.
- [34] C. J. Foot. *Atomic physics*. Oxford master series in physics 7. Atomic, Optical, and laser physics. OCLC: ocm57478010. Oxford ; New York: Oxford University Press, 2005.
- [35] D. McCarron. A Guide to Acousto-Optic Modulators. English. Durham, 2007.
- [36] R. Grimm, M. Weidmüller, and Y. B. Ovchinnikov. Optical Dipole Traps for Neutral Atoms. en. In: *Advances In Atomic, Molecular, and Optical Physics*. Vol. 42. DOI: [10.1016/S1049-250X\(08\)60186-X](https://doi.org/10.1016/S1049-250X(08)60186-X). Elsevier, 2000, 95–170.
- [37] H. Vahlbruch, M. Mehmet, K. Danzmann, and R. Schnabel. Detection of 15 dB Squeezed States of Light and their Application for the Absolute Calibration of Photoelectric Quantum Efficiency. en. *Physical Review Letters*, 117(11), 2016. DOI: [10.1103/PhysRevLett.117.110801](https://doi.org/10.1103/PhysRevLett.117.110801).
- [38] C. Eichler, Y. Salathe, J. Mlynek, S. Schmidt, and A. Wallraff. Quantum-Limited Amplification and Entanglement in Coupled Nonlinear Resonators. en. *Physical Review Letters*, 113(11), 2014. DOI: [10.1103/PhysRevLett.113.110502](https://doi.org/10.1103/PhysRevLett.113.110502).
- [39] J. Abadie et al. A gravitational wave observatory operating beyond the quantum shot-noise limit. *Nature Physics*, 7(12):962–965, 2011. DOI: [10.1038/nphys2083](https://doi.org/10.1038/nphys2083).
- [40] M. A. Taylor, J. Janousek, V. Daria, J. Knittel, B. Hage, H.-A. Bachor, and W. P. Bowen. Biological measurement beyond the quantum limit. *Nature Photonics*, 7(3):229–233, 2013. DOI: [10.1038/nphoton.2012.346](https://doi.org/10.1038/nphoton.2012.346).
- [41] C. Gross, T. Zibold, E. Nicklas, J. Estève, and M. K. Oberthaler. Nonlinear atom interferometer surpasses classical precision limit. *Nature*, 464(7292):1165–1169, 2010. DOI: [10.1038/nature08919](https://doi.org/10.1038/nature08919).

- [42] M. F. Riedel, P. Böhi, Y. Li, T. W. Hänsch, A. Sinatra, and P. Treutlein. Atom-chip-based generation of entanglement for quantum metrology. *Nature*, 464(7292):1170–1173, 2010. DOI: [10.1038/nature08988](https://doi.org/10.1038/nature08988).
- [43] C. D. Hamley, C. S. Gerving, T. M. Hoang, E. M. Bookjans, and M. S. Chapman. Spin-nematic squeezed vacuum in a quantum gas. *Nature Physics*, 8(4):305–308, 2012. DOI: [10.1038/nphys2245](https://doi.org/10.1038/nphys2245).
- [44] J. Appel, P. J. Windpassinger, D. Oblak, U. B. Hoff, N. Kjaergaard, and E. S. Polzik. Mesoscopic atomic entanglement for precision measurements beyond the standard quantum limit. en. *Proceedings of the National Academy of Sciences*, 106(27):10960–10965, 2009. DOI: [10.1073/pnas.0901550106](https://doi.org/10.1073/pnas.0901550106).
- [45] T. Takano, M. Fuyama, R. Namiki, and Y. Takahashi. Spin Squeezing of a Cold Atomic Ensemble with the Nuclear Spin of One-Half. en. *Physical Review Letters*, 102(3), 2009. DOI: [10.1103/PhysRevLett.102.033601](https://doi.org/10.1103/PhysRevLett.102.033601).
- [46] M. H. Schleier-Smith, I. D. Leroux, and V. Vuletić. States of an Ensemble of Two-Level Atoms with Reduced Quantum Uncertainty. en. *Physical Review Letters*, 104(7), 2010. DOI: [10.1103/PhysRevLett.104.073604](https://doi.org/10.1103/PhysRevLett.104.073604).
- [47] I. D. Leroux, M. H. Schleier-Smith, and V. Vuletić. Implementation of Cavity Squeezing of a Collective Atomic Spin. *Physical Review Letters*, 104(7):073602, 2010. DOI: [10.1103/PhysRevLett.104.073602](https://doi.org/10.1103/PhysRevLett.104.073602).
- [48] I. D. Leroux, M. H. Schleier-Smith, and V. Vuletić. Orientation-Dependent Entanglement Lifetime in a Squeezed Atomic Clock. en. *Physical Review Letters*, 104(25), 2010. DOI: [10.1103/PhysRevLett.104.250801](https://doi.org/10.1103/PhysRevLett.104.250801).
- [49] R. J. Sewell, M. Koschorreck, M. Napolitano, B. Dubost, N. Behbood, and M. W. Mitchell. Magnetic Sensitivity Beyond the Projection Noise Limit by Spin Squeezing. en. *Physical Review Letters*, 109(25), 2012. DOI: [10.1103/PhysRevLett.109.253605](https://doi.org/10.1103/PhysRevLett.109.253605).

- [50] W. Muessel, H. Strobel, D. Linnemann, D. B. Hume, and M. K. Oberthaler. Scalable Spin Squeezing for Quantum-Enhanced Magnetometry with Bose-Einstein Condensates. en. *Physical Review Letters*, 113(10), 2014. DOI: 10.1103/PhysRevLett.113.103004.
- [51] K. C. Cox, G. P. Greve, J. M. Weiner, and J. K. Thompson. Deterministic Squeezed States with Collective Measurements and Feedback. en. *Physical Review Letters*, 116(9), 2016. DOI: 10.1103/PhysRevLett.116.093602.
- [52] J. Guéna, M. Abgrall, A. Clairon, and S. Bize. Contributing to TAI with a secondary representation of the SI second. en. *Metrologia*, 51(1):108, 2014. DOI: 10.1088/0026-1394/51/1/108.
- [53] E. Rocco, R. N. Palmer, T. Valenzuela, V. Boyer, A. Freise, and K. Bongs. Fluorescence detection at the atom shot noise limit for atom interferometry. en. *New Journal of Physics*, 16(9):093046, 2014. DOI: 10.1088/1367-2630/16/9/093046.
- [54] B. J. Bloom, T. L. Nicholson, J. R. Williams, S. L. Campbell, M. Bishof, X. Zhang, W. Zhang, S. L. Bromley, and J. Ye. An optical lattice clock with accuracy and stability at the 10-18 level. en. *Nature*, 506(7486):71–75, 2014. DOI: 10.1038/nature12941.
- [55] M. H. Schleier-Smith, I. D. Leroux, and V. Vuletić. States of an Ensemble of Two-Level Atoms with Reduced Quantum Uncertainty. *Physical Review Letters*, 104(7):073604, 2010. DOI: 10.1103/PhysRevLett.104.073604.
- [56] P. Hyllus, L. Pezzé, A. Smerzi, and G. Tóth. Entanglement and extreme spin squeezing for a fluctuating number of indistinguishable particles. *Physical Review A*, 86(1):012337, 2012. DOI: 10.1103/PhysRevA.86.012337.
- [57] B. Lücke, J. Peise, G. Vitagliano, J. Arlt, L. Santos, G. Tóth, and C. Klempt. Detecting Multiparticle Entanglement of Dicke States. *Physical Review Letters*, 112(15):155304, 2014. DOI: 10.1103/PhysRevLett.112.155304.

- [58] F. Haas, J. Volz, R. Gehr, J. Reichel, and J. Esteve. Entangled States of More Than 40 Atoms in an Optical Fiber Cavity. en. *Science*, 344(6180):180–183, 2014. DOI: [10.1126/science.1248905](https://doi.org/10.1126/science.1248905).
- [59] O. Gühne and G. Tóth. Entanglement detection. *Physics Reports*, 474(1):1–75, 2009. DOI: [10.1016/j.physrep.2009.02.004](https://doi.org/10.1016/j.physrep.2009.02.004).
- [60] G. W. Biedermann, K. Takase, X. Wu, L. Deslauriers, S. Roy, and M. A. Kasevich. Zero-Dead-Time Operation of Interleaved Atomic Clocks. *Physical Review Letters*, 111(17):170802, 2013. DOI: [10.1103/PhysRevLett.111.170802](https://doi.org/10.1103/PhysRevLett.111.170802).
- [61] J. Borregaard and A. S. Sørensen. Near-Heisenberg-Limited Atomic Clocks in the Presence of Decoherence. *Physical Review Letters*, 111(9):090801, 2013. DOI: [10.1103/PhysRevLett.111.090801](https://doi.org/10.1103/PhysRevLett.111.090801).
- [62] J. G. Bohnet, K. C. Cox, M. A. Norcia, J. M. Weiner, Z. Chen, and J. K. Thompson. Reduced spin measurement back-action for a phase sensitivity ten times beyond the standard quantum limit. *Nature Photonics*, 8(9):731–736, 2014. DOI: [10.1038/nphoton.2014.151](https://doi.org/10.1038/nphoton.2014.151).
- [63] B. Lucke, M. Scherer, J. Kruse, L. Pezze, F. Deuretzbacher, P. Hyllus, O. Topic, J. Peise, W. Ertmer, J. Arlt, L. Santos, A. Smerzi, and C. Klempt. Twin Matter Waves for Interferometry Beyond the Classical Limit. en. *Science*, 334(6057):773–776, 2011. DOI: [10.1126/science.1208798](https://doi.org/10.1126/science.1208798).
- [64] R. McConnell, H. Zhang, J. Hu, S. Ćuk, and V. Vuletić. Entanglement with negative Wigner function of almost 3,000 atoms heralded by one photon. *Nature*, 519(7544):439–442, 2015. DOI: [10.1038/nature14293](https://doi.org/10.1038/nature14293).
- [65] H. Zhang, R. McConnell, S. Ćuk, Q. Lin, M. H. Schleier-Smith, I. D. Leroux, and V. Vuletić. Collective State Measurement of Mesoscopic Ensembles with Single-Atom Resolution. en. *Physical Review Letters*, 109(13), 2012. DOI: [10.1103/PhysRevLett.109.133603](https://doi.org/10.1103/PhysRevLett.109.133603).
- [66] J. Volz, R. Gehr, G. Dubois, J. Estève, and J. Reichel. Measurement of the internal state of a single atom without energy exchange. *Nature*, 475(7355):210–213, 2011. DOI: [10.1038/nature10225](https://doi.org/10.1038/nature10225).

- [67] D. B. Hume, I. Stroescu, M. Joos, W. Muessel, H. Strobel, and M. K. Oberthaler. Accurate Atom Counting in Mesoscopic Ensembles. en. *Physical Review Letters*, 111(25), 2013. DOI: [10.1103/PhysRevLett.111.253001](https://doi.org/10.1103/PhysRevLett.111.253001).
- [68] I. Stroescu, D. B. Hume, and M. K. Oberthaler. Double-well atom trap for fluorescence detection at the Heisenberg limit. en. *Physical Review A*, 91(1), 2015. DOI: [10.1103/PhysRevA.91.013412](https://doi.org/10.1103/PhysRevA.91.013412).
- [69] E. Davis, G. Bentsen, and M. Schleier-Smith. Approaching the Heisenberg Limit without Single-Particle Detection. en. *Physical Review Letters*, 116(5), 2016. DOI: [10.1103/PhysRevLett.116.053601](https://doi.org/10.1103/PhysRevLett.116.053601).
- [70] Y.-L. Zhang, C.-L. Zou, X.-B. Zou, L. Jiang, and G.-C. Guo. Detuning-enhanced cavity spin squeezing. *Physical Review A*, 91(3):033625, 2015. DOI: [10.1103/PhysRevA.91.033625](https://doi.org/10.1103/PhysRevA.91.033625).
- [71] M. O. Scully and M. S. Zubairy. *Quantum optics*. Cambridge ; New York: Cambridge University Press, 1997.
- [72] R. McConnell, H. Zhang, S. Ćuk, J. Hu, M. H. Schleier-Smith, and V. Vuletić. Generating entangled spin states for quantum metrology by single-photon detection. en. *Physical Review A*, 88(6), 2013. DOI: [10.1103/PhysRevA.88.063802](https://doi.org/10.1103/PhysRevA.88.063802).
- [73] S. Massar and E. S. Polzik. Generating a Superposition of Spin States in an Atomic Ensemble. en. *Physical Review Letters*, 91(6), 2003. DOI: [10.1103/PhysRevLett.91.060401](https://doi.org/10.1103/PhysRevLett.91.060401).
- [74] H. Strobel, W. Muessel, D. Linnemann, T. Zibold, D. B. Hume, L. Pezze, A. Smerzi, and M. K. Oberthaler. Fisher Information and Entanglement of Non-Gaussian Spin States. *Science*, 345(6195):424–427, 2014. DOI: [10.1126/science.1250147](https://doi.org/10.1126/science.1250147).
- [75] W. Muessel, H. Strobel, D. Linnemann, T. Zibold, B. Juliá-Díaz, and M. K. Oberthaler. Twist-and-turn spin squeezing in Bose-Einstein condensates. en. *Physical Review A*, 92(2), 2015. DOI: [10.1103/PhysRevA.92.023603](https://doi.org/10.1103/PhysRevA.92.023603).

- [76] J. G. Bohnet, B. C. Sawyer, J. W. Britton, M. L. Wall, A. M. Rey, M. Foss-Feig, and J. J. Bollinger. Quantum spin dynamics and entanglement generation with hundreds of trapped ions. en. *Science*, 352(6291):1297–1301, 2016. DOI: 10.1126/science.aad9958.
- [77] R. Horodecki, P. Horodecki, M. Horodecki, and K. Horodecki. Quantum Entanglement. *Reviews of Modern Physics*, 81(2):865–942, 2009. DOI: 10.1103/RevModPhys.81.865.
- [78] N. Li and S. Luo. Entanglement Detection via Quantum Fisher Information. *Physical Review A*, 88(1):014301, 2013. DOI: 10.1103/PhysRevA.88.014301.
- [79] C. W. Helstrom. Minimum Mean-Squared Error of Estimates in Quantum Statistics. *Physics Letters A*, 25(2):101–102, 1967. DOI: 10.1016/0375-9601(67)90366-0.
- [80] S. L. Braunstein and C. M. Caves. Statistical Distance and the Geometry of Quantum States. *Physical Review Letters*, 72(22):3439–3443, 1994. DOI: 10.1103/PhysRevLett.72.3439.
- [81] A. S. Sørensen and K. Mølmer. Entanglement and Extreme Spin Squeezing. *Phys. Rev. Lett.* 86:4431–4434, 2001. DOI: 10.1103/PhysRevLett.86.4819.
- [82] B. Lucke, J. Peise, G. Vitagliano, J. Arlt, L. Santos, G. Toth, and C. Klempt. Detecting Multiparticle Entanglement of Dicke States. *Physical Review Letters*, 112(15):155304, 2014. DOI: 10.1103/PhysRevLett.112.155304.
- [83] S. B. Papp, K. S. Choi, H. Deng, P. Lougovski, S. J. van Enk, and H. J. Kimble. Characterization of Multipartite Entanglement for One Photon Shared Among Four Optical Modes. en. *Science*, 324(5928):764–768, 2009. DOI: 10.1126/science.1172260.
- [84] N. Brunner, D. Cavalcanti, S. Pironio, V. Scarani, and S. Wehner. Bell Non-locality. *Reviews of Modern Physics*, 86(2):419–478, 2014. DOI: 10.1103/RevModPhys.86.419.

- [85] J. F. Clauser, M. A. Horne, A. Shimony, and R. A. Holt. Proposed Experiment to Test Local Hidden-Variable Theories. *Physical Review Letters*, 23(15):880–884, 1969. DOI: [10.1103/PhysRevLett.23.880](https://doi.org/10.1103/PhysRevLett.23.880).
- [86] M. Eibl, S. Gaertner, M. Bourennane, C. Kurtsiefer, M. Zukowski, and H. Weinfurter. Experimental Observation of Four-Photon Entanglement from Parametric down-Conversion. *Physical Review Letters*, 90(20):200403, 2003. DOI: [10.1103/PhysRevLett.90.200403](https://doi.org/10.1103/PhysRevLett.90.200403).
- [87] Z. Zhao, T. Yang, Y.-A. Chen, A.-N. Zhang, M. Żukowski, and J. W. Pan. Experimental Violation of Local Realism by Four-Photon Greenberger-Horne-Zeilinger Entanglement. *Physical Review Letters*, 91(18):180401, 2003. DOI: [10.1103/PhysRevLett.91.180401](https://doi.org/10.1103/PhysRevLett.91.180401).
- [88] M. Giustina et al. Significant-Loophole-Free Test of Bell’s Theorem with Entangled Photons. *Physical Review Letters*, 115(25):250401, 2015. DOI: [10.1103/PhysRevLett.115.250401](https://doi.org/10.1103/PhysRevLett.115.250401).
- [89] L. K. Shalm et al. Strong Loophole-Free Test of Local Realism. *Physical Review Letters*, 115(25):250402, 2015. DOI: [10.1103/PhysRevLett.115.250402](https://doi.org/10.1103/PhysRevLett.115.250402).
- [90] B. P. Lanyon, M. Zwerger, P. Jurcevic, C. Hempel, W. Dur, H. J. Briegel, R. Blatt, and C. F. Roos. Experimental Violation of Multipartite Bell Inequalities with Trapped Ions. *Physical Review Letters*, 112(10):100403, 2014. DOI: [10.1103/PhysRevLett.112.100403](https://doi.org/10.1103/PhysRevLett.112.100403).
- [91] J. Hofmann, M. Krug, N. Ortegel, L. Gerard, M. Weber, W. Rosenfeld, and H. Weinfurter. Heralded Entanglement Between Widely Separated Atoms. *Science*, 337(6090):72–75, 2012. DOI: [10.1126/science.1221856](https://doi.org/10.1126/science.1221856).
- [92] W. Pfaff, T. H. Taminiau, L. Robledo, H. Bernien, M. Markham, D. J. Twitchen, and R. Hanson. Demonstration of Entanglement-by-Measurement of Solid-State Qubits. *Nature Physics*, 9(1):29–33, 2013. DOI: [10.1038/NPHYS2444](https://doi.org/10.1038/NPHYS2444).
- [93] B. Hensen et al. Loophole-Free Bell Inequality Violation Using Electron Spins Separated by 1.3 Kilometres. en. *Nature*, 526(7575):682–686, 2015. DOI: [10.1038/nature15759](https://doi.org/10.1038/nature15759).

- [94] J. Tura, R. Augusiak, A. B. Sainz, T. Vertesi, M. Lewenstein, and A. Acin. Detecting Nonlocality in Many-Body Quantum States. en. *Science*, 344(6189):1256–1258, 2014. doi: [10.1126/science.1247715](https://doi.org/10.1126/science.1247715).
- [95] R. Schmied, J.-D. Bancal, B. Allard, M. Fadel, V. Scarani, P. Treutlein, and N. Sangouard. Bell Correlations in a Bose-Einstein Condensate. en. *Science*, 352(6284):441–444, 2016. doi: [10.1126/science.aad8665](https://doi.org/10.1126/science.aad8665).
- [96] J. Tura, R. Augusiak, A. B. Sainz, B. Lucke, C. Klempt, M. Lewenstein, and A. Acin. Nonlocality in Many-Body Quantum Systems Detected with Two-Body Correlators. *Annals of Physics*, 362:370–423, 2015. doi: [10.1016/j.aop.2015.07.021](https://doi.org/10.1016/j.aop.2015.07.021).
- [97] M. Kitagawa and M. Ueda. Squeezed Spin States. *Physical Review A*, 47(6):5138–5143, 1993. doi: [10.1103/PhysRevA.47.5138](https://doi.org/10.1103/PhysRevA.47.5138).
- [98] D. J. Wineland, J. J. Bollinger, W. M. Itano, and D. J. Heinzen. Squeezed Atomic States and Projection Noise in Spectroscopy. *Phys. Rev. A*, 50:67–88, 1994. doi: [10.1103/PhysRevA.50.67](https://doi.org/10.1103/PhysRevA.50.67).
- [99] L. Dellantonio, S. Das, J. Appel, and A. S. Sorensen. Multi-Partite Entanglement Detection with Non Symmetric Probing, 2016. arXiv: [1609.08516](https://arxiv.org/abs/1609.08516) [cond-mat, physics:quant-ph].
- [100] S. Pironio, A. Acin, S. Massar, A. Boyer de la Giroday, D. N. Matsukevich, P. Maunz, S. Olmschenk, D. Hayes, L. Luo, T. A. Manning, and C. Monroe. Random Numbers Certified by Bell’s Theorem. en. *Nature*, 464(7291):1021–1024, 2010. doi: [10.1038/nature09008](https://doi.org/10.1038/nature09008).
- [101] T. Kovachy, P. Asenbaum, C. Overstreet, C. A. Donnelly, S. M. Dickerson, A. Sugarbaker, J. M. Hogan, and M. A. Kasevich. Quantum Superposition at the Half-Metre Scale. en. *Nature*, 528(7583):530–533, 2015. doi: [10.1038/nature16155](https://doi.org/10.1038/nature16155).
- [102] L. Dellantonio. Entanglement criteria for Spin Squeezing. MA thesis. University of Copenhagen, 2015.

- [103] G. Vitagliano, I. Apellaniz, M. Kleinmann, B. Lucke, C. Klempf, and G. Toth. Entanglement and Extreme Spin Squeezing of Unpolarized States. *arXiv:1605.07202 [quant-ph]*, 2016. arXiv: 1605.07202 [quant-ph].
- [104] STAT 414 / 415 Lecture Notes. The Pennsylvania State University, 2017.
- [105] M. G. Bulmer. *Principles of statistics*. New York: Dover Publications, 1979.
- [106] A. de Moivre. *The doctrine of chances: or, a method for calculating the probabilities of events in play*. 2nd. Woodfall, 1738.
- [107] P.-S. Laplace. *Théorie analytique des probabilités*. Paris, 1812.
- [108] A. Lyapunov. Theorem of Laplace. 1901.
- [109] K. O. Bowman and L. R. Shenton. *Properties of estimators for the gamma distribution*. Statistics, textbooks and monographs v. 89. New York: Marcel Dekker, 1988.
- [110] C. Helstrom. Minimum mean-squared error of estimates in quantum statistics. en. *Physics Letters A*, 25(2):101–102, 1967. DOI: 10.1016/0375-9601(67)90366-0.
- [111] A. S. Holevo. *Probabilistic and statistical aspects of quantum theory*. eng. North-Holland series in statistics and probability v. 1. Amsterdam ; New York : New York: North-Holland Pub. Co. ; Sole distributors for the U.S.A. and Canada, Elsevier Science Pub. Co, 1982.
- [112] S. L. Braunstein and C. M. Caves. Statistical distance and the geometry of quantum states. *Physical Review Letters*, 72(22):3439–3443, 1994. DOI: 10.1103/PhysRevLett.72.3439.
- [113] D. M. Stamper-Kurn. Cavity optomechanics with cold atoms. *arXiv:1204.4351 [cond-mat, physics:physics, physics:quant-ph]*, 2012. arXiv: 1204.4351.